UCRL-53649

Spin-Flip (p,n) Reactions on ^{26}Mg, ^{54}Fe, and ^{56}Fe at Selected Proton Bombarding Energies in the Range of 17 to 25 MeV

David Leonard Aron

(Ph. D. Thesis)

June 1985

Lawrence Livermore National Laboratory

UCRL-53649
Distribution Category UC-34c

UCRL--53649

DE85 015664

Spin-Flip (p,n) Reactions on ^{26}Mg, ^{54}Fe, and ^{56}Fe at Selected Proton Bombarding Energies in the Range of 17 to 25 MeV

David Leonard Aron

(Ph. D. Thesis)

Manuscript date: June 1985

LAWRENCE LIVERMORE NATIONAL LABORATORY
University of California • Livermore, California • 94550

Available from: National Technical Information Service • U.S. Department of Commerce
5285 Port Royal Road • Springfield, VA 22161 • $16.00 per copy • (Microfiche $4.50)

Spin-Flip (p,n) Reactions on ^{26}Mg, ^{54}Fe, and ^{56}Fe at Selected Proton Bombarding Energies in the Range of 17 to 25 MeV

By

DAVID LEONARD ARON
A.B. (University of California, Berkeley) 1975
M.S. (University of California, Davis) 1978

DISSERTATION

Submitted in partial satisfaction of the requirements for the degree of

DOCTOR OF PHILOSOPHY

in

Engineering-Applied Science

in the

GRADUATE DIVISION

of the

UNIVERSITY OF CALIFORNIA

DAVIS

Approved:

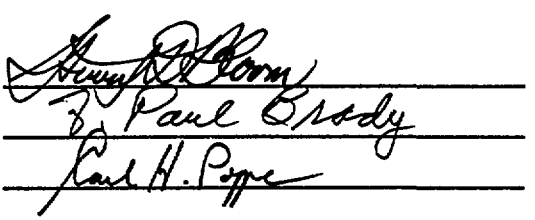

Committee in Charge

Deposited in the University Library _____
Date Librarian

David Leonard Aron
June 1985
Applied Science

Spin-Flip (p,n) Reactions on ^{26}Mg, ^{54}Fe, and ^{56}Fe at Selected Proton Bombarding Energies in the Range of 17 to 25 MeV

ABSTRACT

New data are presented for the ^{26}Mg (p,n)^{26}Al reaction at E_p = 19.12 and 24.97 MeV, for the $^{54}Fe(p,n)^{54}Co$ reaction at E_p = 17.20, 18.60, and 24.60 MeV, and for the $^{56}Fe(p,n)^{56}Co$ reaction at E_p = 19.12 and 24.59 MeV. Data were taken with the LLNL Cyclograaff at 16 angles from 3.5° to 159.0°. A large detector at 23.8° with a long neutron flight path collected high resolution spectra. This large detector also collected separate 0° high resolution data on the ^{26}Mg and $^{56}Fe(p,n)$ reactions at E_p = 19 MeV.

Absolute differential (p,n) cross sections were extracted for 1^+ states in ^{26}Al, ^{54}Co, and ^{56}Co, for the 0^+ isobaric analog state (IAS) in ^{54}Co and ^{56}Co, for a 2^+ state in each residual nucleus, and for the 0.199 MeV 7^+ state of ^{54}Co. No new experimental states were identified. Only relative cross sections were extracted at 0°. Experimental angle-integrated cross sections were obtained for all but one state.

DWBA79 was used, with the G-matrix effective nucleon-nucleon interaction of Bertsch *et al.* (with the central triplet-odd component V_{to} = 0) and the Livermore shell model wave functions to calculate differential (p,n) cross sections to 1^+ states and to the ^{54}Co and ^{56}Co IAS. The shapes of all DWBA79 calculations were in good agreement with measurements. The ratio n of the angle-integrated measured cross section to the DWBA calculated angle-integrated cross section ranged from n = 0.62 to n = 1.56 for all states with

these exceptions: ^{54}Co IAS (n = 2.59 at 17.20 MeV, n = 2.51 at 18.60 MeV), and ^{56}Co 1.7203 MeV 1^+ (n = 0.12 at 19.11 MeV, n = 0.10 at 24.59 MeV). The large values of n for the ^{54}Co IAS at 17.20 MeV and 18.60 MeV may have been due to the contribution from decay of the ^{55}Co compound nucleus. The small values of n for the ^{56}Co 1.7203 MeV 1^+ indicated that the shell model wave function was inadequate to describe that particular state. n ranged from 0.62 to 0.88 for all 1^+ states except for the following states: ^{56}Co 1.7203 MeV 1^+ (n = 0.10, and 0.12), ^{54}Co 0.9372 MeV 1^+ (n = 1.50 at 17.20 MeV, and n = 1.35 at 18.60 MeV), ^{26}Al 1.0578 MeV 1^+ (n = 1.09 at 19.12 MeV), and ^{26}Al 9.44 MeV 1^+; T = 1 (n = 1.15 at 24.97 MeV).

Normalization of the DWBA angle-integrated cross sections to measurements for the ^{54}Co and ^{56}Co IAS (at E_p = 24.6 MeV) yielded the renormalized V_τ = 21.4±2.1 MeV. Normalization of the DWBA angle-integrated cross sections to measurements for the 24.6 MeV ^{54}Co and ^{56}Co 1^+ states, coupled with the normalization of the wave functions to previously experimentally determined GT strength, yielded the renormalized $V_{\sigma\tau}$ = 12.3±1.2 MeV.

The experimental Gamow-Teller strength $B(GT)_{exp.}$ of the T = 1 ^{26}Al state at 9.44 MeV was found to be 0.69; $B(GT)_{exp.}$ of the T = 1 ^{26}Al state at 10.47 MeV was found to be 0.39. These strengths were obtained by normalization of the wave functions using the Gamow-Teller matrix element of the 1.0578 MeV 1^+ ^{26}Al state. This matrix element was previously determined experimentally from the beta decay of ^{26}Si. Shell model calculations of the Gamow-Teller strength $B(GT)_{calc.}$ gave $B(GT)_{calc.}$ = 0.49 for the 9.44 MeV state, and $B(GT)_{calc.}$ = 0.42 for the 10.47 MeV state. Thus, it is concluded that the measured Gamow-Teller strength of the 9.44 MeV state is enhanced (by a factor

of 1.39) compared to the theoretically predicted value. Also, the measured Gamow-Teller strength of the 10.47 MeV state is quenched (by a factor of 0.93) compared to the theoretically predicted value.

Finally, it is concluded that the G-matrix interaction (with the central triplet-odd component of the effective nucleon-nucleon interaction set to zero: $V_{to} = 0$) provided a good description of the effective nucleon-nucleon interaction. Also, shell model wave functions gave reasonable descriptions of the 1^+ states and of the ^{54}Co and ^{56}Co IAS.

TABLE OF CONTENTS

Page

I. INTRODUCTION

The (p,n) reaction has been used as an experimental tool for many years to identify the energies, spins, and parities of states in the residual nucleus. It has also been used as a means of elucidating optical model parameters and of understanding nuclear structure and the effective nuclear interaction. For example, the (p,n) reaction was used in the discovery of the isobaric analog state phenomenon.[1] In the work described here we have performed experiments with the (p,n) reaction on ^{26}Mg, ^{54}Fe, and ^{56}Fe for selected proton energies from 17 to 25 MeV. The isobaric analog state (IAS) in Co of the ground state of Fe was investigated for both stable isotopes of iron. Although this research concentrated mainly on the 1^+ levels of the residual nuclei, we also included some states of spin other than one. The choice of the three target nuclei was based on the search for new 1^+ states in the residual nuclei, coupled with the availability of manufactured targets. The proton bombarding energies were chosen, within the constraints of the LLNL Cyclograaff Facility parameters, to give reasonable energy resolution at the lower energies, and also to elucidate the dependence of the cross sections on the proton bombarding energy.

The (p,n) reaction on ^{26}Mg, ^{54}Fe, and ^{56}Fe at high proton bombarding energies has recently been used to study the Gamow-Teller strength distributions in the residual nuclei.[2-5] These measurements were limited in several ways. First, the high proton bombarding energies resulted in poor resolution of the states in the residual nucleus. Individual states were often difficult, sometimes impossible to resolve. Second, the experimental apparatus restricted the angular distributions to a few forward angles.

The measurements of this paper complemented the above earlier high energy measurements. Our low energy measurements plus the high energy ones gave the

variation in (p,n) differential cross sections with proton energy. In addition, our measurements generally had considerably better energy resolution, allowing the identification of individual states. Angular distributions taken over the larger range of 0° (or 3.5°) to 159° in the laboratory system, permitted the comparison of measured cross sections with DWBA calculations for transitions to individual states. However, the high proton energy work had the advantage of preferentially exciting the 1^+ states compared to the other states. Also, the maximum excitation energy attainable in the residual nucleus was greater for measurements at high proton bombarding energy than for those of this thesis.

Our low bombarding energy (p,n) measurements provided further opportunity to test the validity of the various shell model calculations made at Livermore. The (p,n) measurements of this work enabled us to compare DWBA calculations with angular distributions of 1^+ states. Z-coefficients from shell model calculations were used by the DWBA code to calculate differential cross sections for a number of transitions (the Z-coefficients are coefficients of fractional parentage; they measure the contribution of each of the possible particle-hole pairs in the (p,n) reaction). Comparison of measured with DWBA calculated cross sections yielded information on the accuracy of the shell model calculation of Z-coefficients, and therefore the accuracy of the nuclear wave functions, within the limits of the validity of both the DWBA approximation and the effective nucleon-nucleon interaction.

The present investigation had both a theoretical component and an experimental one. Experimentally, the (p,n) reaction was used to observe the excitation of various states in the residual nuclei. An attempt was made to identify new 1^+ states, as well as to measure differential cross sections of known 1^+ states. The (p,n) differential cross sections were measured at 16 angles between 3.5° and 159°; in some cases a 0° measurement was made. Angle-integration of

most of these measured cross sections was also done. A large neutron detector was used in conjunction with a long neutron flight path at 23.8° for better energy resolution than that of the other 15 detectors. All the 0° measurements utilized this large detector; its characteristics, including measured efficiency, will be fully described in section II.E.

The theoretical component consisted of first using DWBA79, a distorted-wave Born approximation computer code, to calculate (p,n) differential cross sections for transitions to many of the experimentally observed nuclear states. Then a comparison was made with measured cross sections and an attempt was made to understand the comparison in terms of nuclear structure and nuclear reaction theory. The shell model codes were also used to generate a manifold of excited states, and a 1^+ strength function; both were compared with experiment.

We now review some of the previous research on the ^{26}Mg, ^{54}Fe, and ^{56}Fe(p,n) reactions. Twenty years ago, J.D. Anderson *et al.*[6] used the Livermore 90-in. cyclotron to measure the differential cross sections from the isobaric analog (p,n) reaction on 19 targets, including Fe, at a proton bombarding energy of 18.5 MeV for lab angles of 3° to 153° in approximately 15° steps. Differential cross sections for isobaric analog reactions were also measured for 17 MeV protons on Fe, and on three other targets for lab angles of 3° to 153° in approximately 30° steps. In ^{56}Fe(p,n), the isobaric analog of the ^{56}Fe ground state, several excited isobaric analog states, and the configuration state were observed in ^{56}Co; all these states had been previously identified.[7] Configuration states are defined as "states in which the overall configuration of the nucleus is unchanged (apart from the exchange of a neutron for a proton)."[8] Note that configuration states whose isospin T is the same in both the target and the residual nucleus are designated isobaric analog states. Cross sections for the $^{56}Fe(p,n)^{56}Co$ 3.59 MeV 0^+ isobaric analog state (IAS) were obtained at 17 and

18.5 MeV; cross sections for the 4.44 MeV 2^+ excited analog state were obtained at 17 MeV. Using the approximation that the incoming proton and outgoing neutron were plane waves, a simple Lane optical model calculation was able to fit the $^{56}Fe(p,n)^{56}Co$ IAS differential cross sections at Ep = 18.5 MeV.

In an experiment performed by R.F. Bentley and associates 35 target nuclei, including ^{26}Mg, ^{54}Fe, and ^{56}Fe, were bombarded with 22.8 MeV protons from the University of Colorado cyclotron. Results[9] (first published in 1971) included the angular distributions for the analog transition $^{26}Mg(p,n)^{26}Al$ 0^+ (E_x = 0.23 MeV), and for the transition $^{54}Fe(p,n)^{54}Co$ 7^+ (Ex = 0.199 MeV). A preliminary attempt to calculate the latter angular distribution with DWBA codes gave a poor fit to data. Bentley's 1972 Ph.D. thesis[10] (unpublished) contained a complete account of the experiment on the 35 nuclei. Cross sections were measured for a number of states in ^{26}Al, ^{54}Co, and ^{56}Co, including the analogs to the parent nuclei ground states, and a number of 1^+ states. The energy resolution of the states in the residual nuclei ranged from 30 to 250 KeV. A comparison of these data with the 24.6 and 25.0 MeV data of the present work will be presented in section III.A.9.

We now summarize Bentley's work on ^{26}Mg, ^{54}Fe, and ^{56}Fe: All measurements were made at a proton bombarding energy of 23.8 MeV. $^{26}Mg(p,n)$ differential cross sections were measured for the following ^{26}Al states: 0.00 MeV 5^+, 0.229 MeV 0^+, 0.418 MeV 3^+, 1.059 MeV 1^+, 1.760 MeV 2^+ (3^+), and 2.072 MeV 2^+. The angular distributions ranged from 10.5° to 153.7° in the center of mass (CM) system for the first four states above, and from 10.5° to 125.8° for the last two states.

$^{54}Fe(p,n)$ differential cross sections were measured for the following ^{54}Co states: 0.00 MeV 0^+, 0.199 MeV 7^+, 0.94 MeV 1^+, 1.446 MeV 2^+, 1.87 MeV (3^+),

2.149 MeV (5^+), 2.285 MeV (?), 2.645 MeV (4^+), and 2.90 MeV (?). The angular distributions ranged from 10.3° to 153.0° in the CM system.

^{56}Fe(p,n) differential cross sections were measured for the following ^{56}Co states: 3.577 MeV 0^+, and 4.451 MeV 2^+. The angular distributions ranged from 10.2° to 151.7° in the CM system.

In the Bentley work a number of DWBA calculations were made. The influence of the following parameters was examined: "the optical potentials, the bound valence nucleon wave functions, the range of the nucleon-nucleon interaction and the inner cutoff of the radial integral".[11] Reasonably good fits to experimental data were obtained (after normalization of the calculation to data) for the analogs to the ground states of ^{26}Mg, ^{54}Fe, and ^{56}Fe. The ^{54}Fe(p,n)^{54}Co 0.94 MeV 1^+transition and the ^{56}Fe(p,n)^{56}Co 4.451 MeV 2^+ analog transition were adequately fit by the normalized DWBA calculations.

The DWBA calculations for this thesis have four advantages over the ones for the University of Colorado data. First, our DWBA calculated differential cross sections were absolute. Bentley's DWBA calculated cross sections for ^{26}Mg, ^{54}Fe and ^{56}Fe (p,n) were normalized to the data. Second, differential cross sections for each transition were calculated at two (three, for ^{54}Fe) energies. Third, the more accurate Ohio University set of neutron optical model parameters was used in the DWBA calculation. Fourth, Z-coefficients were explicitly calculated from Livermore shell model codes and entered into the DWBA calculation. Bentley's ^{26}Mg, ^{54}Fe, and ^{56}Fe (p,n) DWBA calculations used simple nuclear wave functions consisting of one or two configurations. The DWBA calculations of this thesis used more accurate complex nuclear wave functions consisting of as many as ten configurations (with the Z-coefficients determined by the shell model code).

Also, we have made DWBA calculations, not made by Bentley, for (p,n) transitions to the following states: 1.851 MeV 1^+, 9.44 MeV 1^+, and 10.47 MeV 1^+ in ^{26}Al; 5.32 MeV (input as a 1^+ state in the DWBA code) in ^{54}Co; and 1.7203 MeV 1^+ and 2.79 MeV 1^+ in ^{56}Co.

In 1975 J.D. Carlson, C.D. Zafiratos, and D.A. Lind[12] published an analysis of the (p,n) isobaric reaction on 29 of the 35 nuclei in Bentley's thesis. The differential cross sections were analyzed using the Lane optical model with the DWBA in order to derive an optimum U_1 for each nuclide. The parameter U_1 is defined as follows in the Lane model:

$$U = U_0 + 4t \cdot TU_1/A,$$

With U = Lane optical model nucleon-nucleus potential, U_0 = isoscalar potential, U_1 = isospin potential, t = projectile isospin operator, and T = target isospin operator.[13] U_1 was initially deduced from the Becchetti-Greenlees set of proton optical model parameters. The shape of the imaginary part of U_1 was varied to give a good fit to data, while the shape of the real part was kept fixed at that of Becchetti-Greenlees. The real to imaginary well depth ratio was also fixed at the Becchetti-Greenlees value. Carlson *et al.* concluded that "The resulting best-fit form factors had overall strengths 20-30% [illegible] than the Becchetti-Greenlees value. Further, the resulting imaginary part of U_1 was found to peak at a decreasing radius relative to the real part of U_1 with an increasing width as A increased."[14] The best fit U_1's were used to generate a set of self-consistent optical model neutron parameters from the Becchetti-Greenlees proton optical model potentials. These potentials were found to give good agreement with data when used to predict (n,n) cross sections.

In 1974 H.W. Fielding *et al.*[15] described a University of Colorado measurement of the ^{56}Fe(p,n)^{56}Co reaction at a proton bombarding energy of 22.8 MeV. Angular distributions of neutrons corresponding to the ^{56}Co IAS and

the so-called ^{56}Co antianalog state (AAS) were measured for lab angles of 10° to 120°. The DWBA Lane model calculations were compared with measurement for both states. Inclusion of a coherent two-step (p,d) (d,n) process in the calculations resulted in an improved fit of data to calculation compared to a single step process. The two-step process reproduced the IAS angular distribution very well, but failed to reproduce the AAS one. However, the calculations of this thesis accurately reproduced the shapes of the ^{54}Fe and ^{56}Fe IAS angular distributions using only a single step process.

The measured differential cross sections of the work of this thesis involve some transitions that were previously examined by University of Colorado researchers at the proton bombarding energy of 22.8 MeV. Our ^{26}Mg measurements were made at approximately 19 MeV and at 24.97 MeV. Our ^{54}Fe measurements were made at 17.2, 18.6, and 24.6 MeV. Our ^{56}Fe measurements were made at approximately 19 MeV and at 24.59 MeV. Good agreement between absolute differential cross sections for the 22.8 MeV data and our data at around 25 MeV substantiates the reliability of both sets of measurements.

At Tohoku University, H. Orihara and associates[16] stated in 1981 that they had observed the T = 0 and T = 1 components of the Gamow-Teller giant resonance in the ^{54}Fe(p,n)^{54}Co reaction at proton bombarding energies of 32, 35, and 40 MeV. The measurements were made at CM angles between 0° and 90° for 35 MeV, and at several angles for 32 and 40 MeV protons. Two large peaks, at 5.32 MeV and at 10.23 MeV were identified as 1^+; T = 0, and 1^+; T = 1 states, respectively. The authors stated that "The DWBA calculations reproduce very well not only the angular distribution shapes but also the magnitudes of the cross sections for the ground state and the 0.94-MeV state. The calculated angular distribution shapes for the 5.32- and 10.23-MeV states are also in good agreement with the measurements, supporting the 1^+ assignments to those states."[17] The

5.32 MeV state carried approximately 50% of the DWBA calculated $T_<$ GT strength. The 10.23 MeV state carried approximately 40% of the DWBA calculated $T_>$ GT strength.

However, J. Rapaport *et al.*[18] reported in 1983 that their study of the $^{54}Fe(p,n)^{54}Co$ reaction at a proton bombarding energy of 160 MeV failed to show a strong 1^+ state at 5.32 MeV, casting doubt on the Orihara *et al.* assignment. The strong state at about 10 MeV was observed. Evidence in this thesis also suggests that the 5.32 MeV state is not a 1^+ state. Rapaport obtained $^{54}Fe(p,n)^{54}Co$ differential cross sections at the lab angles of 0°, 5.1°, 8.1°, and 11.1°. He also presented 0° cross sections for a number of L = 0 transfers in the $^{54}Fe(p,n)$ reaction.

In the same paper, the $^{56}Fe(p,n)$ reaction was examined at a proton bombarding energy of 160 MeV with neutron detectors at 0° and 4.7°. $^{56}Fe(p,n)$ zero degree cross sections for L = 0 transfers were also obtained. For both $^{54}Fe(p,n)^{54}Co$ and $^{56}Fe(p,n)^{56}Co$, the total experimental GT strength was approximately 50% of the GT strength predicted by the shell model calculations of Bloom *et al.*[19] In deducing this value of 50%, comparison was made between experiment and theory for ^{54}Co excitation energies of 0 to 25 MeV, and for ^{56}Co excitation energies of 0 to 26 MeV.

In 1980, C.D. Goodman *et al.*[20] reported the results of measurements of zero degree (p,n) differential cross sections at the proton energy of 120 MeV for eight nuclei, including ^{26}Mg. The measured $^{26}Mg(p,n)$ differential cross sections to identified low-lying states were the 0.23 MeV 0^+ isobaric analog state, and the three 1^+ states at 1.06 MeV, 1.85 MeV, and 2.07 MeV in ^{26}Al. The 1.85 MeV and the 2.07 MeV states were unresolved, and the combined differential cross section of both states was presented. The squares of the Gamow-Teller matrix elements extracted from experiment for the beta decay of ^{26}Si to the

1.06, 1.85, and 2.07 MeV 1^+ states in ^{26}Al were presented. The square of the calculated Fermi matrix elements of the ^{26}Si beta decay to the ^{26}Al 0.23 MeV 0^+ state was also given. Goodman *et al.* found that after correcting for distortion effects, all the 120 MeV 0° cross sections were "proportional to the squares of the corresponding Fermi and Gamow-Teller matrix elements extracted from beta decay measurements."[21]

S.D. Bloom, C.D. Goodman, S.M. Grimes, and R.F. Hausman[22] used the Livermore shell model codes to calculate the total Gamow-Teller (GT) strength for the ^{26}Mg(p,n)^{26}Al reaction. The PMM interaction[23] was used along with the ^{26}Mg 4p/6h (4 particles/6 holes) shell model approximation. The calculation was normalized by setting the sum of the calculated strength of the first two 1^+ states equal to the sum of the experimentally measured beta decay strengths of ^{26}Si to these two levels. Bloom *et al.* state that "The validity of this comparison is supported by the fact that the shapes of the calculated and observed strength functions agree rather well."[24] The comparison referred to is that of the theoretical GT strength function to the experimental 0° (p,n) measurement, using the normalization described above. The total GT strength observed in the 0° (p,n) measurement at E_p = 120 MeV was found to be somewhat less than 60% of the total calculated GT strength. Approximately 55% of the calculated strength was distributed into the lowest two calculated 1^+; T = 0 states and the first T = 1 state at about 11 MeV.

In 1983 Bloom[25] presented calculations of GT strength functions using the Livermore shell model codes for the nuclei ^{26}Mg, ^{54}Fe, ^{56}Fe, ^{58}Ni, ^{60}Ni, and ^{90}Zr. He found that "in general the agreement between the experimental and theoretical shapes ranges from good to excellent but the theoretical total strengths are too large by a factor of $\frac{1}{0.45}$ to $\frac{1}{0.55}$, the inverse of the so called GT quenching

factor."[26] All the experimental shapes from the (p,n) data presented show the broad regions of $M1$ strength known as the giant GT resonance.

In 1980 W.A. Sterrenburg *et al.*[27] described their work on the $^{26}Mg(p,n)^{26}Al$ reaction for proton energies of 24.6, 35.0, and 45.0 MeV. They obtained differential cross sections for the 0.23 MeV 0^+ state and the 1.06 and 1.85 MeV 1^+ states. The angular distributions ranged from about 15° to 105° (CM) for 24.6 MeV, from about 7° to 110° (CM) for 35 MeV, and from about 10° to 72° (CM) for 45 MeV. DWBA calculations gave reasonable agreement with experimental data. Values of V_τ and $V_{\sigma\tau}$ of the effective interaction were also deduced. The ratio of $\frac{V_{\sigma\tau}}{V_\tau}$ was found to increase with proton bombarding energy in the interval studied.

U.E.P. Berg *et al.*[28] found five 1^+ states in ^{26}Al at 9.44, 9.89, 10.47, 10.83, and 11.21 MeV from the study of the $^{26}Mg(p,n)^{26}Al$ reaction at a proton energy of 35 MeV. The differential cross sections were measured from 7° to 120° (in the laboratory system) using the Michigan State Cyclotron Time-of-Flight Facility. The 1.06 MeV and the 9.44 MeV experimental angular distributions showed good agreement with DWBA calculations. The 3.16 MeV 2^+ angular distribution was given for comparison; it differed in shape from that of the 1^+ states. The integrated cross sections for the five 1^+ states around 10 MeV were compared with the B($M1$) strengths from the (e,e') interaction. Berg *et al.* concluded that the integrated cross sections and the B($M1$) strengths were closely correlated.

R. Madey *et al.*[29] used the Indiana University Cyclotron facility to measure the $^{26}Mg(p,n)^{26}Al$ cross sections at lab angles of 0°, 4°, 8°, and 12° at a proton bombarding energy of 134.4 MeV. They observed two strong peaks at excitation energies in ^{26}Al of 1 and 2 MeV, and a single strong narrow peak at 13.6 MeV. They identified as 1^+, T = 0 states the 1, 2, and 5 MeV

peaks. The peaks between 9 and 11.5 MeV were identified as T = 1 states and the 13.6 MeV peak as the first T = 2; 1^+ level. The shell model calculations of B.H. Wildenthal[30] were compared with the experimental results. Madey *et al.* found that the total experimental GT strength was 60% of that predicted theoretically. He also found that the calculation reproduced the experimental distribution of GT strength into the above four regions of excitation energy (1-2 MeV, around 5 MeV, 9-11.5 MeV, and at 13.6 MeV). The calculated relative GT strength of each region showed good agreement with experiment.

II. EXPERIMENTAL METHODS

A. Overview

The data for this thesis were taken with the LLNL Cyclograaff Neutron Time-of-Flight (TOF) Facility using a 30" (76 cm) cyclotron coupled to a tandem Van de Graaff accelerator (see figures 1a-d). Data were taken at selected proton bombarding energies in the range of 17 to 25 MeV on three metal foil targets of ^{26}Mg, ^{54}Fe, and natural iron. The TOF data were collected in a multichannel analyzer in the Cyclograaff control room and were stored on magnetic tape. At the end of an experiment the tape was read into a Control Data Corporation 7600 mainframe computer. Various programs were then used to obtain excitation energy spectra and cross sections from the TOF data.

Zero degree long flight path data were taken with a large neutron detector to obtain high resolution spectra. For these data the 0° geometry previously used by Wong *et al.*[31] in their 1978 $^{58}Fe(p,n)$ experiment was reproduced.

Sixteen detector TOF angular distributions were also obtained. These spanned 3.5° to 159° in the laboratory system using 15 small detectors (see section II.D below) and the large neutron detector (see section II.E below) which was placed at 23.8° to obtain long flight path high resolution data. For these angular distributions the beam was transported into the neutron TOF pit (see figures 1a and 1d).

B. Description of the Cyclograaff Facility

1. Proton Beam Generation

This section describes the features of the Cyclograaff Facility common to both the 0° and the 16 detector runs. The Cyclograaff Facility contains a Cyclotron Corporation Model CNI-15 30-inch AVF cyclotron (see figure 1b) and

a High Voltage Engineering Corporation Model EN tandem Van de Graaff accelerator (see figure 1c). Although both machines could have been operated independently, all the (p,n) data of this thesis were taken at proton bombarding energies high enough to require their combined use. The term "cyclograaff mode" refers to this combined use as described below. This mode produces a 16 to 27 MeV proton beam.

In the cyclograaff mode an external ion source produces H^- ions from hydrogen gas. These are extracted from the source and sent into the buncher. The buncher imposes a time structure on the ion beam by forming groups of ions which are then injected into the cyclotron during the so-called acceptance period which lasts for 10% of the RF (radio frequency) period. Without the buncher 90% of the ions will be rejected by the cyclotron because of the phase and magnitude of the dee voltage.[32]

The cyclotron accelerates the H^- ions to the fixed energy of 14.8 MeV. These ions then pass to an external RF sweeper. The sweeper passes every n-th group of ions from the cyclotron into the tandem Van de Graaff generator, and discards the intermediate groups. Sweeping results in an H^- beam with greater separation in time between successive pulses than the 40 ns separation produced by the cyclotron. Typically, $\frac{f}{10}$ sweeping was used, where the cyclotron frequency f = 25 MHz. $\frac{f}{10}$ sweeping occurs by passing every tenth group of ions from the cyclotron into the tandem Van de Graaff generator, and discarding the other groups. $\frac{f}{10}$ sweeping produces a pulsed H^- beam with pulses about 2 ns in width separated in time by 400 ns. Thus, the proton beam created from this H^- beam in the tandem Van de Graaff (see below) has pulses separated in time by 400 ns. Without sweeping, low energy neutrons from an earlier burst could arrive at the detector at the same time as high energy neutrons from a later burst. This would produce a meaningless neutron TOF spectrum.

The beam is then injected into the tandem Van de Graaff accelerator. The H^- ions are accelerated to the central positive high voltage terminal, and at the terminal a thin carbon stripper foil removes the electrons from the H^- ions. The resulting protons are repelled by the central terminal and are thus further accelerated; the energy gained is twice the terminal voltage.

2. Zero Degree Measurements

In the 0° runs, the targets were placed at the entrance to the tandem analyzing magnet (see figure 1a) with the large detector at 0° and at a distance of 29.6 m from the target. Upon emerging from the tandem acceleration tank, the proton beam traverses collimators and strikes the target. After exiting the target the beam is bent 90° by the analyzing magnet into a Faraday cup. Unfortunately, accurate charge collection was not available for these runs. "Because of multiple scattering in the target foil and energy analysis by the analyzing magnet, the integrated beam [on the Faraday cup] is less than that incident on the target. Hence the 0° measurements yielded only relative cross sections."[33] A pick-off loop on the cyclotron RF sweeper provided the stop pulses for the zero degree TOF electronics

3. Sixteen Detector Measurements

For the 16 detector runs (see figures 1a and 1d) the beam exited the tandem, was bent 90° by the analyzing magnet, travelled vertically, and was bent another 90° by the bending magnet. The horizontal beam travelled through the "Charged Particle and Gamma Pit" to the "Neutron and Gamma Pit" (also known as the TOF Pit). At the entrance to the TOF Pit, the beam passed through a quadrupole triplet. It continued through a magnetic steerer, collimators, and a carbon foil pick-off into the scattering chamber. The latter contained the

targets in a target changing assembly. The carbon foil pick-off provided the stop pulses for the electronics of the 16 detector runs. A Faraday cup 4.3 m behind the target collected charge and permitted the determination of absolute cross sections.

The 16 detector runs used a combination of 15 small detectors at a distance of approximately 10.75 m from the target, and the large detector at 26.0 m from the target. The small detectors were shielded by 2 m water collimators. The large detector was placed at an angle of 23.8° to the target at the end of a tunnel. As in the 0° runs, the neutrons were incident normal to the cylindrical axis of the large detector.

C. Target Specifications

Here is a tabulation of the target specifications:

Target	$\rho x \left[\frac{mg}{cm^2}\right]$	Isotopic Composition	Size and Shape	Aluminum Frame Diameter
^{26}Mg	3.52±1.11	≥ 90.0% ^{26}Mg	square of side = 2.2 cm	5.5
^{54}Fe	5.54±0.57	96.8% ^{54}Fe 3.0% ^{56}Fe 0.2% other	disk of diameter = 2.6 cm	4.2
^{N}Fe	6.32±0.75	5.8% ^{54}Fe 91.7% ^{56}Fe 2.2% ^{57}Fe 0.3% ^{58}Fe	disk of diameter = 4.4 cm	5.7

Three self-supporting metal foil targets mounted in aluminum frames were used in the experiment. The target thicknesses ρx were determined experimentally by Dr. Calvin Wong at LLNL using the alpha gauge. The gauge measured

the energy loss in the targets of 5.47 MeV alpha particles emitted in the decay of ^{241}Am. One can determine the target thicknesses from the energy loss using a handbook of ranges and stopping powers such as CERN Report No. *CEA-R 3042*. *CEA-R 3042* stopping powers for alphas on aluminum[34] were used for ^{26}Mg, and *CEA-R 3042* stopping powers for alphas on iron[35] were used for both iron isotopes. Alpha gauge measurements were made at the center of the target, 0.64 cm right of center, and 0.64 cm left of center for each target. px was computed for each position, and the value given above is the mean of px for the three positions.

The error is:

$$\sqrt{(0.1\ px)^2 + (sd)^2 + (max/2)^2}\ ,$$

where 0.1 px is the 10% error (as explained in No. 36 of section VI) in the stopping powers in *CEA-R 3042*,[36] sd is the standard deviation in px for the three positions, and max is the maximum difference between the values of px at the three positions. "Size and Shape" refers to the metal foil target. "Aluminum Frame Diameter" is the outer diameter of the aluminum frame in which the metal foil target is mounted. The isotopic composition of ^{N}Fe is from the *Handbook of Chemistry and Physics*.[37]

D. Small Detector Specifications

The small detectors were each 11.4 cm in diameter by 5.1 cm long cylinders of NE213 liquid scintillator connected by a light pipe to a RCA 8575 photomultiplier tube. Neutrons entered the scintillator parallel to the cylindrical axis. The liquid scintillator contained a bubble approximately equal to 4% of its volume; correction for the bubble was built into the cross section calculating code GRIND.

The Area x Efficiency (AE) curves at 1 x Hi Na ("one times high sodium"), and 2 x Hi Na ("two times high sodium") biases, are shown in figures 2 and 3. See section III.G below for an explanation of 1 x Hi Na and 2 x Hi Na biases. The 1 x Hi Na curve was created as follows: The efficiency code EFFIC generated a 1 x Hi Na AE curve. The curve was flattened for neutron energies greater than 20 MeV; this flattened curve was then adopted as the small detector 1 x Hi Na AE curve (figure 2).

The 2 x Hi Na AE curve was created as follows: EFFIC was used to generate a 2 x Hi Na AE curve. The curve was modified (as described below) for neutron energies greater than 18.1 MeV; this modified curve was then taken as the small detector 2 x Hi Na AE curve (figure 3).

The $T(d,n)^4He$ reaction was used to calibrate the detector at 2 x Hi Na for neutrons with energy greater than 18.1 MeV. A tritium gas cell in the TOF pit was bombarded with deuterons whose energies ranged from 7 to 12 MeV in 1 MeV increments. Neutron spectra were obtained, and the area of the D-T peak was determined by the peak fitting routine NDFOXE for each of the 16 detectors at each deuteron energy. For a particular deuteron energy, the NDFOXE set of counts from the 16 peak areas were input into the code GRIND. For each detector, GRIND calculated both the energy of the neutrons at that angle and the differential cross section. In calculating differential cross sections, GRIND used a built-in 2 x Hi Na AE table calculated with EFFIC. This table also included compensation for air absorption of neutrons along the 10.75 m flight path.

GRIND calculated differential cross sections were compared with those produced by the code NPCS. NPCS used a Legendre polynomial expansion with Drosg's[38] Legendre coefficients to generate precise differential cross sections. The built-in 2 x Hi Na AE table was then modified for neutron energies greater

than 18.1 MeV to make the GRIND calculated cross sections agree with the accurate NPCS values. This modified AE table constituted the small detector 2 x Hi Na AE; it is plotted in figure 3.

E. Large Detector Specifications

1. Physical Description

The large detector (figure 4) had a Nuclear Enterprises Inc. type BA2 cylindrical aluminum scintillation tank with internal dimensions of 25.4 cm in length and 12.5 cm in diameter. Its inner cylindrical surface was thinly coated with white titanium dioxide reflector and its two viewing windows were made of glass. The tank was filled at the factory with NE213 liquid scintillator. A concealed PTFE tube was wrapped around the circumference of the tank and served as an expansion chamber for the liquid scintillator. Two RCA 8854 photomultiplier tubes viewed the tank through lucite light pipes (lucite has a low UV absorption coefficient). The light pipes were wrapped with white plastic tape and the photomultiplier tubes were wrapped with electrically insulating plastic. The tubes and the tank were clamped to an aluminum channel holder to keep the assembly rigid. The entire detector was then wrapped with layers of black plastic tape to make it lightproof. The pins at the base of each photomultiplier tube were plugged into a socket on a small metal box. The resistor chain (see figures 5a and 7) was wired to the socket. The box also contained the dynode signal preamplifier (figure 5b), inputs for the high voltage and the preamplifier power, and outputs for the anode and (preamplified) dynode signals.

2. Efficiency

All measurements with the large detector in this thesis were done with the detector axis perpendicular to the incident neutrons. The AE was determined experimentally using the $T(d,n)^4He$ and the $D(d,n)^3He$ differential cross sections. These cross sections were generated by the code NPCS using Drosg's[39] Lengendre coefficients.

For the D-D runs, a beam of deuterons was directed into a deuterium gas cell in the TOF pit. The center of the gas cell was 10.95 m from the center of the 3.5° small detector, and 4.53 m from the center of the large detector. The large detector was placed at the same angle as the 3.5° small detector. Measurements were made using deuterons with bombarding energies in the range of 4 to 10 MeV in 1 MeV increments, and at 12 MeV.

For the D-T runs, a beam of deuterons was directed into a tritium gas cell in the TOF pit. The center of the gas cell was 10.75 m from the center of the 3.5° small detector, and 4.33 m from the center of the large detector. The large detector was placed at the same angle as the 3.5° small detector. Measurements were made using deuterons with bombarding energies in the range of 5 to 12 MeV in 1 MeV increments.

For both the D-D and the D-T runs, TOF neutron spectra were obtained at each deuteron energy. The small detector bias was set at 2 x Hi Na for all runs and measurements were made with the large detector at 1 x, 2 x, 3 x, and 4 x Hi Na bias. The counts in the neutron peaks for both detectors were determined by NDFOXE.

The relationship between the differential cross section at 3.5°, and the counts in the neutron peak is:

$$(DTC)\cdot(Counts) = \frac{Q\cdot N\cdot \ell\cdot \frac{d\sigma}{d\Omega}(3.5°)\cdot(AE)}{(1.602E-13)\cdot R^2}$$

where DTC is the dead time correction, Counts is the NDFOXE area of the neutron peak, Q is the total charge collected in μC, N is the number of atoms per cm^3 in the gas cell, ℓ is the length of the gas cell, $\frac{d\sigma}{d\Omega}(3.5°)$ is the 3.5° differential cross section, AE is the detector Area x Efficiency, and R is the distance between the center of the gas cell and the center of the detector.

Application of this formula to the small detector gives:

$$(DTC_S)\cdot(Counts_S) = \frac{Q\cdot N\cdot \ell\cdot \frac{d\sigma}{d\Omega}(3.5°)\cdot(AE_S)}{(1.602E{-}13)\cdot R_S^2}.$$

Similarly, for the large detector:

$$(DTC_L)\cdot(Counts_L) = \frac{Q\cdot N\cdot \ell\cdot \frac{d\sigma}{d\Omega}(3.5°)\cdot(AE_L)}{(1.602E{-}13)\cdot R_L^2}.$$

Dividing gives:

$$\frac{(DTC_L)\cdot(Counts_L)}{(DTC_S)\cdot(Counts_S)} = \frac{(AE_L)\cdot R_S^2}{(AE_S)\cdot R_L^2}.$$

Thus,

$$AE_L = \frac{(DTC_L)\cdot(Counts_L)\cdot(R_L^2)\cdot(AE_S)}{(DTC_S)\cdot(Counts_S)\cdot(R_S^2)}.$$

Since the small detector AE_S includes air absorption, but the large detector AE_L does not, AE_L must be corrected as follows:

$$AE_L = \frac{(DTC_L)\cdot(Counts_L)\cdot(R_L^2)\cdot(AE_S)}{(DTC_S)\cdot(Counts_S)\cdot(R_S^2)\cdot(I/I_o)}.$$

(I/I_o) was computed analytically with the formula:

$$(I/I_o) = \exp(-[\sigma_{O_2,\,total}\cdot N_{O_2} + \sigma_{N_2,\,total}\cdot N_{N_2}]L),$$

with $N_{O_2} = 1.126E{+}19\ \frac{O_2\ atoms}{cm^3}$, $N_{N_2} = 4.197E{+}19\ \frac{N_2\ atoms}{cm^3}$, assuming that air consists of 78.084% nitrogen, and 20.946% oxygen by volume. The total cross

sections $\sigma_{N_2,\ total}$ for nitrogen,[40] and the total cross sections $\sigma_{O_2,\ total}$ for oxygen,[41] are taken from *UCRL-50400* at the energy bin closest to the actual neutron energy. L is the large detector flight path during the calibration.

Finally, the measured Area x Efficiencies were plotted, and smooth curves were drawn through the data points. These smooth curves were used as the Area x Efficiency for the (p,n) experiments using the large detector. Specifically, the values of AE read off of these smooth curves were used in the data analysis programs GRIND and TOFFEE (see Appendix: Computer Codes). For each bias, these programs used a table of AE values for neutron energies of E_n = 0.1 to 30.0 MeV in 0.1 MeV increments. Since measurements of AE for the large detector were made at a limited number of neutron energies, smooth curves were drawn to provide complete tables of AE values. See figures 13-16 for the AE curves; note that calculations of AE with two Monte Carlo codes are also plotted for comparison. The Monte Carlo codes are described in the Appendix.

3. Time Resolution

The large detector time resolution was 3 ns full-width at half-maximum (see below) for the 0° runs of July 1981. This was measured with a ^{22}Na source and the electronics of figure 6. ^{22}Na decays to ^{22}Ne by positron emission. The positrons slow down in the source package, encounter an atomic electron and annihilate, producing two 0.511 MeV gamma rays at 180° to each other. The circuit of figure 6 produced a peak in the multichannel analyzer spectrum corresponding to the coincident detection of the two gamma rays.

The full-width at half-maximum of the peak multiplied by the time per channel is the time resolution of the entire system. A system with perfect time resolution would produce counts in only a single channel since the start and stop pulses from the two gamma rays would always have the same separation in time.

In our system, the start and stop pulses do not have a constant separation in time due to several factors. First, the large size of the scintillator results in the escape of light, and in the spread of light transit times (due to reflections off the scintillator walls). Second, there are variations in the rise time of the large detector anode pulses due to fluctuations in the light response of the scintillator and in the number of photoelectrons produced by the cathodes of the photomultiplier tubes. Third, there are variations in the small detector anode pulse rise times for the same reasons. Fourth, there is noise in the electronics.

The 3 ns time resolution measurement of the large detector (and its electronics) assumes a negligible contribution by the small detector and its constant fraction discriminator to the overall time resolution. This assumption is justified by a later measurement using the circuit of figure 6 with the large detector replaced by a small detector (with a plastic scintillator), and with the fan-in removed. The time resolution obtained ranged from 0.6 to 0.8 ns depending on the CFDs' lower level discriminator settings (0.8 ns was obtained with both discriminators set to 0).

Before the April 1983 16 detector runs, the large detector time resolution was improved (as discussed below) by the base circuit modification shown in figure 7, and by the use of the electronics of figure 8. The large detector constant fraction discriminators (CFDs) had their lower level discriminators set to approximately $\frac{1}{4}$ of low Na bias. The small detector of figure 8 had its CFD lower level discriminator set to about $\frac{3}{7}$ of low Na bias. Measurement of the time resolution in July 1984, using the large detector April 1983 fast signal electronics gave 1.7 ns at the center of the detector. However, the time resolution at the end of the scintillator tank near phototube 1 was 1.7 ns, and near phototube 2 it was 1.9 ns. This difference was probably due to a small difference in the rise time of the anode pulses from the two tubes. The count rate with the

source near phototube 2 was also less than the count rate with the source near phototube 1. Also, phototube 1 was run at a higher voltage than the other tube. The voltage and count rate differences indicated that the gain of phototube 1 was less than phototube 2.

The improvement in time resolution from 3.0 to 1.7 ns is due to several factors. First, the detector bases were modified to increase the voltages at the first few dynodes. This decreases the transit time of the electrons through the photomultiplier tube, which decreases the rise time of the signal and yields better time resolution. Also, increasing the voltage at the first few dynodes increases the number of secondary electrons emitted by the dynodes. Since the total number of electrons arriving at the anode is increased, the fluctuations in this total number are a smaller percentage of the total. This diminishes the statistical anode signal fluctuations, and improves the time resolution. Second, better constant fraction discriminators (CFDs) were used. Different CFD delays were tried, and the one (5 ns) yielding the best time resolution was selected. Each CFD walk adjustment was set so that all the bipolar signals crossed the zero crossing baseline as near to the same time as possible. Each CFD lower level discriminator was set below the slow bias, but high enough to improve time resolution. A description of the function of the constant fraction discriminator is given below in section II.E.4.

Third, a meantimer was used. Since we have a long scintillator, light from an event occurring away from the center takes longer to reach one photomultiplier tube than the other. Therefore, the fast (anode) signals from each tube will not be in coincidence. The meantimer sends the two constant fraction discriminator output pulses (each produced by one tube) down a delay line. The delay line has 17 pickoff points yielding a resolution of 0.5 ns. When the two pulses overlap a single logic pulse is generated. The input-output delay of the mean-

timer is $0.5t_d$ + 13 ns, where t_d is the time delay between the two input pulses. This creates a pulse that is independent of the location of the event in the scintillator. Therefore, the time interval between the event and the generation of the meantimer output pulse is constant and independent of the event's position in the scintillator.

Finally, the voltages to the photomultiplier tubes and the cable lengths from the bases to the CFDs were adjusted to produce anode signals that were approximately equal in magnitude and arrival time.

4. Electronics

The electronics for the large detector 0° runs of July 1981 are diagrammed in figure 9. The preamplifier power supply is located in the TOF Pit near the detector. High voltage is supplied to the detector by cables from power supplies in the control room. The anode and dynode signals from both photomultiplier tubes are sent through cables to the dual fan-in in the control room. The sum of the anode signals from the fan-in constitutes the fast signal; the sum of the dynode signals from the fan-in constitutes the slow signal.

The fast signal amplitude is reduced by a factor of 2 by the 2 x Attenuator. The signal passes to the TFA (see figure 9 for a key to the abbreviations) where it is amplified and sent to the CFD. The CFD triggers on a constant fraction of the input pulse independent of amplitude. It provides a negative logic pulse with a baseline crossover independent of the amplitude of the input pulse. The CFD has two identical negative pulse outputs. One pulse is sent to the TOF Delay Gate and the other is sent into 900 ns of RG58 delay cable.

Consider the pulse sent to the TOF Delay Gate. The TOF Delay Gate passes the delayed pulse to the start input of the TOF TAC. The TOF TAC stop pulse is generated by the cyclotron RF. The TOF Delay Gate is adjusted to delay the

start pulse in order to place the time interval between the start and stop pulses within the range of the TAC. The TAC generates a pulse with amplitude proportional to the time interval between the start and stop pulses. The signal from the TOF TAC enters the TOF Delay Amp, which delays it without changing its amplitude, and passes it to the TOF ADC. The TOF Delay Amp is used to make the TOF TAC output pulses arrive at the ADC at the same time as the Gate pulses. The ADC digitizes the TAC analog pulses; analog pulses appear as counts in the multichannel analyzer.

The other logic signal from the CFD is sent down 900 ns of cable to delay it. A TFA then amplifies the signal to compensate for the loss in the cable. The PE Delay Gate allows adjustment of the delay of the logic pulse leading into the PE TAC/SCA start. The TAC output can be plugged into the ADC2 Delay Amp. This delay amp is connected to ADC2 which is used to display the PE spectra (or the pulse height spectra, if the unipolar output of the DDL Amp is connected to the ADC2 Delay Amp).

The slow signal passes into the DDL Amplifier. This component generates amplified bipolar and unipolar pulses whose rise time is a function of the rise time of the summed slow signal. The rise time of the total integrated light output of a gamma ray is about $\frac{1}{13}$ of that of a neutron because the scintillator responds differently to gamma rays than to neutrons. That is, neutrons interact primarily with protons in the scintillator, and gamma rays interact with electrons. The amount of light emitted, and its maximum intensity, differ for neutrons and gamma rays. Therefore, the bipolar DDL Amplifier output pulses will have one shape for gamma rays, and a different shape for neutrons. This is also the case for the unipolar output. This difference in pulse shape results in the bipolar gamma ray pulses crossing the zero baseline at an earlier time than the bipolar neutron pulses.

The bipolar pulses pass to the Timing SCA. The lower level discriminator on the Timing SCA is set to reject pulses with amplitudes below a certain threshold. This discriminator is used to set the pulse height bias. It rejects pulses corresponding to gamma ray energies below a certain value, and to neutron energies below a corresponding value. Since the Timing SCA triggers at the zero baseline crossing, its output due to gamma rays occurs before that due to neutrons.

The PE TAC/SCA output thus produces low amplitude pulses due to gamma rays, and higher amplitude pulses corresponding to neutrons. The lower level discriminator on the PE TAC/SCA is used to cut out most of the low amplitude gamma ray pulses. The SCA output of the PE TAC/SCA passes to the ADC Delay Gate. The TOF TAC is thus gated by slow pulses that satisfy the following two conditions: First, the pulse must be of a minimum pulse height; this corresponds to rejecting neutrons below a certain energy (and also gamma rays below the corresponding energy). Second, the pulse must produce a PE SCA pulse above the set threshold, thus indicating it as a neutron-induced event.

The electronics for the large detector 23.8° runs are diagrammed in figure 10. For these runs, the large detector is located at the bottom of a manhole. The neutrons reach the detector through a tunnel from the pit. A NIM bin containing the Quad CFD, preamplifier power supply, meantimer, linear fan-in, and photomultiplier tube high voltage power supplies is located in the manhole. The anode signals are fed into the CFDs whose output is connected to the meantimer. The meantimer output is fed into the control room by cable and constitutes the fast signal. The dynode signals are fed into the linear fan-in. The fan-in output is fed into the control room and is the slow signal.

The same electronics as in the 0° runs are used to process the slow and fast signals with a few minor differences. Three ADCs are permanently hooked up to display TOF, pulse height, and PE spectra in the multichannel analyzer.

The PE and pulse height spectra are not displayed simultaneously in the 0° runs. In the 23.8° runs the anode signals go to independent channels of a Quad CFD. The CFD outputs pass to the meantimer (see section II.E.3 above) and are then split with one part going to the PE Delay Gate.

The large detector photomultiplier tube high voltages for the July 1981 set of 0° (p,n) runs were −1,799 V for photomultiplier tube 1, and −1,580 V for photomultiplier tube 2. For the April 1983 set of (p,n) runs (with the large detector at 23.8°) the high voltages were −2,190 V for photomultiplier tube 1, and −1,996 V for photomultiplier tube 2.

F. Electronics of the Array of 15 Small Detectors

Since the small detector electronics have been described elsewhere,[42] only a block diagram is presented (see figure 11).

G. Pulse Height Bias

The pulse height biases in this thesis are described as being set at some multiple of Hi Na such as 1 x Hi Na, 2 x Hi Na, etc. This section will explain the meaning of the term n x Hi Na, where n = 1, 2, 3, or 4. The method of setting biases also will be elucidated.

Biases are set by placing a ^{22}Na source near the detector. ^{22}Na decays by positron emission to the 1.27 MeV 2^+ excited state of ^{22}Ne. The 2^+ state decays to the ^{22}Ne 0^+ ground state by the emission of a gamma ray with 1.27 MeV energy. Positron annihilation produces two 0.511 MeV gamma rays at 180° to each other. Thus the ^{22}Na source produces gamma rays of two energies: 0.511 MeV and 1.27 MeV.

The gamma rays Compton scatter off electrons in the scintillator. The maximum energy that the 0.511 MeV gamma ray can impart to an electron is

0.341 MeV. The maximum energy that the 1.27 MeV gamma can impart is 1.062 MeV. The low energy gamma can thus produce Compton electrons with energies from nearly 0 to 0.341 MeV. The high energy gamma can produce Compton electrons with energies from nearly 0 to 1.062 MeV. This Compton recoil spectra produces the pulse height distribution of figure 12. The 1 x HI Na bias is set on the 1.062 MeV edge as shown. This bias corresponds to rejecting neutrons of energy below 3.3 MeV. The 2 x HI Na bias corresponds to 2.12 MeV electrons or 5.4 MeV neutrons. The 3 x HI Na bias corresponds to 3.18 MeV electrons or 7.2 MeV neutrons. The 4 x HI Na bias corresponds to 4.24 MeV electrons or 9.0 MeV neutrons. Since the pulse height discriminator is linear, the 2 x, 3 x, and 4 x HI Na biases correspond to 2 x, 3 x, and 4 x the discriminator setting.

III. RESULTS

A. Data Analysis

1. Time of Flight Spectra

Two typical plots of TOF spectra are shown in figures 21-22. Both are from the ^{56}Fe(p,n) run with the proton bombarding energy of 19.11 MeV. Figure 21 is the TOF spectrum of the large detector at 23.8°, and figure 22 is the TOF spectrum of the 32.3° small detector. The principal ^{56}Co states are indicated on the plots. The TOF spectra for each of the small detectors consisted of 512 channels. The TOF spectra for the large detector consisted of 1024 channels for 23.8°, and 2048 channels for 0°.

2. Differential and Angle-Integrated Cross Sections

Figures 31 to 56 are graphs of the experimentally determined ^{26}Mg, ^{54}Fe, and ^{56}Fe(p,n) center of mass differential cross sections. Below each graph is a table of the plotted experimental differential cross sections and their errors. The integrated cross section over all angles, exp. σ_{total}, is also presented when available; it is obtained by use of the code LEGENDRE to fit a sum of Legendre polynomials to the data points. Curves of DWBA calculated differential cross sections are superimposed on many of the experimental differential cross section plots (see section III.C below). The differential cross sections from R.F. Bentley's Ph.D. thesis[43] and those of this paper are compared for seven transitions (figures 57-63). For the 1.0578 MeV 1^+ state in ^{26}Al, a comparison (figure 57) was made of the differential cross sections of this thesis with those of Bentley[44] and Sterrenburg *et al.*[45] Reasonable agreement was obtained between our differential cross sections and those of Bentley and Sterrenburg.

Differential cross sections were obtained either by the use of a planimeter, or by the use of the computer code GRIND. These two methods are described below. The method used in a particular graph is indicated by the words "planimeter" or "GRIND." Circular symbols were used exclusively on planimeter plots, and asterisks were used exclusively on GRIND plots. Triangular symbols represent differential cross sections obtained with the large detector.

All of the differential cross sections from 3.5° to 159° were obtained from the April 1983 series of runs. Zero degree ^{26}Mg and ^{56}Fe(p,n) differential cross sections were measured with the large detector in July 1981. The 0° data were taken at a proton bombarding energy of 19 MeV (neglecting proton energy loss in the target). See section III.A.5 below for a discussion of the 0° data proton energy loss.

3. Planimeter Method

The code TOFFEE is applied to the raw TOF plots. This code has appropriate internal AE tables specific to the detector and its bias. The code converts the raw TOF data into a plot of $\frac{d^2\sigma}{d\Omega dU}$ vs. U, where $\frac{d^2\sigma}{d\Omega dU}$ is the center of mass double differential cross section in $\frac{mb}{sr\text{-}MeV}$, and U is the excitation energy of the residual nucleus in MeV. The code also computes and plots error bars for each double differential cross section. The code can average double differential cross sections over two channels and compute the appropriate error. All of the large detector TOFFEE plots displayed in section VII are averaged with the exception of figure 24. TOFFEE plots for the large detector at 23.8° are displayed for the ^{26}Al, ^{54}Co, and ^{56}Co residual nuclei at all the proton bombarding energies (figures 23-30). States are identified from the energy level diagrams of Lederer *et al.*[46] and Endt[47], and from the work of

U.E.P. Berg *et al.*[48] (see figures 17-20). Note that the approximate locations of many levels (from the energy level diagrams) are indicated on the TOFFEE plots, although these levels may not have been resolved.

Differential cross sections were extracted from the TOFFEE plots in the following manner: A smooth background was hand drawn through the spectrum, and smooth curves were hand drawn through the peaks. For closely spaced peaks, curves of the same width and shape were drawn, and the division of counts between the peaks was carefully made to conserve the total counts under the peaks. The high resolution large detector plots were used to determine the energy spacing between peaks for the low resolution plots if necessary. An example of the hand drawn peaks is figure 24. A planimeter was moved around the boundary of each peak, and the area in square inches was extracted. The planimeter was then used to measure the area in square inches of a 1 $\frac{mb}{sr\text{-}MeV}$ rectangle on the TOFFEE plot. This enabled us to convert the area of a peak in square inches to the differential cross section in $\frac{mb}{sr}$. All differential cross sections obtained in this manner were absolute with the exception of the zero degree 19 MeV data. The zero degree ^{26}Mg(p,n) differential cross sections were obtained by setting the differential cross section of the zero degree 0.00 MeV-0.23 MeV-0.42 MeV ^{26}Al triplet equal to the 3.5° triplet differential cross section. Similarly, the zero degree ^{56}Fe(p,n) differential cross section was obtained by setting the 3.59 MeV ^{56}Co isobaric analog state differential cross section equal to the 3.5° differential cross section.

The error of a differential cross section was the sum in quadrature of three errors. The first was the planimeter error (PL ERROR) taken as the standard deviation of the measurements of area for the particular peak. The second was the background error (BKG ERROR) which was the area of a small region at the base of the peak (see figure 24). The area of this small region is an estimation of

the error in the area of the peak due to the uncertainty in drawing the background. The third error is the statistical error (ST ERROR) computed from the raw TOF data plot in the following manner. A background is drawn through the TOF data. For a particular peak, we obtain the number of counts in the peak S, the number of counts in the background B, and the combined counts S+B. The statistical error of the combined counts is $\sqrt{(S+B)}$. We can approximate the statistical error of the same peak in the TOFFEE plot by multiplying by $(\frac{AREA}{S})$, where AREA is the area of the TOFFEE peak. Thus, the statistical error becomes approximately:

$$\text{ST ERROR} = \sqrt{(S+B)} \cdot (\frac{AREA}{S}).$$

The total error for the differential cross section is thus:

$$\text{TOTAL ERROR} = \sqrt{(\text{ST ERROR})^2 + (\text{BKG ERROR})^2 + (\text{PL ERROR})^2} \quad .$$

The minimum total error was set at 7.5% of the differential cross section.

4. GRIND Method

The code GRIND was used to obtain the $^{54}Fe(p,n)$ differential cross sections at proton bombarding energies of 17.2 and 18.6 MeV. The curve fitting routine NDFOXE was used to fit Gaussian shapes to the TOF data and to compute the integrated counts under the peak and its error. GRIND contained the Area x Efficiency (AE) tables specific to the detector and its bias. GRIND generated differential cross sections from the NDFOXE integrated counts and errors. The error in these differential cross sections was the combination of the statistical error in the counts in the peak, and the χ^2 fit of the Gaussian curve to the peak. The minimum error computed by GRIND was 7.0% of the differential cross section.

5. Energy Loss in the Targets

The proton bombarding energies given in the differential cross section plots for the data of this thesis include the proton energy loss in the targets. The formula for the energy loss DE of a proton of energy $E_{p'}$(machine) in a target of thickness ρx is:

$$DE = \left[-\frac{dE}{d(\rho x)} \Big|_{E_{p'}(\text{machine})} \right] \frac{\rho x}{2},$$

where $-\frac{dE}{d(\rho x)} \Big|_{E_{p'}(\text{machine})}$ is the stopping power for a proton of energy $E_{p'}$(machine). The proton can react with a target nucleus anywhere in the target. This formula assumes that on the average, a proton passes through one half of the target before reacting. The bombarding energy E_p of the proton after energy loss in the target is:

$$E_p = E_{p'}(\text{machine}) - DE$$

Here is a table of the E_p for the experimental (p,n) runs of this thesis:

Target	$E_{p'}$(machine) [MeV]	$-\frac{dE}{d(\rho x)}$ [MeV-cm^2/gm]	ρx [gm/cm^2]	DE [Mev]	E_p [MeV]
^{26}Mg	19.16	2.030E+01	3.52E-03	3.57E-02	19.12
^{26}Mg	25.00	1.645E+01	3.52E-03	2.90E-02	24.97
^{54}Fe	17.25	1.870E+01	5.54E-03	5.18E-02	17.20
^{54}Fe	18.65	1.762E+01	5.54E-03	4.88E-02	18.60
^{54}Fe	24.64	1.423E+01	5.54E-03	3.94E-02	24.60
^{N}Fe	19.16	1.726E+01	6.32E-03	5.45E-02	19.11
^{N}Fe	24.64	1.423E+01	6.32E-03	4.50E-02	24.60

The values of $E_{p'}$(machine) were obtained from the cyclograaff operating personnel during the course of the experimental runs. The *CEA-R 3042* stopping powers for protons on aluminum[49] were used for ^{26}Mg, and the stopping

powers for protons on iron were used for both iron isotopes[50] ($-\frac{dE}{d(\rho x)}$ is called the stopping power). The values of ρx are taken from section II.C.

6. Total Charge Collected

Here is a table of the total charge collected for each experimental (p,n) run. E_p is the proton bombarding energy (taking into account the energy loss in the target). Since charge collection was not available for the zero degree runs, the phrase "N/A at 0°" appears in the Total Charge Collected column.

Target	E_p [MeV]	Total Charge Collected [μC]
^{26}Mg	19.00	N/A at 0°
^{26}Mg	19.12	3700.
^{26}Mg	24.97	4719. (Small Detectors)
^{26}Mg	24.97	5298. (Large Detector)
^{54}Fe	17.20	2990.
^{54}Fe	18.60	2007.
^{54}Fe	24.60	2920.
^{N}Fe	18.95	N/A at 0°
^{N}Fe	19.11	3725.
^{N}Fe	24.59	1680.

The 24.97 MeV ^{26}Mg(p,n) run has greater charge collection with the large detector alone than with the array of 15 small detectors for the following reason: The run initially accumulated charge with all the detectors at 2 x Hi Na bias. The run was stopped, and the data collected by the 15 small detectors were erased; the data collected by the large detector were retained. The small detector biases were reset to 1 x Hi Na (the large detector bias was unchanged), and data were

acquired by all 16 detectors. This gave a greater total charge collection for the large detector at the end of the run.

7. Energy Resolution

The full-width at half-maximum of a single prominent isolated peak in a TOFFEE energy spectrum is used as a measure of the energy resolution of its peaks. The FWHM was obtained for selected peaks in TOFFEE spectra for the large detector and the 3.5° small detector. The peaks selected were those produced by the $^{26}Mg(p,n)^{26}Al$ 1.06 MeV 1^+, the $^{54}Fe(p,n)^{54}Co$ 0.94 MeV 1^+, and the $^{56}Fe(p,n)^{56}Co$ 3.59 MeV 0^+. E_p is the proton bombarding energy, taking into account the proton energy loss in the target.

Reaction	E_p [MeV]	Detector	Detector Angle [Degrees in Lab]	Peak	FWHM [MeV]
$^{26}Mg(p,n)^{26}Al$	19.00	Large	0.	1.06 MeV 1^+	0.16
$^{56}Fe(p,n)^{56}Co$	18.95	Large	0.	3.59 MeV 0^+	0.18
$^{26}Mg(p,n)^{26}Al$	19.12	Small	3.5	1.06 MeV 1^+	0.32
$^{26}Mg(p,n)^{26}Al$	19.12	Large	23.8	1.06 MeV 1^+	0.19
$^{26}Mg(p,n)^{26}Al$	24.97	Small	3.5	1.06 MeV 1^+	0.41
$^{26}Mg(p,n)^{26}Al$	24.97	Large	23.8	1.06 MeV 1^+	0.26
$^{54}Fe(p,n)^{54}Co$	17.20	Small	3.5	0.94 MeV 1^+	0.15
$^{54}Fe(p,n)^{54}Co$	17.20	Large	23.8	0.94 MeV 1^+	0.097
$^{54}Fe(p,n)^{54}Co$	18.60	Small	3.5	0.94 MeV 1^+	0.21
$^{54}Fe(p,n)^{54}Co$	18.60	Large	23.8	0.94 MeV 1^+	0.14
$^{54}Fe(p,n)^{54}Co$	24.60	Small	3.5	0.94 MeV 1^+	0.29
$^{54}Fe(p,n)^{54}Co$	24.60	Large	23.8	0.94 MeV 1^+	0.19

Energy Resolution (cont'd)

Reaction	E_p [MeV]	Detector	Detector Angle [Degrees in Lab]	Peak	FWHM [MeV]
$^{56}Fe(p,n)^{56}Co$	19.11	Small	3.5	3.59 MeV 0^+	0.26
$^{56}Fe(p,n)^{56}Co$	19.11	Large	23.8	3.59 MeV 0^+	0.19
$^{56}Fe(p,n)^{56}Co$	24.59	Small	3.5	3.59 MeV 0^+	0.35
$^{56}Fe(p,n)^{56}Co$	24.59	Large	23.8	3.59 MeV 0^+	0.23

8. Biases

Here is a table of the large detector and small detector biases for the experimental runs. All 15 of the small detectors were set to the same bias as indicated (i.e., 1 x Hi Na or 2 x Hi Na). The method of setting biases has been previously discussed in section II.G above.

Reaction	E_p [MeV]	Detector	Detector Angle [Degrees in Lab]	Bias [x Hi Na]
$^{26}Mg(p,n)^{26}Al$	19.00	Large	0.	2
$^{56}Fe(p,n)^{56}Co$	18.95	Large	0.	2
$^{26}Mg(p,n)^{26}Al$	19.12	Small	3.5	2
$^{26}Mg(p,n)^{26}Al$	19.12	Large	23.8	2
$^{26}Mg(p,n)^{26}Al$	24.97	Small	3.5	1
$^{26}Mg(p,n)^{26}Al$	24.97	Large	23.8	3
$^{54}Fe(p,n)^{54}Co$	17.20	Small	3.5	1
$^{54}Fe(p,n)^{54}Co$	17.20	Large	23.8	2
$^{54}Fe(p,n)^{54}Co$	18.60	Small	3.5	2

Biases (cont'd)

Reaction	$\bar{E}_p$ [MeV]	Detector	Detector Angle [Degrees in Lab]	Bias [x Hi Na]
$^{54}Fe(p,n)^{54}Co$	18.60	Large	23.8	2
$^{54}Fe(p,n)^{54}Co$	24.60	Small	3.5	2
$^{54}Fe(p,n)^{54}Co$	24.60	Large	23.8	2
$^{56}Fe(p,n)^{56}Co$	19.11	Small	3.5	2
$^{56}Fe(p,n)^{56}Co$	19.11	Large	23.8	2
$^{56}Fe(p,n)^{56}Co$	24.59	Small	3.5	2
$^{56}Fe(p,n)^{56}Co$	24.59	Large	23.8	3

9. Comparison with Bentley and Sterrenburg

Comparison of our differential cross sections with those of Bentley's[51] in figures 57–63 shows good agreement in shape and magnitude for all except the 1.06 MeV 1^+ state of ^{26}Al. In the latter, the shape of our differential cross sections agrees with Sterrenburg[52] and Bentley, but ours are lower than both. The cause of this discrepancy may be the difference in bombarding energies.

10. Ground State Q-Values

The experimental ground state (g.s.) Q-values from *Nuclear Reaction Q-Values*[53] are listed below for the three (p,n) reactions of this thesis.

Reaction	Q-Value [MeV]
$^{26}Mg(p,n)^{26}Al$ g.s.	-4.7858
$^{54}Fe(p,n)^{54}Co$ g.s.	-9.0339
$^{56}Fe(p,n)^{56}Co$ g.s.	-5.3568

B. Shell Model Calculations

1. Overview

The Livermore shell model code (also known as the Vector Method Code) was used to compute Z-coefficients for the DWBA calculations. Manifolds of states were also created for ^{26}Al, ^{54}Co, and ^{56}Co. The energies, spins, and parities of these states were compared with tabulated values (see figures 17-20). The same shell model calculations also generated Gamow-Teller strength functions for the ^{26}Mg, ^{54}Fe, and ^{56}Fe(p,n) reactions. Comparison of these strength functions with high proton bombarding energy experiments has been made by S.D. Bloom[54] with good agreement; Bloom also describes the generation of the strength functions in detail.

Since the Livermore shell model code has been described in the literature,[55-57] we present only a brief outline of the four main ingredients of a typical calculation.[58] First, there is a model space {P} for the parent state vector |P> consisting of a set of single particle shell model orbitals and an excitation restriction. The excitation restriction limits the number of particles (p) and holes (h) allowed in the model space. The second ingredient is a Hamiltonian (in the second quantized representation); the PMM Hamiltonian[59] was used in the shell model calculations of this thesis. The third ingredient is a transition operator. For example, our Gamow-Teller strength function calculations used the Gamow-Teller operator (GT) with:

$$(GT) = g_A \sigma \tau^-.$$

The fourth and final component is the model space {D} for the daughter state vectors |D>.

2. $^{26}Mg(p,n)^{26}Al$ Calculations

A ^{26}Mg ground state wave function |g.s.> was created having as its model space an ^{16}O core and the [$1d_{5/2}$, $2s_{1/2}$, $1d_{3/2}$] orbitals with the 4p/6h (4 particles/6 holes) excitation restriction. The holes were in the $1d_{5/2}$ orbital, and the particles were in the $2s_{1/2}$ and $1d_{3/2}$ orbitals. The number of particles in either the $2s_{1/2}$ or $1d_{5/2}$ orbitals was required to be even. The Gamow-Teller operator was applied, producing a state called the collective Gamow-Teller state |CGT>:

$$(GT)|g.s.\rangle = |CGT\rangle,$$

where (GT) is the Gamow-Teller operator as defined above but now summed over all particles,

$$(GT) = \Sigma g_A \sigma_i \tau_i^- .$$

In our case the Gamow-Teller operator changed a neutron into a proton, and therefore produced a 5p/7h daughter model space from the 4p/6h parent model space.

Then, using the method of Whitehead,[60-61] i.e., the Lanczos diagonalization algorithm, a set of approximate eigenstates $|e_i\rangle$ of the daughter nucleus ^{26}Al were produced. Each approximate eigenstate had an associated spin, parity, and energy E_i. The manifold of ^{26}Al states generated in this manner is compared with known states in figures 17 and 18. The Gamow-Teller strengths α_i^2 of the 1^+ states are also indicated in figures 17 and 18, where:

$$\alpha_i^2 = \langle e_i | CGT \rangle^2 \langle CGT | CGT \rangle,$$

$\langle CGT | CGT \rangle$ is the total Gamow-Teller strength of ^{26}Al; its shell model calculated value is 7.5.

As stated earlier, Z-coefficients are coefficients of fractional parentage which measure the contribution of each of the possible particle-hole pairs in the

(p,n) reaction. The Z-coefficients for the 1^+ states were determined in the following manner: The approximate eigenstate corresponding to the experimental 1^+ state for which Z-coefficients were desired was identified. This identification was based on finding an approximate 1^+ state of the same T and similar excitation energy as the experimental state. If there were several closely spaced approximate 1^+ states at about the excitation energy of the actual state (as occurred for only the 9.44 and 10.47 MeV experimental states) we chose the state(s) carrying significant Gamow-Teller strength α_i^2 and calculated Z-coefficients for each one. The DWBA code was then used to calculate a set of differential cross sections for each set of Z-coefficients. The differential cross sections for the actual 1^+ state were the incoherent sum of the differential cross sections produced by the different sets of Z-coefficients.

Once the calculated approximate state (or states) corresponding to the known state was determined (see paragraph above), the Z-coefficients were calculated in the following manner: One body operators O_j were created. These O_j were applied to the ground state wave function |g.s.> to change a neutron in a specified orbital into a proton in another specified orbital. The operators acted on |g.s.> to produce a wave function with the spin, isospin, and parity of the final state wave function $|e_i>$. In the case of 0^+ to 1^+ transitions, five possible operators were created. The Z-coefficients were then the set of numbers produced by the complete set of operators $O_j(x)$:

$$Z_j = <e_i|O_j(x)|g.s.>,\ j = 1,5.$$

The squares of the Z-coefficients measured the strengths of the various configurations making up the excited state wave function $|e_i>$.

We now tabulate the $^{26}Mg(p,n)^{26}Al$ Z-coefficients calculated by the Livermore shell model code. "Transitions" identifies the transition of a neutron in the first indicated orbital into a proton in the second indicated orbital. For example,

$d_{3/2} \rightarrow d_{5/2}$ is the transition of a $1d_{3/2}$ neutron into a $1d_{5/2}$ proton. The approximate state of ^{26}Al used to calculate the Z-coefficients is identified by its energy. For example, the approximate state with excitation energy of 1.373 MeV is used to calculate the (experimental) 1.85 MeV 1^+ state Z-coefficients. Note that the first 1^+ approximate state excitation energy in our shell model calculation was normalized to the 1.06 MeV state, i.e., the first experimental 1^+ state. Thus all the T = 0 states in our shell model manifold (figure 17) have been shifted up by 1.06 MeV.

The $^{26}Mg(p,n)^{26}Al$ Z-coefficients are:

1.06 MeV 1^+ Z-coefficients with the 1st 1^+ Approximate State

Transition	Z-coefficient
$d_{5/2} \rightarrow d_{5/2}$	-3.52E-01
$d_{5/2} \rightarrow d_{3/2}$	-1.06E-01
$s_{1/2} \rightarrow s_{1/2}$	-6.27E-03
$d_{3/2} \rightarrow d_{3/2}$	9.92E-02
$d_{3/2} \rightarrow d_{5/2}$	-8.10E-02

1.85 MeV 1^+ Z-coefficients with the 1.373 MeV 1^+ Aproximate State

Transition	Z-coefficient
$d_{5/2} \rightarrow d_{5/2}$	1.28E-01
$d_{5/2} \rightarrow d_{3/2}$	2.04E-01
$s_{1/2} \rightarrow s_{1/2}$	2.84E-02
$d_{3/2} \rightarrow d_{3/2}$	-7.10E-02
$d_{3/2} \rightarrow d_{5/2}$	4.41E-02

9.44 MeV 1^+ Z-coefficients with the 8.521 MeV 1^+ Approximate State (Set 1 of 2)

Transition	Z-coefficient
$d_{5/2} \rightarrow d_{5/2}$	8.29E-02
$d_{5/2} \rightarrow d_{3/2}$	1.81E-01
$s_{1/2} \rightarrow s_{1/2}$	-1.17E-02
$d_{3/2} \rightarrow d_{3/2}$	1.54E-03
$d_{3/2} \rightarrow d_{5/2}$	3.64E-02

9.44 MeV 1^+ Z-coefficients with the 8.755 MeV 1^+ Approximate State (Set 2 of 2)

Transition	Z-coefficient
$d_{5/2} \rightarrow d_{5/2}$	1.55E-02
$d_{5/2} \rightarrow d_{3/2}$	-1.15E-01
$s_{1/2} \rightarrow s_{1/2}$	7.90E-03
$d_{3/2} \rightarrow d_{3/2}$	-8.25E-03
$d_{3/2} \rightarrow d_{5/2}$	-1.50E-02

10.47 MeV 1^+ Z-coefficients with the 10.442 MeV 1^+ Approximate State (Set 1 of 3)

Transition	Z-coefficient
$d_{5/2} \rightarrow d_{5/2}$	-3.72E-02
$d_{5/2} \rightarrow d_{3/2}$	-9.93E-02
$s_{1/2} \rightarrow s_{1/2}$	-6.91E-04
$d_{3/2} \rightarrow d_{3/2}$	-1.65E-02
$d_{3/2} \rightarrow d_{5/2}$	-2.57E-02

10.47 MeV 1^+ Z-coefficients with the 10.664 MeV 1^+ Approximate State (Set 2 of 3)

Transition	Z-coefficient
$d_{5/2} \rightarrow d_{5/2}$	2.46E-02
$d_{5/2} \rightarrow d_{3/2}$	1.79E-01
$s_{1/2} \rightarrow s_{1/2}$	2.57E-03
$d_{3/2} \rightarrow d_{3/2}$	-6.16E-03
$d_{3/2} \rightarrow d_{5/2}$	4.66E-02

10.47 MeV 1^+ Z-coefficients with the 10.703 MeV 1^+ Approximate State (Set 3 of 3)

Transition	Z-coefficient
$d_{5/2} \rightarrow d_{5/2}$	3.10E-02
$d_{5/2} \rightarrow d_{3/2}$	9.92E-02
$s_{1/2} \rightarrow s_{1/2}$	-1.42E-02
$d_{3/2} \rightarrow d_{3/2}$	1.14E-02
$d_{3/2} \rightarrow d_{5/2}$	2.24E-02

3. $^{54}Fe(p,n)^{54}Co$ Calculations

The total shell model calculated Gamow-Teller strength $\langle CGT | CGT \rangle$ for ^{54}Co is 16.3 for the 0p/2h calculation and 15.1 for the 1p/3h calculation (these calculations are described below). The Gamow-Teller strengths α_i^2 for individual 1^+ states are given in figure 19 (as before, $\alpha_i^2 = \langle e_i | CGT \rangle^2 \langle CGT | CGT \rangle$).

Two sets of Z-coefficients were obtained for the $^{54}Fe(p,n)^{54}Co$ 1^+ transitions. The first set used the $[1f_{7/2}, 2p_{3/2}, 2p_{1/2}, 1f_{5/2}]$ orbitals with the 0p/2h model

space of $(1f_{7/2})^{-2}$ $(2p,1f_{5/2})^{0}$ for the ^{54}Fe |g.s.>. The inert core was taken to be ^{48}Ca. The second set of Z-coefficients used the same orbitals and the same core, but had the 1p/3h + the 0p/2h model space yielding the $(1f_{7/2})^{-3}$ $(2p,1f_{5/2})^{+1}$ model space for the ^{54}Fe |g.s.>. The daughter state was 1p/3h for the first set, and 2p/4h + 1p/3h for the second. The ^{54}Fe(p,n)^{54}Co IAS transition was computed in the above 1p/3h excitation restriction only.

The Z-coefficients for the 0.94 MeV 1^+ state were computed in the same manner as those for the 1.06 MeV 1^+ state in ^{26}Al. However, there were ten Z-coefficients for transitions to 1^+ states of ^{54}Co, in contrast to five for those to 1^+ states in ^{26}Al. This increase in the number of Z-coefficients was due to there being twice as many possible $\Delta J = 1$ single-particle transitions (of a neutron into a proton) in the $[1f_{7/2}, 2p_{3/2}, 2p_{1/2}, 1f_{5/2}]$ model space of ^{54}Fe and ^{56}Fe as in the $[1d_{5/2}, 2s_{1/2}, 1d_{3/2}]$ model space of ^{26}Mg.

The set of Z-coefficients for the 0p/2h model space was computed using the calculated approximate ^{54}Co 1^+ state at 5.810 MeV, and the ^{54}Fe ground state. The set of Z-coefficients for the 1p/3h + the 0p/2h model space was computed using the calculated approximate ^{54}Co 1^+ state at 5.482 MeV, and the ^{54}Fe ground state. The Z-coefficients were used to calculate DWBA differential cross sections for a 1^+ state at 5.32 MeV; these were then compared with the experimentally measured differential cross sections of the 5.3 MeV ^{54}Co state (see figure 48). This comparison suggests that the experimental state is not 1^+ (see section IV).

The ^{54}Co IAS Z-coefficients were calculated in the following manner: Since the ^{54}Co IAS wave function $|^{54}$Co IAS> differed from the ^{54}Fe ground state wave function only in isospin projection T_z, we produced the $|^{54}$Co IAS> by application of the T_z- lowering operator T_z^-:

$$T_z^- |^{54}\text{Fe g.s.}\rangle = |^{54}\text{Co IAS}\rangle.$$

The T_z^- operator lowered T_z by one unit, changing the T = 1, T_z = 1 $|^{54}$Fe g.s.> into the T = 1, T_z = 0 $|^{54}$Co IAS>. The Z-coefficients were then given by:

$$Z_j = \langle^{54}\text{Fe g.s. } |O_j(x)|^{54}\text{Co IAS}\rangle, \; j = 1,4.$$

The one body operators $O_j(x)$ change a neutron in a particular orbital into a proton in the same orbital. Since the total spin of the neutron and proton orbitals must couple to zero, only the four Z-coefficients corresponding to the $2p_{1/2}\rightarrow 2p_{1/2}$, $2p_{3/2}\rightarrow 2p_{3/2}$, $1f_{5/2}\rightarrow 1f_{5/2}$, and $1f_{7/2}\rightarrow 1f_{7/2}$ single particle transitions occurred.

The ^{54}Fe(p,n)^{54}Co Z-coefficients are:

0.00 MeV 0^+ Z-coefficients

Transition	Z-coefficient 1p/3h
$p_{1/2}\rightarrow p_{1/2}$	4.98E-03
$p_{3/2}\rightarrow p_{3/2}$	2.34E-02
$f_{5/2}\rightarrow f_{5/2}$	1.65E-02
$f_{7/2}\rightarrow f_{7/2}$	4.65E-01

0.94 MeV 1^+ Z-coefficients with the 0.337 MeV 1^+ Approximate State (0p/2h) and the 0.114 MeV 1^+ Approximate State (1p/3h)

Transition	Z-coefficient 0p/2h	Z-coefficient 1p/3h
$p_{1/2} \rightarrow p_{1/2}$	0.	-2.16E-03
$p_{1/2} \rightarrow p_{3/2}$	0.	-2.38E-03
$p_{3/2} \rightarrow p_{1/2}$	0.	2.26E-03
$p_{3/2} \rightarrow p_{3/2}$	0.	9.13E-03
$p_{3/2} \rightarrow f_{5/2}$	0.	-7.84E-03
$f_{5/2} \rightarrow p_{3/2}$	0.	9.00E-03
$f_{5/2} \rightarrow f_{5/2}$	0.	-1.12E-02
$f_{5/2} \rightarrow f_{7/2}$	0.	1.16E-01
$f_{7/2} \rightarrow f_{5/2}$	1.16E-01	-4.03E-02
$f_{7/2} \rightarrow f_{7/2}$	-4.73E-01	4.44E-01

5.3 MeV 1^+ Z-coefficients with the 5.810 MeV 1^+ Approximate State (0p/2h) and the 5.482 MeV 1^+ Approximate State (1p/3h)

Transition	Z-coefficient 0p/2h	Z-coefficient 1p/3h
$p_{1/2} \rightarrow p_{1/2}$	0.	2.90E-03
$p_{1/2} \rightarrow p_{3/2}$	0.	-7.98E-03
$p_{3/2} \rightarrow p_{1/2}$	0.	5.52E-04
$p_{3/2} \rightarrow p_{3/2}$	0.	4.88E-03
$p_{3/2} \rightarrow f_{5/2}$	0.	-5.66E-03
$f_{5/2} \rightarrow p_{3/2}$	0.	-2.05E-02
$f_{5/2} \rightarrow f_{5/2}$	0.	1.97E-03
$f_{5/2} \rightarrow f_{7/2}$	0.	-5.91E-03
$f_{7/2} \rightarrow f_{5/2}$	-4.28E-01	-1.46E-01
$f_{7/2} \rightarrow f_{7/2}$	-4.89E-02	-1.71E-02

4. $^{56}Fe(p,n)^{56}Co$ Calculations

The total shell model calculated Gamow-Teller strength <CGT | CGT> for ^{56}Co is 22.0. The Gamow-Teller strengths α_i^2 for individual 1^+ states are given in figure 20 (as before, $\alpha_i^2 = \langle e_i | CGT \rangle^2 \langle CGT | CGT \rangle$).

Since we were able to extract cross sections for only two of the known 1^+ states in ^{56}Co, we calculated Z-coefficients for only those states (at 1.7203 and 2.79 MeV). The model space and core were the same as for the $^{54}Fe(p,n)$ above, except that the 2p/2h excitation restriction was placed upon the ^{56}Fe ground state, i.e., $(1f_{7/2})^{-2}\ (2p,1f_{5/2})^{+2}$. This yielded a 3p/3h model space for the ^{56}Co daughter nucleus. The Z-coefficients for both of the 1^+ states were computed in the same way as those for the 0.94 MeV 1^+ in ^{54}Co. The Z-coefficients for the

isobaric analog state in ^{56}Co (3.59 MeV 0^+) were computed in the same way as those for the ^{54}Co IAS; i.e., through the application of the T_z- lowering operator to the T = 2, T_z = 2 $|^{56}$Fe g.s.> to produce the T = 2, T_z = 1 $|^{56}$Co IAS>. The Z-coefficients were then calculated with the same set of operators O_j used in calculating the Z-coefficients for the ^{54}Co IAS.

The ^{56}Fe(p,n)^{56}Co Z-coefficients are:

1.72 MeV 1^+ Z-coefficients with the 1.818 MeV 1^+ Approximate State

Transition	Z-coefficient
$p_{1/2} \rightarrow p_{1/2}$	-6.09E-02
$p_{1/2} \rightarrow p_{3/2}$	-1.62E-01
$p_{3/2} \rightarrow p_{1/2}$	2.28E-01
$p_{3/2} \rightarrow p_{3/2}$	3.29E-01
$p_{3/2} \rightarrow f_{5/2}$	-2.54E-03
$f_{5/2} \rightarrow p_{3/2}$	4.39E-03
$f_{5/2} \rightarrow f_{5/2}$	-2.76E-02
$f_{5/2} \rightarrow f_{7/2}$	-4.33E-03
$f_{7/2} \rightarrow f_{5/2}$	-1.27E-01
$f_{7/2} \rightarrow f_{7/2}$	3.74E-02

2.79 MeV 1^+ Z-coefficients with the 3.244 MeV 1^+ Approximate State

Transition	Z-coefficient
$p_{1/2} \rightarrow p_{1/2}$	-6.23E-02
$p_{1/2} \rightarrow p_{3/2}$	-1.25E-02
$p_{3/2} \rightarrow p_{1/2}$	-6.64E-03
$p_{3/2} \rightarrow p_{3/2}$	5.31E-02
$p_{3/2} \rightarrow f_{5/2}$	-4.36E-02
$f_{5/2} \rightarrow p_{3/2}$	2.37E-02
$f_{5/2} \rightarrow f_{5/2}$	-8.40E-03
$f_{5/2} \rightarrow f_{7/2}$	4.60E-03
$f_{7/2} \rightarrow f_{5/2}$	-1.02E-01
$f_{7/2} \rightarrow f_{7/2}$	3.65E-01

3.59 MeV 0^+ Z-coefficients

Transition	Z-coefficient
$p_{1/2} \rightarrow p_{1/2}$	1.94E-01
$p_{3/2} \rightarrow p_{3/2}$	4.19E-01
$f_{5/2} \rightarrow f_{5/2}$	2.28E-02
$f_{7/2} \rightarrow f_{7/2}$	2.75E-01

C. DWBA Calculations

1. Overview

The code DWBA79 (an updated version of R. Schaeffer and J. Raynal's DWBA70 code[62]) was used to calculate the DWBA differential cross sections of this thesis. These DWBA differential cross sections are plotted as smooth curves superimposed on the experimentally determined differential cross section plots.

Each smooth curve is first drawn through the 37 differential cross sections calculated by DWBA79 (over the center of mass angular range of 0° to 180° in 5° increments). Then, each curve is normalized to the data by the factor n, as described below. The value of n is indicated on each plot by "DWBA calculation (x n)," where n is a real number. The plots are found in section VII; all of the DWBA curves therein have been normalized to the data except for the 5.3 MeV state in ^{54}Co (see figure 48). The number n (except for the ^{56}Co 1.7203 MeV 1^+ state) is

$$n = \frac{\text{exp. } \sigma_{total}}{\text{DWBA } \sigma_{total}},$$

where exp. σ_{total} is the angle-integrated cross section computed by integrating (with the code LEGENDRE) the experimental differential cross sections over angle. DWBA σ_{total} is the angle-integrated cross section calculated by DWBA79. In the case of the ^{56}Co 1.7203 MeV 1^+ state (see figures 49 and 53), exp. σ_{total} was not available, so the values of n were chosen to give a reasonable fit of the DWBA79 curves to the experimental differential cross sections. Note that exp. σ_{total}, DWBA σ_{total}, and n appear on the figures, and in section III.C.7 below.

Although DWBA calculations for the (p,n) reaction to the 0.9372 MeV 1^+ and 5.3 MeV states in ^{54}Co were made with the 0p/2h sets of Z-coefficients, they are not plotted in the figures. Instead, we show only results obtained with the more accurate 1p/3h sets of Z-coefficients. For the 0.9372 MeV 1^+ state (at all three proton bombarding energies) the DWBA calculations with the 0p/2h Z-coefficients were nearly identical in shape, and somewhat higher in magnitude, compared to the calculations made with the 1p/3h Z-coefficients. The shapes were also nearly identical for the 5.3 MeV state, but the 0p/2h calculation was

approximately ten times higher than the 1p/3h calculation. Of course, the calculations for the 5.3 MeV state were made only at the proton bombarding energy of 24.6 MeV, as our lower energy data did not reach sufficiently high in excitation energy to detect the state.

2. Optical Model Potential

The optical model potential for our DWBA calculations is that of F.D. Becchetti, Jr., and G.W. Greenlees:[63]

$$V(r) = V_C(r, R_C) \quad \text{Coulomb}$$

$$-V_R\, f(r, r_R, a_R) \quad \text{central real}$$

$$-iW_V\, f(r, r_I', a_I') \quad \text{imaginary volume}$$

$$+4ia_I W_{Sf}\, (d/dr)\, f(r, r_I, a_I) \quad \text{imaginary surface}$$

$$+\left(\frac{\hbar}{m_\pi c}\right)^2 [V_{SO}(1/r)\, (d/dr)\, f\,(r, r_{SO}, a_{SO})]\, L\cdot\sigma \quad \text{spin-orbit}$$

where $f(r, R, a) = \{1+\exp[(r-RA^{1/3})/a]\}^{-1}$ is in the Woods-Saxon form (A is the mass number). The Coulomb potential is of a uniformly charged sphere of radius R and total charge Ze, where Z is the atomic number. $L\cdot\sigma$ is the scalar product of the particle's spin and orbital angular momentum; $\left(\frac{\hbar}{m_\pi c}\right)$ is the pion's Compton radius. The unit of energy is MeV, and the unit of length is fm.

It should be noted that a better optical model potential may exist. However, the author of this thesis was not aware of any.

The next two sections present the proton-nucleus and neutron-nucleus optical model parameters for the above model. The units of energy are MeV and the units of length are fm, as above.

3. Proton-Nucleus Optical Model Parameters

The proton-nucleus optical model parameters used in the DWBA calculations of this thesis are those of Becchetti and Greenlees:[64]

$R_C = 1.25$

$V_R = 54.0 - 0.32E_p + 0.4Z/A^{1/3} + 24.0(N-Z)/A$

$r_R = 1.17$

$a_R = 0.75$

$W_V = 0.22E_p - 2.7$, or zero, whichever is greater

$W_{Sf} = 11.8 - 0.25E_p + 12.0(N-Z)/A$, or zero, whichever is greater

$r_I' = r_I = 1.32$

$a_I' = a_I = 0.51 + 0.7(N-Z)/A$

$V_{SO} = 6.2$

$r_{SO} = 1.01$

$a_{SO} = 0.75$

Z is the atomic number, N is the neutron number, and A is the mass number. E_p is the bombarding energy of the proton in the lab system.

4. Neutron-Nucleus Optical Model Parameters

The neutron-nucleus optical model parameters of J. Rapaport, V. Kulkarni, and R.W. Finlay[65] are used in the DWBA calculations of this thesis. These parameters were deduced from (n,n) differential cross sections on six nuclei in the energy range of 7-26 MeV, and are more accurate than the earlier Becchetti-Greenlees ones.[66] Here are the neutron-nucleus optical model parameters:

$R_C = 1.25$

$V_R = 54.62 - 0.30E_n - [(N-Z)/A](25.3-0.02E_n)$

$r_R = 1.225 - 2.985/A$

$a_R = 0.668$

$W_V = 0$, for $E_n \lesssim 15$ MeV; $= -3.95 + 0.37E_n$, for $E_n \gtrsim 15$ MeV

$W_{Sf} = 4.27 + 0.40E_n - 12.7[(N-Z)/A]$, for $E_n \lesssim 15$ MeV;
$= 13.5 - 0.35E_n - 9.3[(N-Z)/A]$, for $E_n \gtrsim 15$ MeV

$r_I' = r_I = 1.297$

$a_I' = a_I = 0.59$

$V_{SO} = 6.2$

$r_{SO} = 1.01$

$a_{SO} = 0.75$

Z is the atomic number, N is the neutron number, and A is the mass number. E_n is the energy of the incident neutron.

We used the approximation of $E_n = E_p - E_x + Q$ in our DWBA calculations, where E_p is the proton bombarding energy, E_x is the excitation energy of the residual nuclear state we are considering, and Q is the ground state Q-value for our (p,n) reaction. This approximation is made because the neutron energy is a function of the angle at which it is emitted. To be precise, E_n would have to be calculated at each of the 37 angles between 0° and 180°, and the neutron optical parameters would have to be calculated for each of the 37 neutron energies. This would be tedious, and would not contribute significantly to the overall accuracy of the DWBA calculation. Our simple approximation essentially assumes that the neutron is emitted at zero degrees, and ignores the very small center of mass correction.

5. Effective Nucleon-Nucleon Interaction

The effective nucleon-nucleon interaction used in DWBA79 for all of the DWBA calculations of this thesis is:

$V = V_{Coul}$	Coulomb
$+V_{se}$	central singlet-even
$+V_{te}$	central triplet-even
$+V_{so}$	central singlet-odd
$+V_{to}$	central triplet-odd
$+V_{\ell so}$	spin-orbit odd
$+V_{\ell se}$	spin-orbit even
$+V_{tno}$	tensor-odd
$+V_{tne}$	tensor-even

The above components V_x (except V_{Coul}) are in the form given by G. Bertsch *et al.*:[67]

$V_x = V_{x1}\, Y(r_{12}/R_1) + V_{x2}\, Y(r_{12}/R_2) + V_{x3}\, Y(r_{12}/R_3)$

for $V_x =$ V_{se}, V_{te}, V_{so}, and V_{to} (central potentials);

$V_x = [V_{x1}\, Y(r_{12}/R_1) + V_{x2}\, Y(r_{12}/R_2) + V_{x3}\, Y(r_{12}/R_3)]L \cdot S$

for $V_x =$ $V_{\ell so}$ and $V_{\ell se}$ (spin-orbit potentials);

$V_x = [V_{x1}\, r_{12}^2\, Y(r_{12}/R_1) + V_{x2}\, r_{12}^2\, Y(r_{12}/R_2) + V_{x3}\, r_{12}^2\, Y(r_{12}/R_3)]S_{12}$

for $V_x = V_{tno}$ and V_{tne} (tensor potentials).

$Y(x) = \frac{\exp(-x)}{x}$ is the Yukawa form factor.

$S_{12} = \frac{1}{r^2}\{3(\sigma_1 \cdot r)(\sigma_2 \cdot r) - r^2(\sigma_1 \cdot \sigma_2)\}$ is the tensor operator.

All of the DWBA calculations of this thesis used the set of nucleon-nucleon potentials consisting of $V_{Coul} = V_{to} = 0.$, and the following potentials from a table of best fit interactions in Bertsch *et al.*:[68]

Name	Channel	V_{x1} [MeV]	V_{x2} [MeV]	V_{x3} [Mev]	Quality of Fit
Reid	se	12454.	-3835.	-10.463	good
Reid	te	21227.	-6622.	-10.463	fair
Elliott	so	26941.	-2777.	31.389	fair
Reid	ℓso	-3733.	-427.3	0.	good
Elliott	ℓse	0.	-813.	0.	fair-good
Elliott	tno	0.	283.	13.62	fair-good
Reid	tne	0.	-1259.6	-28.41	good

$R_1 = 0.25$ fm, $R_2 = 0.40$ fm, $R_3 = 1.414$ fm for all channels except the tensor-even (tne) and the tensor-odd (tno). For tne and tno we have $R_1 = 0.25$ fm,

R_2 = 0.40 fm, and R_3 = 0.7 fm. "Name" refers to the interaction derived from the nucleon-nucleon potentials of Reid,[69] or from the oscillator matrix elements of Elliott.[70] "Channel" is the reaction channel; i.e., se refers to the central singlet-even channel. V_{x1}, V_{x2}, V_{x3} refer to the components of V_x in the form of Bertsch *et al.* above; i.e., $V_{se} = V_{se1}\,Y(r_{12}/R_1) + V_{se2}\,Y(r_{12}/R_2) + V_{se3}\,Y(r_{12}/R_3)$. "Quality of Fit" is "poor, fair, or good, depending on how well the matrix elements are fit, and whether there are large cancellations between various terms of the Yukawa potential."[71] The effective interaction of Bertsch *et al.* is commonly referred to as the "G-matrix effective interaction," or as "M3Y."

A commonly used alternative form of the effective nucleon-nucleon potential is presented below:

$V = V_C$	Coulomb
$+ V_o$	central
$+ V_\sigma\,(\sigma_1 \cdot \sigma_2)$	central with spin transfer
$+ V_\tau\,(\tau_1 \cdot \tau_2)$	central with charge transfer
$+ V_{\sigma\tau}\,(\sigma_1 \cdot \sigma_2)\,(\tau_1 \cdot \tau_2)$	central with charge & spin transfer
$+ V_{LS}\,L \cdot S$	spin-orbit
$+ V_{LS\tau}\,(\tau_1 \cdot \tau_2)\,L \cdot S$	spin-orbit with charge transfer
$+ V_T\,S_{12}$	tensor
$+ V_{T\tau}\,(\tau_1 \cdot \tau_2)\,S_{12}$	tensor with charge transfer

The above components V_w (except V_{Coul}) are in the form given by G. Bertsch *et al.*:[72]

$V_w = V_{w1}Y(r_{12}/R_1) + V_{w2}Y(r_{12}/R_2) + V_{w3}Y(r_{12}/R_3)$

for $V_w = V_0$, V_σ, V_τ, and $V_{\sigma\tau}$ (central potentials);

$V_w = [V_{w1}Y(r_{12}/R_1) + V_{w2}Y(r_{12}/R_2) + V_{w3}Y(r_{12}/R_3)]L \cdot S$

for $V_w = V_{LS}$ and $V_{LS\tau}$ (spin-orbit potentials);

V_w = $[V_{w1}\, r_{12}^2\, Y(r_{12}/R_1) + V_{w2}\, r_{12}^2\, Y(r_{12}/R_2) + V_{w3}\, r_{12}^2\, Y(r_{12}/R_3)]S_{12}$

for V_w = $V_{T\tau}$ and $V_{T\tau}$ (tensor potentials).

$Y(x) = \frac{\exp(-x)}{x}$ is the Yukawa form factor.

$S_{12} = \frac{1}{r^2}\{3(\sigma_1 \cdot r)(\sigma_2 \cdot r) - r^2(\sigma_1 \cdot \sigma_2)\}$ is the tensor operator.

The relationship of the two effective nucleon-nucleon interactions is given in Bertsch *et al.*[73] as:

$V_o = \frac{1}{16}[\,3V_{te} + 3V_{se} + 9V_{to} + 1V_{so}]$

$V_\sigma = \frac{1}{16}[\,1V_{te} - 3V_{se} + 3V_{to} - 1V_{so}]$

$V_\tau = \frac{1}{16}[-3V_{te} + 1V_{se} + 3V_{to} - 1V_{so}]$

$V_{\sigma\tau} = \frac{1}{16}[-1V_{te} - 1V_{se} + 1V_{to} + 1V_{so}]$

$V_{LS} = \frac{1}{4}\,[\,3V_{\ell so} + 1V_{\ell se}]$

$V_{LS\tau} = \frac{1}{4}\,[\,1V_{\ell so} - 1V_{\ell se}]$

$V_T = \frac{1}{4}\,[\,3V_{tno} + 1V_{tne}]$

$V_{T\tau} = \frac{1}{4}\,[\,1V_{tno} - 1V_{tne}]$

The above relationship between the two representations allows us to calculate the set (V_o, V_σ, V_τ, ...) from the (V_{se}, V_{te}, V_{to}, ...) used in this thesis:

Interaction	V_{w1} [MeV]	V_{w2} [MeV]	V_{w3} [MeV]
V_o	7999.0	-2134.3	-1.9618
V_σ	-2692.3	478.75	-0.6539
V_τ	-4885.5	1175.5	-0.6539
$V_{\sigma\tau}$	-421.25	480.00	3.2697
V_{LS}	-2800.	-523.7	0.
$V_{LS\tau}$	-933.3	96.43	0.
V_T	0.	-103.	3.113
$V_{T\tau}$	0.	386.	10.51

As before, V_C = 0. R_1 = 0.25 fm, R_2 = 0.40 fm, R_3 = 1.414 fm for all interactions except V_T and $V_{T\tau}$. For V_T and $V_{T\tau}$ we have R_1 = 0.25 fm, R_2 = 0.40 fm, and R_3 = 0.7 fm.

6. Shell Model Wave Functions

The shell model wave functions used in all of the DWBA calculations of this thesis are harmonic oscillator wave functions characteristic of the quantum numbers n, j, and l. The valence shell model orbitals for the various calculations are given in section III.B above. Only the valence shell model wave functions are used in the DWBA calculations since the core is inert.

7. Tabulation of exp. σ_{total}, DWBA σ_{total}, and n

Here is a tabulation of the values of exp. σ_{total}, DWBA σ_{total}, and n for all of our states (N/A indicates that a value is not

available). Complete definitions of exp. σ_{total}, DWBA σ_{total}, and n were given in section III.C.1 above. As previously defined, $n = \frac{\text{exp. } \sigma_{total}}{\text{DWBA } \sigma_{total}}$, for all the states below except the 1.7203 MeV 1^+ in ^{56}Co; for that state n is the constant multiplying the DWBA differential cross sections in order to fit them to the measurements. This was done because the code LEGENDRE was unable to compute exp. σ_{total} for that state.

$^{26}Mg(p,n)^{26}Al$, E_p = 19.12 MeV

^{26}Al State	exp. σ_{total} [mb]	DWBA σ_{total} [mb]	n
1.0578 MeV 1^+	3.58±0.27	3.27	1.09
1.851 MeV 1^+	1.74±0.13	2.36	0.74
3.1596 MeV 2^+	2.99±0.22	N/A	N/A

$^{26}Mg(p,n)^{26}Al$, E_p = 24.97 MeV

^{26}Al State	exp. σ_{total} [mb]	DWBA σ_{total} [mb]	n
1.0578 MeV 1^+	2.04±0.17	3.28	0.62
3.1596 MeV 2^+	0.84±0.07	N/A	N/A
9.44 MeV 1^+;T=1	0.96±0.07	0.84	1.15
10.47 MeV 1^+;T=1	0.56±0.05	0.73	0.77

$^{54}Fe(p,n)^{54}Co$, E_p = 17.20 MeV

^{54}Co State	exp. σ_{total} [mb]	DWBA σ_{total} [mb]	n
0.00 MeV 0^+	4.50±0.73	1.74 (1p/3h)	2.59
0.199 MeV 7^+	1.59±0.12	N/A	N/A
0.9372 MeV 1^+	1.70±0.13	1.53 (0p/2h)	1.11
0.9372 MeV 1^+	1.70±0.13	1.13 (1p/3h)	1.50

$^{54}Fe(p,n)^{54}Co$, E_p = 18.60 MeV

^{54}Co State	exp. σ_{total} [mb]	DWBA σ_{total} [mb]	n
0.00 MeV 0^+	4.19±0.31	1.67 (1p/3h)	2.51
0.199 MeV 7^+	1.82±0.14	N/A	N/A
0.9372 MeV 1^+	1.56±0.12	1.55 (0p/2h)	1.00
0.9372 MeV 1^+	1.56±0.12	1.16 (1p/3h)	1.35

$^{54}Fe(p,n)^{54}Co$, E_p = 24.60 MeV

^{54}Co State	exp. σ_{total} [mb]	DWBA σ_{total} [mb]	n
0.00 MeV 0^+	1.87±0.14	1.32 (1p/3h)	1.41
0.199 MeV 7^+	1.36±0.10	N/A	N/A
0.9372 MeV 1^+	0.92±0.069	1.42 (0p/2h)	0.65
0.9372 MeV 1^+	0.92±0.069	1.07 (1p/3h)	0.86
1.4465 MeV 2^+	0.47±0.036	N/A	N/A
5.3 MeV	0.98±0.074	3.22 (0p/2h)	0.30
5.3 MeV	0.98±0.074	0.31 (1p/3h)	3.17

$^{56}Fe(p,n)^{56}Co$, E_p = 19.11 MeV

^{56}Co State	exp. σ_{total} [mb]	DWBA σ_{total} [mb]	n
1.7203 MeV 1^+	N/A	4.06	0.12
2.79 MeV 1^+	1.18±0.089	1.35	0.88
3.59 MeV 0^+	5.89±0.44	3.79	1.56
4.44 MeV 2^+	2.10±0.16	N/A	N/A

$^{56}Fe(p,n)^{56}Co$, E_p = 24.59 MeV

^{56}Co State	exp. σ_{total} [mb]	DWBA σ_{total} [mb]	n
1.7203 MeV 1^+	N/A	3.08	0.10
2.79 MeV 1^+	0.78±0.059	1.19	0.66
3.59 MeV 0^+	4.00±0.30	2.75	1.45
4.44 MeV 2^+	0.75±0.057	N/A	N/A

8. Renormalization of V_τ and $V_{\sigma\tau}$

The normalization factors for V_τ and $V_{\sigma\tau}$ are obtained from the normalization n in the following manner: The experimental differential cross sections are related to the theoretical DWBA cross sections by this equation:

$$\frac{d\sigma}{d\Omega}_{exp.} = (N^f)^2 \cdot (N^w)^2 \frac{d\sigma}{d\Omega}_{DWBA},$$

where $(N^f)^2$ is the normalization of the force, and $(N^w)^2$ is the normalization of the wave function. Integrating both sides of the equation over angle gives:

$$exp.\ \sigma_{total} = (N^f)^2 \cdot (N^w)^2\ DWBA\ \sigma_{total},$$

Thus, $n = (N^f)^2 \cdot (N^w)^2$.

Since the normalization of the wave function $(N^w)^2 = 1$ for the isobaric analog transitions, the normalization of the force is $(N^f)^2 = n$. Isobaric analog transitions are mediated by V_τ, therefore, the normalization N_τ^f of V_τ is just $\sqrt{n}$ (the square root appears because $\frac{d\sigma}{d\Omega}$ is proportional to V_τ^2).

Here is a tabulation of the values of N_τ^f (we have also included exp. σ_{total}, DWBA σ_{total}, and n for reference):

IAS Transition	E_p [MeV]	exp. σ_{total} [mb]	DWBA σ_{total} [mb]	n	N_τ^f
$^{54}Fe(p,n)^{54}Co$	17.20	4.50±0.73	1.74	2.59	1.61
$^{54}Fe(p,n)^{54}Co$	18.60	4.19±0.31	1.67	2.51	1.58
$^{54}Fe(p,n)^{54}Co$	24.60	1.87±0.14	1.32	1.41	1.19
$^{56}Fe(p,n)^{56}Co$	19.11	5.89±0.44	3.79	1.56	1.25
$^{56}Fe(p,n)^{56}Co$	24.59	4.00±0.30	2.75	1.45	1.20

Note that the values of N_τ^f for the $^{54}Fe(p,n)^{54}Co$ IAS transition are considerably larger at E_p = 17.20 and 18.60 MeV than at E_p = 24.60 MeV. Also, the value of N_τ^f for the $^{54}Fe(p,n)^{54}Co$ IAS transition at E_p = 24.60 MeV is

very close to the values for the $^{56}Fe(p,n)^{56}Co$ IAS transition at 19.11 and 24.59 MeV. Examination of the values of exp. σ_{total} and DWBA σ_{total} indicates that the values of exp. σ_{total} for the $^{54}Fe(p,n)^{54}Co$ IAS transition at E_p = 17.20 and 18.60 MeV are about twice the value that would be consistent with the other exp. σ_{total}'s (i.e., we would expect exp. σ_{total} at 17.20 and 18.60 MeV to be approximately 2.5 mb).

The cause of this anomaly in the two lower energy ^{54}Co IAS angle-integrated cross sections is not known. However, we can speculate as follows: The lower proton bombarding energies favor the formation of a compound nucleus. In the case of $^{54}Fe(p,n)^{54}Co$, the ^{55}Co compound nucleus can de-excite to ^{54}Co by neutron emission. The level density around the ^{54}Co IAS is small (only the 0.199 MeV 7^+ state is nearby). Also, the IAS is the 0^+ ground state of ^{54}Co. This means that the energy difference between the compound nucleus excited state and the IAS is greater than that between the compound nucleus excited state and any other state of ^{54}Co. In addition, the spin of the IAS is zero, which eliminates the neutron angular momentum barrier. The low level density, the large energy difference, and the absence of an angular momentum barrier cause the IAS to be preferentially populated by the compound nucleus reaction, thus increasing the magnitude of the angle-integrated cross section.

The anomaly is not seen in the $^{56}Fe(p,n)^{56}Co$ IAS transition at 19.11 MeV for several reasons. First, the level density around the IAS is large, so other levels can be populated. Second, there are levels below the IAS that can be populated. The energy difference between the excited compound nucleus state and levels below the IAS is greater than the energy difference between the excited compound nucleus state and the IAS. This greater energy difference increases the probability of populating energy levels below the IAS.

It must be stressed that, at this time, the above explanation of the large ^{54}Co IAS angle-integrated cross sections at low energies is qualitative, and must remain so until such time that quantitative Hauser-Feshbach calculations can be performed. Because of the likelihood of contamination from compound processes, the lower energy N_τ^f's for the ^{54}Fe(p,n)^{54}Co IAS will not be used.

The average of N_τ^f for the ^{54}Fe(p,n)^{54}Co IAS at 24.60 MeV and the ^{56}Fe(p,n)^{56}Co IAS at 24.59 MeV is 1.195. Assuming an error of 10% (based on the error of approximately 7.5% in the LEGENDRE computed exp. σ_{total}), we have:

$$N_\tau^f = 1.20 \pm 0.12 \text{ at } 24.6 \text{ MeV}$$

$$N_\tau^f = 1.25 \pm 0.12 \text{ at } 19.11 \text{ MeV},$$

where the value at 19.11 MeV is the ^{56}Fe(p,n)^{56}Co IAS result.

Since the spin-flip (p,n) reaction is mediated by $V_{\sigma\tau}$, we use the 0^+ to 1^+ transitions to determine the normalization $N_{\sigma\tau}^f$ of $V_{\sigma\tau}$. The relationship of exp. σ_{total} to DWBA σ_{total} is given by

$$\text{exp. } \sigma_{total} = (N_{\sigma\tau}^f)^2 \cdot (N_{\sigma\tau}^w)^2 \text{ DWBA } \sigma_{total},$$

where $(N_{\sigma\tau}^f)^2$ is the normalization due to the force, and $(N_{\sigma\tau}^w)^2$ is that due to the Gamow-Teller strength. $(N_{\sigma\tau}^w)^2$ is not equal to 1, as in the isobaric analog transitions. Our low energy measurements do not permit us to extract the Gamow-Teller strength. However, the Gamow-Teller strengths of selected states have been extracted through high energy (p,n) measurements on ^{54}Fe and ^{56}Fe targets.[74] Also Gamow-Teller matrix elements have been determined from the beta decay rates of ^{26}Si to the 1.0578 MeV 1^+ and the 1.851 MeV 1^+ levels of the ^{26}Al nucleus.[75]

$(N_{\sigma\tau}^w)^2$ is then just:

$$(N_{\sigma\tau}^w)^2 = \frac{B(GT)_{exp.}}{B(GT)_{calc.}} \text{ [for } ^{54,\,56}\text{Fe(p,n)], and}$$

$$(N^{w}_{\sigma\tau})^2 = \frac{M^2_{exp.}}{B(GT)_{calc.}} \quad [\text{for } ^{26}\text{Mg(p,n)}]$$

where for a selected state, $B(GT)_{exp.}$ is the measured GT strength, $M^2_{exp.}$ is the square of the Gamow-Teller matrix element from the beta decay rate of ^{26}Si, and $B(GT)_{calc.}$ is our shell model calculated GT strength. $B(GT)_{calc.}$ is the α^2 that appears in figures 17-20 (see section III.B above). Since $n = (N^{f}_{\sigma\tau})^2 \cdot (N^{w}_{\sigma\tau})^2$, the normalization $N^{f}_{\sigma\tau}$ of $V_{\sigma\tau}$ is:

$$N^{f}_{\sigma\tau} = \frac{\sqrt{n}}{N^{w}_{\sigma\tau}} .$$

We can now tabulate $N^{f}_{\sigma\tau}$:

E_p [MeV]	Final State	n	$M^2_{exp.}$	$B(GT)_{calc.}$	$N^{f}_{\sigma\tau}$
19.12	^{26}Al 1.0578 MeV 1^+	1.09	1.21±0.05	1.61	1.20
19.12	^{26}Al 1.851 MeV 1^+	0.74	0.64±0.04	1.09	1.12
24.97	^{26}Al 1.0578 MeV 1^+	0.62	1.21±0.05	1.61	0.91
24.97	^{26}Al 9.44 MeV 1^+;T=1	1.15	N/A	0.49	N/A
24.97	^{26}Al 10.47 MeV 1^+;T=1	0.77	N/A	0.42	N/A

E_p [MeV]	Final State	n	$B(GT)_{exp.}$	$B(GT)_{calc.}$	$N^{f}_{\sigma\tau}$
17.20	^{54}Co 0.9372 MeV 1^+	1.50	0.73	0.82	1.30
18.60	^{54}Co 0.9372 MeV 1^+	1.35	0.73	0.82	1.23
24.60	^{54}Co 0.9372 MeV 1^+	0.86	0.73	0.82	0.93
19.11	^{56}Co 1.7203 MeV 1^+	0.12	0.23	2.32	1.10
19.11	^{56}Co 2.79 MeV 1^+	0.88	0.75	0.99	1.08
24.59	^{56}Co 1.7203 MeV 1^+	0.10	0.23	2.32	1.00
24.59	^{56}Co 2.79 MeV 1^+	0.66	0.75	0.99	0.93

N/A means that a value is not available. The treatment in the above table of the 0.9372 MeV 1^+ ^{54}Co state utilized DWBA calculations with 1p/3h Z-coefficients.

From the ^{54}Co 0.9372 MeV 1^+ state above,

$N^f_{\sigma\tau}$ = 1.30 ± 0.13, E_p = 17.20 MeV,

$N^f_{\sigma\tau}$ = 1.23 ± 0.12, E_p = 18.60 MeV.

The average of $N^f_{\sigma\tau}$ at E_p = 19.1 over the ^{26}Al 1.0578 MeV 1^+, the ^{26}Al 1.851 MeV 1^+, the ^{56}Co 1.7203 MeV 1^+, and the ^{56}Co 2.79 MeV 1^+ is:

$N^f_{\sigma\tau}$ = [illegible] ± 0.11, E_p = 19.1 MeV.

The average of $N^f_{\sigma\tau}$ at E_p = 24.6 MeV over the ^{54}Co 0.9372 MeV 1^+, the ^{56}Co 1.7203 MeV 1^+, and the ^{56}Co 2.79 MeV 1^+ is:

$N^f_{\sigma\tau}$ = 0.97 ± 0.10, E_p = 24.6 MeV.

$N^f_{\sigma\tau}$ for the 1.0578 MeV 1^+state of ^{26}Al at 24.97 MeV is:

$N^f_{\sigma\tau}$ = 0.91 ± 0.09, E_p = 24.97 MeV.

The error in all of the above $N^f_{\sigma\tau}$ was chosen to be 10%, since the error in the LEGENDRE determined exp. σ_{total}'s was approximately 7.5%.

The above value of $N^f_{\sigma\tau}$ for the ^{26}Al 1.0578 MeV 1^+ state allows us to correct $B(GT)_{calc.}$ for the 9.44 and 10.47 MeV 1^+ states of ^{26}Al to account for the inadequacies of the wave functions. The normalization factor $(N^w_{\sigma\tau})^2$ is simply $(N^w_{\sigma\tau})^2 = \frac{n}{(N^f_{\sigma\tau})^2}$, where we assume that the value of $N^f_{\sigma\tau}$ for the two states we are considering is the same as the value we derived from the 1.0578 MeV 1^+ state above; namely, $N^f_{\sigma\tau}$ = 0.91. Our normalization factors

are then $(N^{w}_{\sigma\tau})^2$ = 1.39 for the 9.44 MeV state, and $(N^{w}_{\sigma\tau})^2$ = 0.93 for the 10.47 MeV state. Multiplying our $B(GT)_{calc.}$ by $(N^{w}_{\sigma\tau})^2$ yields $B(GT)_{exp.}$ = 0.68 for the 9.44 MeV state, and $B(GT)_{exp.}$ = 0.39 for the 10.47 MeV state. Of course, $B(GT)_{exp.}$ is the experimentally measured Gamow-Teller strength. It must be noted that at the low energy of 24.97 MeV, we are not sure that all of the (p,n) strength is due to Gamow-Teller strength. Also, our $B(GT)_{calc.}$ is dependent on the limitations of the truncated model space.

Let us summarize the N^{f}_{τ} and $N^{f}_{\sigma\tau}$ needed to renormalize V_{τ} and $V_{\sigma\tau}$, and present the renormalized V_{τ} and $V_{\sigma\tau}$ (the values of V_{τ} and $V_{\sigma\tau}$ of the Bertsch *et al.*, effective interaction are V^{B}_{τ} = 17.80 MeV, and $V^{B}_{\sigma\tau}$ = 12.64 MeV, as derived below):

E_p [MeV]	N^{f}_{τ}	$N^{f}_{\sigma\tau}$	$V_{\tau} = N^{f}_{\tau}V^{B}_{\tau}$ [MeV]	$V_{\sigma\tau} = N^{f}_{\sigma\tau}V^{B}_{\sigma\tau}$ [MeV]
17.20	N/A	1.30±0.13	N/A	16.4±1.6
18.60	N/A	1.23±0.12	N/A	15.5±1.6
19.1	1.25±0.12	1.13±0.11	22.3±2.2	14.3±1.4
24.6	1.20±0.12	0.97±0.10	21.4±2.1	12.3±1.2
24.97	N/A	0.91±0.09	N/A	11.5±1.2

From section III.C.5 above, the effective interaction of Bertsch *et al.* has:

$$V_{\tau} = \frac{1}{16}[-3V_{te} + 1V_{se} + 3V_{to} - 1V_{so}]$$

$$V_{\sigma\tau} = \frac{1}{16}[-1V_{te} - 1V_{se} + 1V_{to} + 1V_{so}]$$

with the interactions in the form

$$V_x = \sum_{i=1}^{3} V_{xi}\, Y(r_{12}/R_i)$$

where R_1 = 0.25 fm, R_2 = 0.40 fm, and R_3 = 1.414 fm; the V_{xi}'s are in MeV.

We can determine a one-parameter Yukawa potential $V_\tau^B\, Y(r_{12}/R)$, with $Y(x) = \exp(-x)/x$, and $R = 1$ fm, whose volume integral J_0 equals that of V_τ of Bertsch *et al.* V_τ^B can then be renormalized and compared to the V_τ's determined experimentally by others for one-parameter Yukawa potentials.

J_0 is defined as:

$$J_0 = 4\pi\int_0^\infty V(r_{12}) r_{12}^2\, dr_{12}.$$

For our one-parameter Yukawa potential with $R = 1$ fm,

$$J_0 = 4\pi\int_0^\infty V_\tau^B\, Y(r_{12}/R) r_{12}^2\, dr_{12} = 4\pi V_\tau^B \int_0^\infty [\exp(-r_{12}/R)/r_{12}] r_{12}^2\, R\, dr_{12} =$$

$$4\pi R V_\tau^B \int_0^\infty r_{12} \exp(-r_{12}/R)\, dr_{12} = 4\pi V_\tau^B R^3 = 4\pi V_\tau^B \text{ MeV-fm}^3.$$

The volume integral J_0 for V_τ of Bertsch *et al.*, is:

$$J_0 = 4\pi\int_0^\infty 1/16[-3V_{te} + 1V_{se} + 3V_{to} - 1V_{so}] r_{12}^2\, dr_{12} =$$

$$(4\pi)1/16[-3\int_0^\infty V_{te} r_{12}^2\, dr_{12} + 1\int_0^\infty V_{se} r_{12}^2\, dr_{12} + 3\int_0^\infty V_{to} r_{12}^2\, dr_{12} - 1\int_0^\infty V_{so} r_{12}^2\, dr_{12}]$$

$$= 1/16[-3\int_0^\infty (4\pi) V_{te} r_{12}^2\, dr_{12} + 1\int_0^\infty (4\pi) V_{se} r_{12}^2\, dr_{12}]$$

(as J_0 does not occur in calculating matrix elements for central-odd components).

The volume integrals are evaluated in Bertsch *et al.*,[76] and yield:

$$J_0 = 1/16[-3(-1530) + 1(-1011)] = 223.7 \text{ MeV-fm}^3.$$

Equating J_0 of our one-parameter Yukawa potential to the above J_0 gives:

$$4\pi V_\tau^B = 223.7 \text{ MeV-fm}^3.$$

Hence, V_τ^B = 17.80 MeV.

Using the same procedure to determine $V_{\sigma\tau}^B$ gives:

$$4\pi V_{\sigma\tau}^B = 1/16[-1\int_0^\infty (4\pi)V_{te} r_{12}^2 \, dr_{12} - 1\int_0^\infty (4\pi)V_{se} r_{12}^2 \, dr_{12}]$$

$$4\pi V_{\sigma\tau}^B = 1/16[-1(-1530) - 1(-1011)] = 158.8 \text{ MeV-fm}^3.$$

Hence, $V_{\sigma\tau}^B$ = 12.64 MeV.

Let us now compare our renormalized values of V_τ and $V_{\sigma\tau}$ with the previous experimentally measured values of Austin's survey,[77] Doering *et al.*,[78] Bentley,[79] and Sterrenburg *et al.*[80] Of course, our renormalized values are $V_\tau = 17.80 \cdot N_\tau^f$ MeV, and $V_{\sigma\tau} = 12.64 \cdot N_{\sigma\tau}^f$ MeV, where we use the N_τ^f and $N_{\sigma\tau}^f$ as derived above for specific reactions and energies.

Reaction	Thesis V_τ (E_p=24.6 MeV) [MeV]	Austin V_τ (E_p=25.0 MeV) [MeV]	Bentley V_τ (E_p=22.8 MeV) [MeV]	Sterrenburg V_τ (E_p=24.6 MeV) [MeV]	Doering V_τ (E_p=25.0 MeV) [MeV]
^{26}Mg(p,n)^{26}Al IAS			26.2	17.9	
^{54}Fe(p,n)^{54}Co IAS	21.2		20.4		
^{56}Fe(p,n)^{56}Co IAS	21.4		17.5		
AUSTIN		16.1			
DOERING					17.0
^{48}Ca(p,n)^{48}Sc					18.3

AUSTIN refers to the value of V_τ at 25 MeV recommended by Austin based on a survey of a number of nuclei. DOERING refers to Doering's average value

of V_τ at 25 MeV based on the ^{48}Ca, ^{90}Zr, ^{120}Sn and ^{208}Pb (p,n) transitions to isobaric analog states in the residual nuclei.

Reaction	Thesis $V_{\sigma\tau}$ (E_p=24.6 MeV) [Mev]	Austin $V_{\sigma\tau}$ (E_p=24.8 MeV) [MeV]	Bentley $V_{\sigma\tau}$ (E_p=22.8 MeV) [MeV]	Sterrenburg $V_{\sigma\tau}$ (E_p=24.6 MeV) [MeV]
$^{26}Mg(p,n)^{26}Al$ 1.06 MeV 1^+	11.5[a]		5.2	13.4
$^{26}Mg(p,n)^{28}Al$ 1.85 MeV 1^+				11.5
$^{54}Fe(p,n)^{54}Co$ 0.94 MeV 1^+	12.4		4.8	
$^{56}Fe(p,n)^{56}Co$ 1.72 MeV 1^+	12.6			
$^{56}Fe(p,n)^{56}Co$ 2.79 MeV 1^+	11.6			
$^{7}Li(p,n)^{7}Be$		10.8		

[a] E_p = 24.97 MeV for the $^{26}Mg(p,n)^{26}Al$ 1.06 MeV $V_{\sigma\tau}$ above.

As described in Austin's article, the $^{7}Li(p,n)^{7}Be$ $V_{\sigma\tau}$ was obtained by use of the ratio at E_p = 24.8 MeV of the $^{7}Li(p,n)^{7}Be$ g.s. $\frac{3^-}{2}$ total cross section to the $^{7}Li(p,n)^{7}Be$ 0.431 MeV $\frac{1^-}{2}$ state total cross section. $V_{\sigma\tau}$ was taken as 15.9 MeV. Austin's best estimate of $V_{\sigma\tau}$ based on a number of nuclei is also $V_{\sigma\tau}$ = 10.8 MeV.

We note that the experimental data of this thesis at E_p = 25.0 MeV was used above, and the lower energy data was not used. This was done because compound nucleus effects are negligible at the higher energy, but may be significant at the lower energies.

IV. CONCLUSIONS

No new energy levels in any of the residual nuclei have been identified in this thesis. It appears that the spin and parity assignment of 1^+ by Orihara *et al.* to the 5.3 MeV state of ^{54}Co was incorrect. This conclusion is based on the large discrepancy in shape and magnitude between measured and calculated differential cross sections. Also, this conclusion is consistent with the work of Rapaport *et al.*, which failed to detect significant 1^+ strength at 5.3 MeV using the (p,n) reaction at 160 MeV proton bombarding energy.

The effective interaction of Bertsch *et al.* (with $V_{to} = 0$) in DWBA79 gave good agreement in the shapes of the measured and calculated differential cross sections, but required renormalization of V_τ and $V_{\sigma\tau}$ in order to fit the calculated angle-integrated cross sections to the measurements. The renormalized V_τ was in reasonable agreement with values reported in the literature. The renormalized $V_{\sigma\tau}$ was in very good agreement with values reported in the literature.

The shell model wave functions generated Gamow-Teller strength that was 1.1 to 1.7 times greater (except for the 1.7203 MeV 1^+ state of ^{56}Co) than the Gamow-Teller strength from previous beta decay and high energy (p,n) measurements. The Gamow-Teller strength generated by the shell model wave functions for the ^{56}Co 1.7203 MeV 1^+ state was 10 times the (p,n) measured Gamow-Teller strength at E_p = 160 MeV. This large difference shows that the shell model wave function for that state is inadequate. The factors of 1.1 to 1.7 indicate that the Gamow-Teller strength is quenched in the high energy (p,n) and beta decay measurements. The shell model wave functions are reasonably accurate for the other states calculated in this thesis.

We were able to extract experimental Gamow-Teller strength for the 9.44 and 10.47 MeV 1^+; T = 1 states of ^{26}Al. We demonstrated that the measured Gamow-Teller strength of the 9.44 MeV state is enhanced (by a factor of 1.39) compared to the theoretically predicted value. Also, the measured Gamow-Teller strength of the 10.47 MeV state is quenched (by a factor of 0.93) compared to the theoretically predicted strength.

Our work used large shell model calculations to determine accurate wave functions. These wave functions were then used by the code DWBA79 to precisely calculate differential cross sections. Previous DWBA calculations lacked accurately determined wave functions. For example, Bentley's work lacked both sophisticated wave functions, and the effective nucleon-nucleon interaction of Bertsch *et al.*

Additional measurements on a variety of nuclei at around 25 MeV, and the comparison of the differential cross sections with DWBA calculations using shell model wave functions should be made. Comparison with DWBA calculations can yield further information on the V_τ and $V_{\sigma\tau}$ components of the effective nucleon-nucleon interaction.

V. ACKNOWLEDGMENTS

I wish to thank my parents, Mr. and Mrs. Herman Aron, for their support and encouragement throughout my years of graduate study. I also am indebted to my late aunt, Miss Mary Black, for her help. My cousin, Dr. J.R. Greenberg, encouraged my interest in science early in life. My aunt and uncle, Mr. and Mrs. Roy Cohn, and their son, Dr. Daniel R. Cohn, gave me much useful advice over the years.

The staff at LLNL provided me with much assistance. I owe a great deal to Dr. Calvin Wong who unselfishly devoted hundreds of hours of his time in helping me in every aspect of this thesis. He assisted me in the course of the experimental runs and he patiently explained physics to me. Dr. Stewart D. Bloom was a good adviser and aided me in the theoretical aspects of my thesis. Dr. Robert C. Haight scrutinized my data carefully and graciously read some of my thesis, offering helpful criticism. Mr. Bertram A. Pohl helped me set up and understand the experimental equipment. Mr. Nicholas Sklueff, Mr. Henry Fong, Mr. Donald Rawles, Dr. Ivan D. Proctor, and Mr. James Hanson scrupulously ran the Cyclograaff. Dr. Luisa F. Hansen and Dr. Haight assisted me in the D-D and D-T experimental runs. Mechanical technicians Mr. Jack Garibaldi, Mr. Robert Keville, and Mr. Warren Bell, and electronics technicians Mr. Philip D'Antonio, Mr. Ronald Del Vasto, Mr. Douglas Norman, and Mr. Donald Burns, provided great help in the experimental runs.

Dr. Fred Petrovich and Dr. Steven M. Grimes, both consultants at the lab, devoted a good deal of their valuable time to answering my questions, and helping me understand nuclear physics.

I wish to thank Dr. Carl H. Poppe, Dr. F. Paul Brady, and Dr. Stewart Bloom for reading and approving this thesis. Finally, I want to thank Dr. Abraham Goldberg, Dr. Fred O. Wooten, and Mrs. Kathryn H. Smith of the Department of Applied Science at Livermore, for their good advice and kind assistance.

VI. REFERENCES

1. J.D. Anderson and C. Wong, "Evidence for Charge Independence in Medium Weight Nuclei," *Phys. Rev. Lett.* **7**, 250 (1961).

2. J. Rapaport *et al.*, "Excitation of Giant Spin-Isopin Multipole Vibrations in ^{54,56}Fe and ^{58,60}Ni," *Nucl. Phys.* **A410**, 371 (1983).

3. C.D. Goodman *et al.*, "Gamow-Teller Matrix Elements from 0°(p,n) Cross Sections," *Phys. Rev. Lett.* **44**, 1755 (1980).

4. S.D. Bloom, "Gamow-Teller Strength Functions with the Lanczos Algorithm," in *Progress in Particle and Nuclear Physics, Vol. 11*, ed. Sir Denys Wilkinson (New York: Pergamon Press, 1984), pp. 505-528.

5. R. Madey *et al.*, "^{26}Mg(p,n)^{26}Al, the Total Gamow-Teller Strength from ^{26}Mg, and its Fractionation into the $T_f = T_i - 1$, T_i, and $T_i + 1$ Isospin Channels," *Reprint of Unknown Origin.*

6. J.D. Anderson *et al.*, "Quasielastic (*p,n*) Angular Distributions," *Phys. Rev.* **136**, B118 (1964).

7. J.D. Anderson, C. Wong, and J.W. McClure, "Direct (*p,n*) Reaction in Medium *A* Nuclei: A Configuration-Selective Process," *Phys. Rev.* **129**, 2718 (1963).

8. *Ibid.*, p. 2718.

9. R.F. Bentley *et al.*, "New (*p,n*) Reaction Studies at *Ep* = 23 MeV," *Phys. Rev. Lett.* **27**, 1081 (1971).

10. R.F. Bentley, "A Fast Neutron Spectrometer, (p,n) Reaction Studies, and Microscopic Analyses," Ph.D. Thesis, University of Colorado 1972.

11. *Ibid.*, p. 57.

12. J.D. Carlson, C.D. Zafiratos, and D.A. Lind, "Optical Model Analysis of Quasielastic (p,n) Reactions at 22.8 MeV," *Nucl. Phys.* **A249**, 29 (1975).

13. *Ibid.*, p. 30.

14. *Ibid.*, p. 29.

15. H.W. Fielding *et al.*, "Study of the Reaction $^{56}Fe(p,n)^{56}Co$ to the Antianalog State," *Phys. Rev. Lett.* 33, 226 (1974).

16. H. Orihara *et al.*, "Observation of $T = 1$ and $T = 0$ Gamow-Teller States in the Reaction $^{54}Fe(p,n)^{54}Co$," *Phys. Rev. Lett.* 47, 301 (1981).

17. *Ibid.*, p. 303.

18. J. Rapaport *et al.*, "Excitation of Giant Spin-Isospin Multipole Vibrations in $^{54,56}Fe$ and $^{58,60}Ni$," pp. 371-398.

19. *Ibid.*, p. 396.

20. C.D. Goodman *et al.*, "Gamow-Teller Matrix Elements from 0°(p,n) Cross Sections," pp. 1755-1759.

21. *Ibid.*, p. 1755.

22. S.D. Bloom *et al.*, "Gamow-Teller Strength Function for $^{26}Mg \rightarrow ^{26}Al$," *Phys. Lett.* 107B, 336 (1981).

23. F. Petrovich *et al.*, "Finite-Nucleus *G* Matrix in the Microscopic Description of Inelastic Proton Scattering," *Phys. Rev. Lett.* 22, 895 (1969).

24. S.D. Bloom *et al.*, "Gamow-Teller Strength Function for $^{26}Mg \rightarrow ^{26}Al$," p. 336.

25. S.D. Bloom, "Gamow-Teller Strength Functions with the Lanczos Algorithm," pp. 505-528.

26. *Ibid.*, p. 505. The quote appearing in this thesis has been somewhat changed from the original on the advice of its author, S. D. Bloom. The exact quote is: "in general the agreement between the experimental and theoretical shapes ranges from good to excellent but the theoretical total strengths are too large by a factor of .45 to .55, the so-called GT quenching factor."

27. W. A. Sterrenburg *et al.*, "The $^{26}Mg(p,n)^{26}Al$ Reaction and the Energy Dependence of the Spin-Isospin Effective Interaction," *Phys. Lett.* **91B**, 337 (1980).

28. U.E.P. Berg *et al.*, "Comparison of $^{24,25,26}Mg(p,n)^{24,25,26}Al$ Cross Sections with Giant *M*1 Strength," *Phys. Rev. Lett.* **45**, 11 (1980).

29. R. Madey *et al.*, "$^{26}Mg(p,n)^{26}Al$, the Total Gamow-Teller Strength from ^{26}Mg, and its Fractionation into the $T_f = T_i - 1$, T_i, and $T_i + 1$ Isospin Channels," pp. 41-45.

30. B.H. Wildenthal, "A Universal Hamiltonian for Calculations in Complete $(sd)^n$ Spaces," *Bull. Am. Phys. Soc.* 27, 725 (1982).

31. C. Wong *et al.*, "Population of the 1^+ levels in ^{58}Co via the $^{58}Fe(p,n)$ reaction," *Phys. Rev. C* **18**, 2052 (1978).

32. *Instruction and Service Manual for the Cyclotron Corporation's Model CNI-15 Cyclotron*, pp. 3-93 to 3-96.

33. C. Wong *et al.*, "Population of the 1^+ levels in ^{58}Co via the $^{58}Fe(p,n)$ reaction," p. 2053.

34. Claude Francis Williamson, Jean-Paul Boujot, and Jean Picard, *Tables of Range and Stopping Power of Chemical Elements for Charged Particles of Energy 0.05 to 500 MeV: Report CEA-R 3042* (Saclay, France: Centre d'Etude Nucléaires de Saclay, 1966), p. 319.

35. *Ibid.*, p. 329.

36. *Ibid.*, p. 11. The authors state that: "In the domain $E > 1$ MeV/amu [and] $Z < 50$ both ranges and stopping powers appear to agree with published values to within 5% and often much better. Outside this domain, the discrepancy can be as high as 10% in the domain covered by the tables, but it is generally much less than this." Also, "It is felt that no entry in the tables is in error by more than 20%, and this degree of accuracy is quite sufficient for many purposes."

37. Robert C. Weast, ed., *Handbook of Chemistry and Physics, 55th Edition* (Cleveland, Ohio: CRC Press, 1974), pp. B256-B257.

38. M. Drosg, "Unified Absolute Differential Cross Sections for Neutron Production by the Hydrogen Isotopes for Charged-Particle Energies Between 6 and 17 MeV," *Nucl. Sci. and Eng.* 67, 190 (1978).

39. *Ibid.*

40. E.F. Plechaty *et al., UCRL-50400 Vol. 16, Rev. 2: Tabular and Graphical Presentation of 175 Neutron-Group Constants Derived from the LLL Evaluated-Nuclear-Data Library (ENDL)* (Livermore, California: UCRL, 1978), p. 84.

41. *Ibid.*, p. 90.

42. B.D. Walker *et al.*, "Quasi-Elastic (p,n) Angular Distributions: Instrumentation," *Nucl. Instr. and Meth.* 29, 333 (1964).

43. R.F. Bentley, Ph.D. Thesis, pp. 112, 127, 128, 132.

44. *Ibid.*, p. 112.

45. W.A. Sterrenburg *et al.*, "The ^{26}Mg(p,n)^{26}Al Reaction and the Energy Dependence of the Spin-Isospin Effective Interaction," p. 338.

46. Edgardo Browne *et al., Table of Isotopes, Seventh Edition,* ed. C. Michael Lederer and Virginia S. Shirley (New York: John Wiley & Sons, Inc., 1978), pp. 49, 154, 162.

47. P.M. Endt and C. Van der Leun, "Energy Levels of A = 21-44 Nuclei (VI)", *Nucl. Phys.* A310, pp. 171, 178, 181 (1978).

48. U.E.P. Berg *et al.*, "Comparison of ^{24,25,26}Mg(*p*,*n*)^{24,25,26}Al Cross Sections with Giant *M*1 Strength," p. 12.

49. Claude Francis Williamson *et al., CEA-R 3042*, p. 23.

50. *Ibid.*, p. 33.

51. R.F. Bentley, Ph.D. Thesis, pp. 112, 127, 128, 132.

52. W.A. Sterrenburg *et al.*, "The $^{26}Mg(p,n)^{26}Al$ Reaction and the Energy Dependence of the Spin-Isospin Effective Interaction," p. 330.

53. C. Maples, G.W. Goth, and J. Cerny, *UCRL-16964: Nuclear Reaction Q-Values* (Berkeley, California: UCRL, 1966), pp. 44, 117, 118.

54. S.D. Bloom, "Gamow-Teller Strength Functions with the Lanczos Algorithm," pp. 505-528.

55. S.D. Bloom, S.M. Grimes, and R.F. Hausman, Jr., "A Monte Carlo Method for Calculating Strength Functions in Many-Fermion Systems," *Phys. Lett.*, 93B, 227 (1980).

56. R.F. Hausman, Jr., *UCRL-52178: A Vector Method for Large Scale Configuration Interaction Problems* (Livermore, California: UCRL, 1976).

57. R.F. Hausman, Jr., S.D. Bloom, and C.F. Bender, "A New Technique for Describing the Electronic States of Atoms and Molecules-the Vector Method," *Chem. Phys. Lett.* 32, 483 (1975).

58. S.D. Bloom, "Gamow-Teller Strength Functions with the Lanczos Algorithm," pp. 506-507.

59. F. Petrovich, *et al.*, "Finite-Nucleus G Matrix in the Microscopic Description of Inelastic Proton Scattering," pp. 895-899.

60. R.R. Whitehead *et al.*, "Computational Methods for Shell-Model Calculations," in *Advances in Nuclear Physics, Vol. 9*, ed., M. Baranger and E. Vogt (New York: Plenum Press, 1977), pp. 123-176.

61. R.R. Whitehead, "Moment Methods and Lanczos Methods," in *Theory and Applications of Moment Methods in Many-Fermion Systems*, ed., B.J. Dalton *et al.* (New York: Plenum Press, 1980), pp. 235-55.

62. R. Schaeffer and J. Raynal, unpublished.

63. F.D. Becchetti, Jr., and G.W. Greenlees, "Nucleon-Nucleus Optical-Model Parameters, $A > 40$, $E < 50$ MeV," *Phys. Rev.* 182, 1190 (1969).

64. *Ibid.*, p. 1194.

65. J. Rapaport, V. Kulkarni, and R.W. Finlay, "A Global Optical-Model Analysis of Neutron Elastic Scattering Data," *Nucl. Phys.* **A330**, 15 (1979).

66. F.D. Becchetti, Jr., and G.W. Greenlees, "Nucleon-Nucleus Optical-Model Parameters, $A > 40$, $E < 50$," p. 1198.

67. G. Bertsch, J. Borysowicz, and H. McManus, "Interactions for Inelastic Scattering Derived from Realistic Potentials," *Nucl. Phys.* **A284**, 399 (1977).

68. *Ibid.*, p. 404.

69. Roderick V. Reid, Jr., "Local Phenomenological Nucleon-Nucleon Potentials," *Ann. of Phys.* 50, 411 (1968).

70. J.P. Elliott *et al.*, "Matrix Elements of the Nucleon-Nucleon Potential for Use in Nuclear-Structure Calculations," *Nucl. Phys.* A121, 241 (1968).

71. G. Bertsch *et al.*, "Interactions for Inelastic Scattering Derived from Realistic Potentials," pp. 402-403.

72. *Ibid.*, pp. 399-400.

73. *Ibid.*, p. 411.

74. J. Rapaport *et al.*, "Excitation of Giant Spin-Isospin Multipole Vibrations in ^{54,56}Fe and ^{58,60}Ni," p. 387.

75. C.D. Goodman *et al.*, "Gamow-Teller Matrix Elements from 0°(p,n) Cross Sections," p. 1757.

76. G. Bertsch *et al.*, "Interactions for Inelastic Scattering Derived from Realistic Potentials," p. 404.

77. Sam M. Austin, "An Empirical Effective Interaction," in *The (p,n) Reaction and the Nucleon-Nucleon Force*, ed. C.D. Goodman *et al.* (New York: Plenum Press, 1980), pp. 203-232.

78. R.R. Doering, D.M. Patterson, and Aaron Galonsky, "Microscopic description of isobaric-analog-state transitions induced by 25-, 35-, and 45-MeV protons," *Phys. Rev. C* **12**, 378 (1975).

79. R.F. Bentley, Ph.D. Thesis, pp. 153, 157.

80. W.A. Sterrenburg *et al.*, "The ^{26}Mg(p,n)^{26}Al Reaction and the Energy Dependence of the Spin-Isospin Effective Interaction," pp. 339-340.

VII. FIGURES

Figure 1a
Lawrence Livermore National Laboratory
Cyclograaff Facility

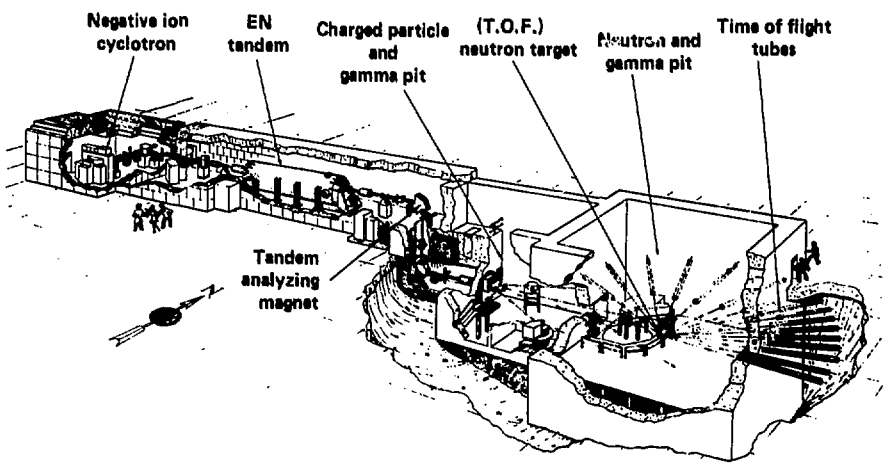

Figure 1b
Cyclotron

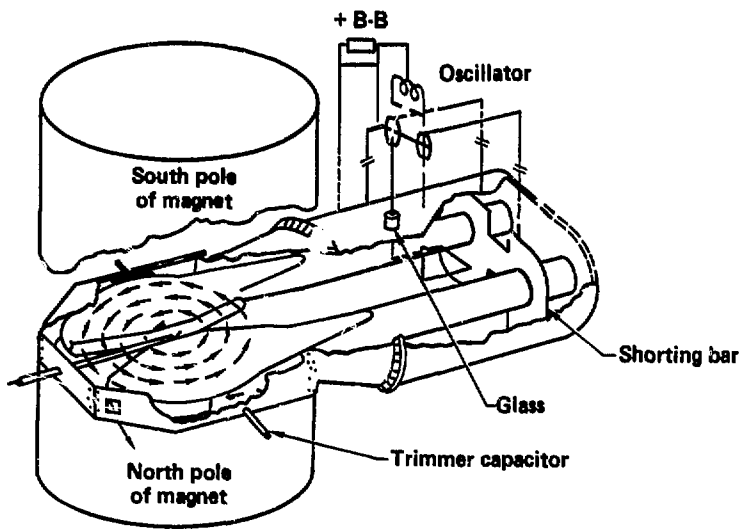

Figure 1c
Tandem Van de Graaff Accelerator

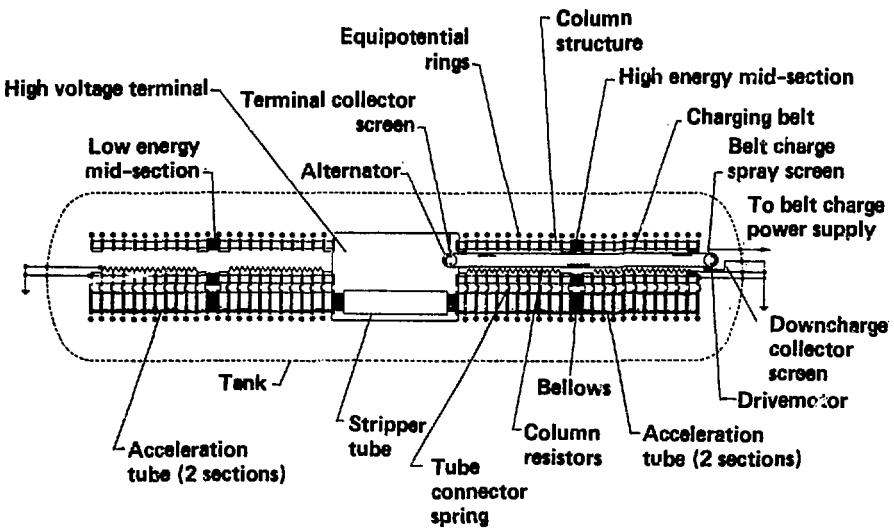

Figure 1d
Neutron TOF Pit

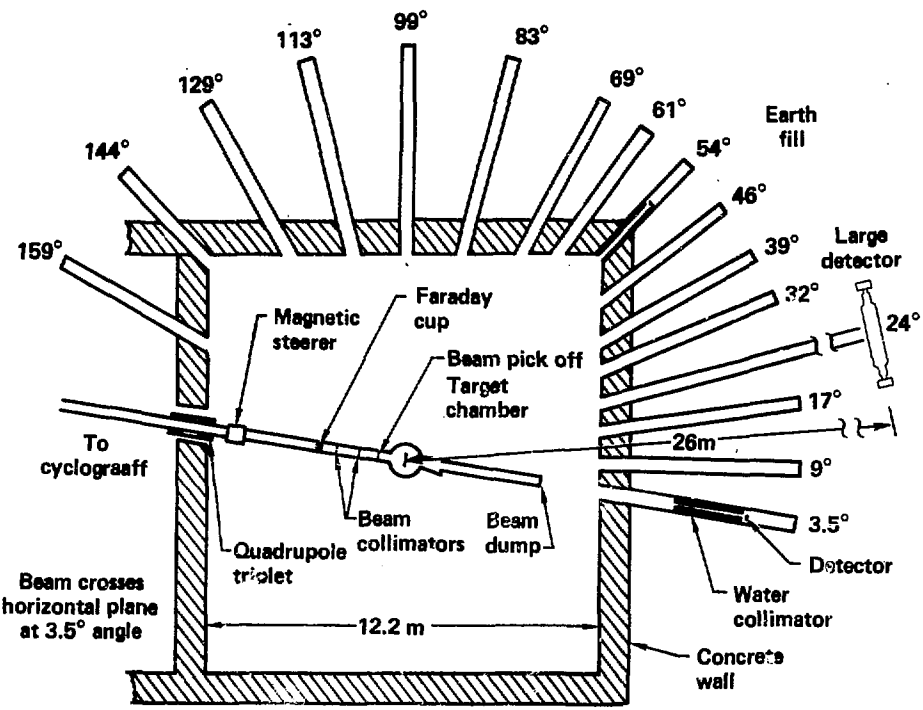

Figure 2

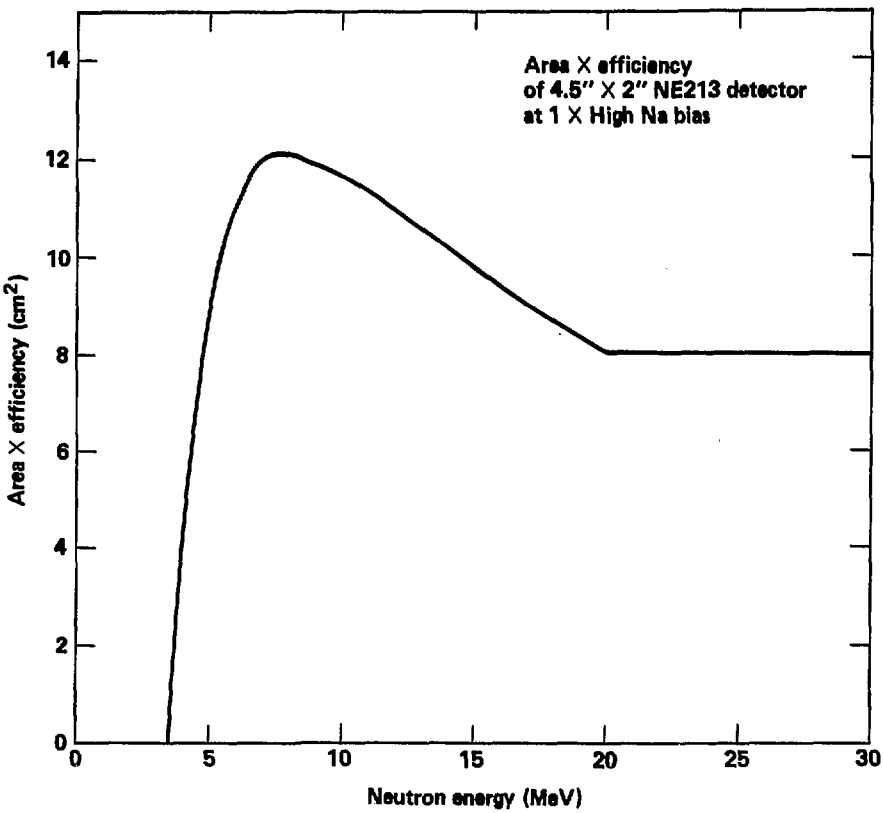

(Area X efficiency has 10.75 m air absorption correction, but does not have bubble correction)

Figure 3

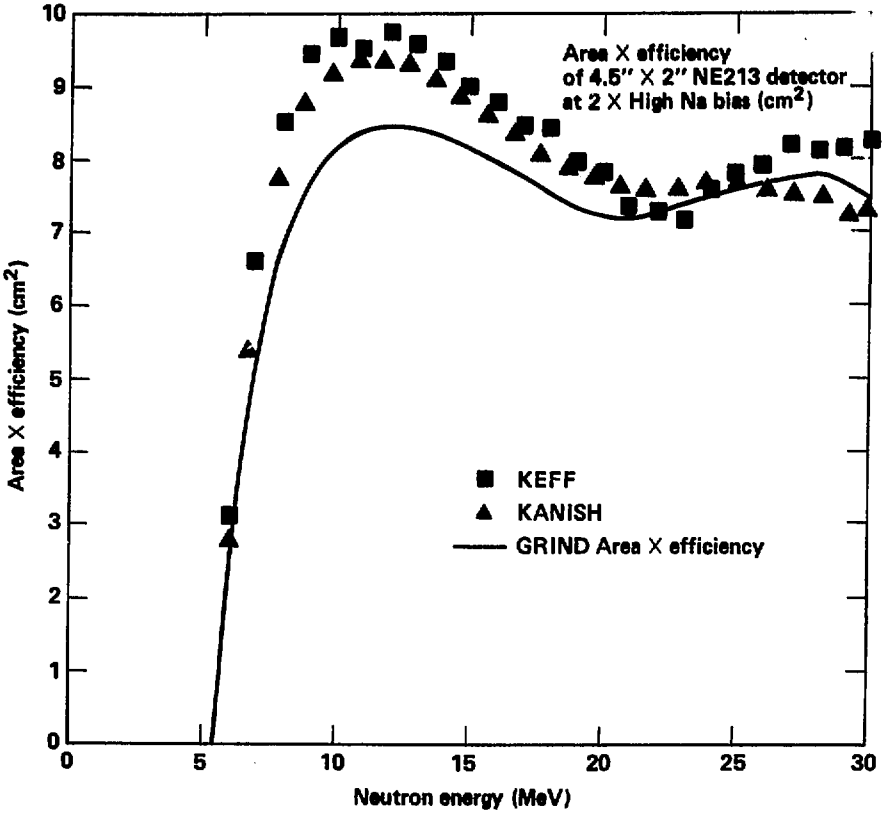

(Area X efficiency has 10.75 m air absorption correction, but does not have bubble correction)

Figure 4
Large detector

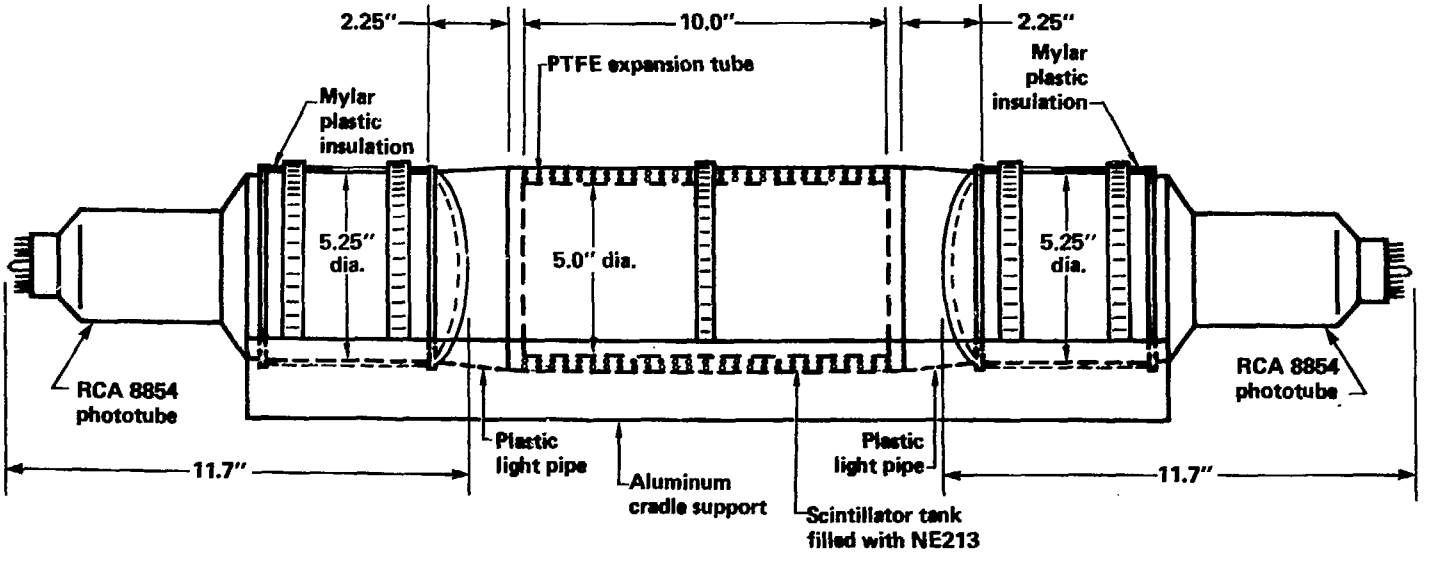

Figure 5a
July 1981 resistor chain in base

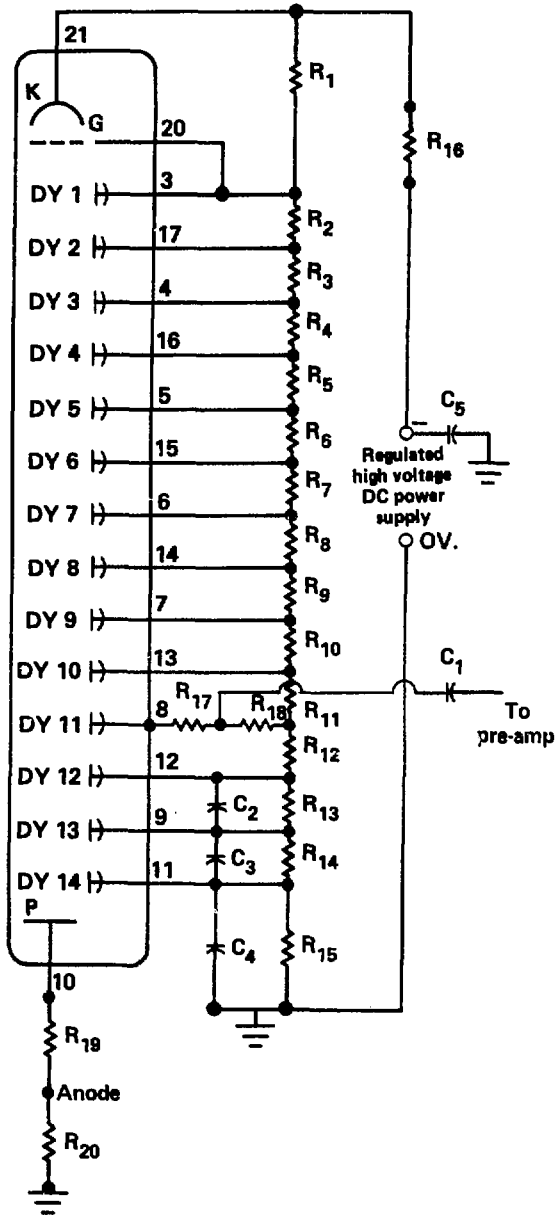

R_1 : 300 KΩ, 2 watts
R_2-R_{15}: 100 KΩ
R_{16} : 1KΩ, 2 watts
R_{17} : 200Ω
R_{18} : 2.2 MegΩ
R_{19} : 51Ω
R_{20} : 1 MegΩ
C_1 : 0.01μf, 1KV
C_2 : 0.01μf, 500V
C_3 : 0.02μf, 500V
C_4 : 0.05μf, 500V
C_5 : 0.005μf, 3KV

Tolerances of resistors are ± 5%. All resistors are 1/2 watt unless otherwise indicated.

Figure 5b
Preamp ($t_r \sim 20$ ns)

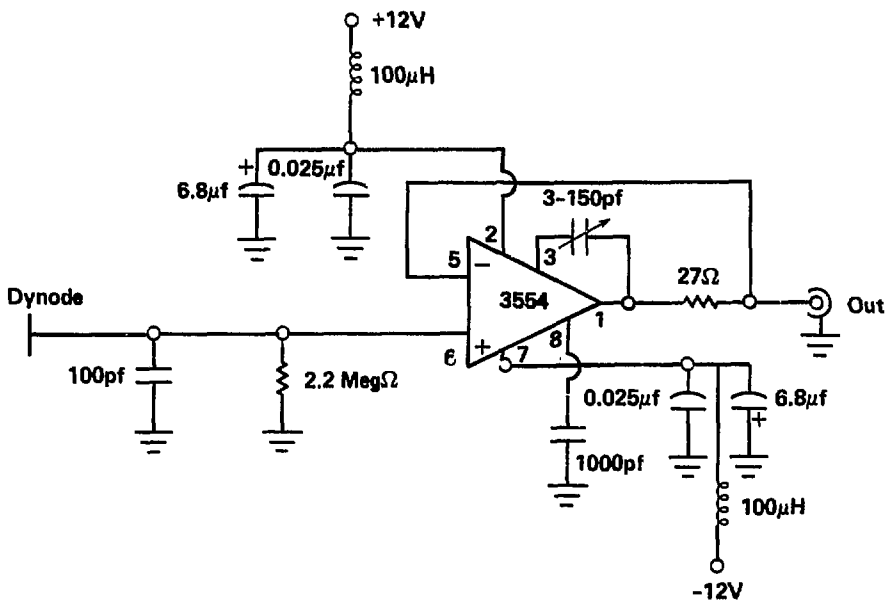

3554 wideband operational
amplifier is made by
Burr-Brown Research Corporation
of Tucson, Arizona

Figure 6
July 1981 Large Detector Time Resolution Circuit

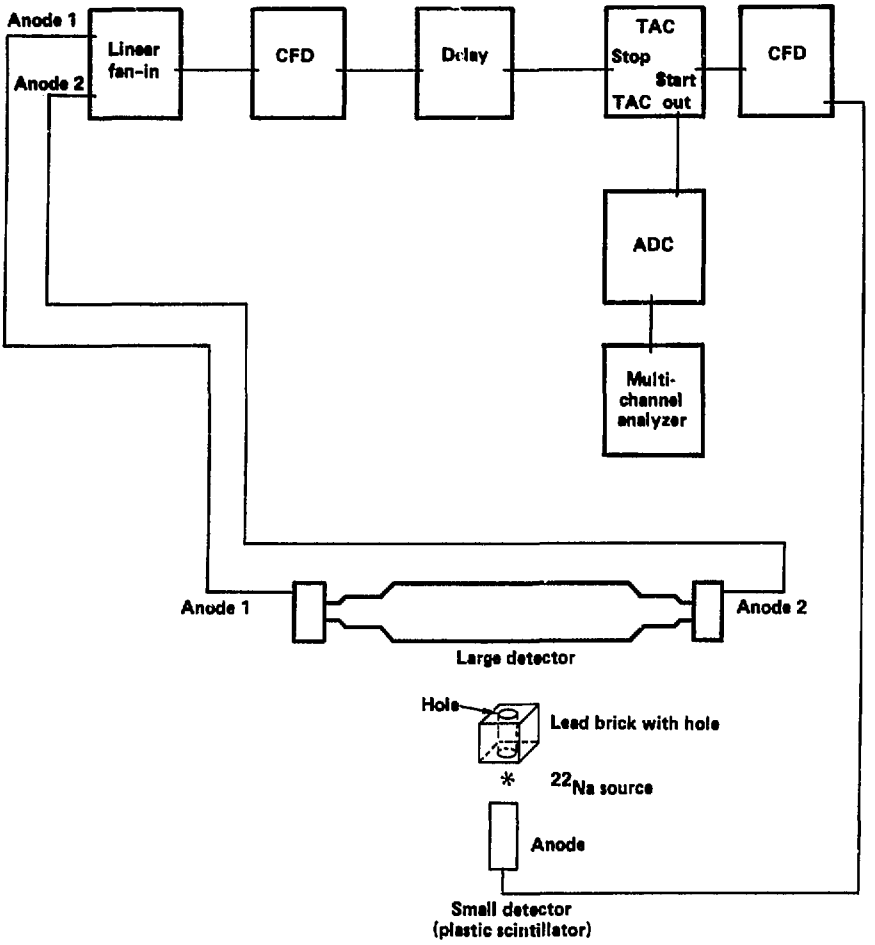

Description of Modules

Linear fan-in	≡ LeCroy Model 127C Dual Bipolar Linear Fan-in
CFD	≡ Ortec Model 473A Constant Fraction Discriminator
Delay	≡ Ortec Model 416A Gate and Delay Generator
TAC	≡ Ortec Model 467 Time to Pulse Height Converter and SCA
ADC	≡ Nuclear Data Analog to Digital Converter
Multichannel analyzer	≡ Nuclear Date 6620 Multichannel Analyzer

Figure 7
April 1983 resistor chain in base

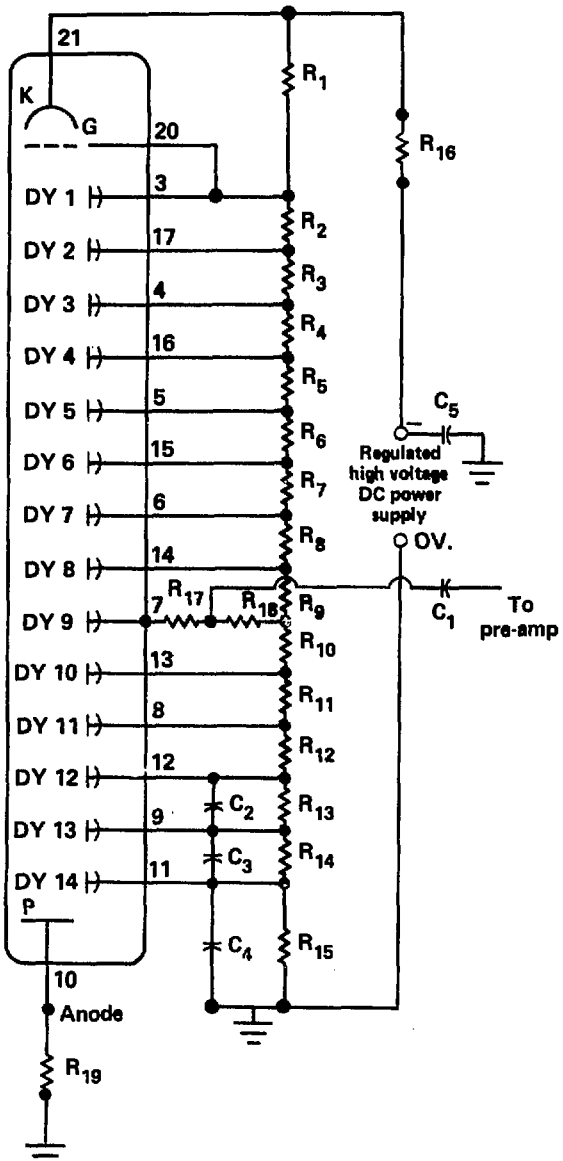

R_1 : 390 KΩ, 2 watt
R_2-R_3 : 130 KΩ
R_4-R_{11} : 100 KΩ
R_{12} : 150 KΩ
R_{13} : 180 KΩ
R_{14} : 200 KΩ
R_{15} : 240 KΩ
R_{16} : 1 KΩ, 2 watt
R_{17} : 200Ω
R_{18} : 2.2 MegΩ
R_{19} : 10 KΩ

C_1 : 0.01 μf, 1 KV
C_2 : 0.01 μf, 500 V
C_3 : 0.02 μf, 500 V
C_4 : 0.05 μf, 500 V
C_5 : 0.005 μf, 3 KV

Tolerances of resistors are ±5%. All resistors are 1/2 watt unless otherwise indicated.
Terminators of 51.1Ω are attached to the dynode and the anode outlets on the outside of the base, and the cables are attached to the terminators.

Figure 8.
July 1984 Large Detector Time Resolution

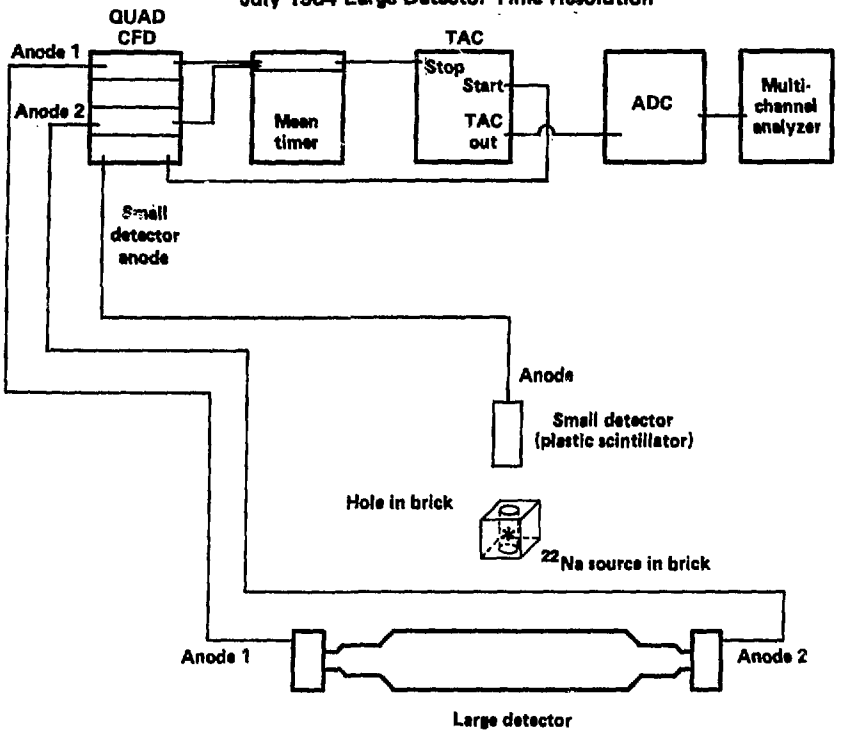

Description of Modules

QUAD CFD	≡ Ortec Model 934 Quad Constant-Fraction Discriminator
Mean Timer	≡ LeCroy Model 624 Octal Meantimer
TAC	≡ Ortec Model 467 Time to Pulse Height Converter and SCA
ADC	≡ Nuclear Data Analog to Digital Converter
Multichannel analyzer	≡ Nuclear Data 6620 Multichannel Analyzer

Figure 9
July 1981 0° Large Detector Circuit

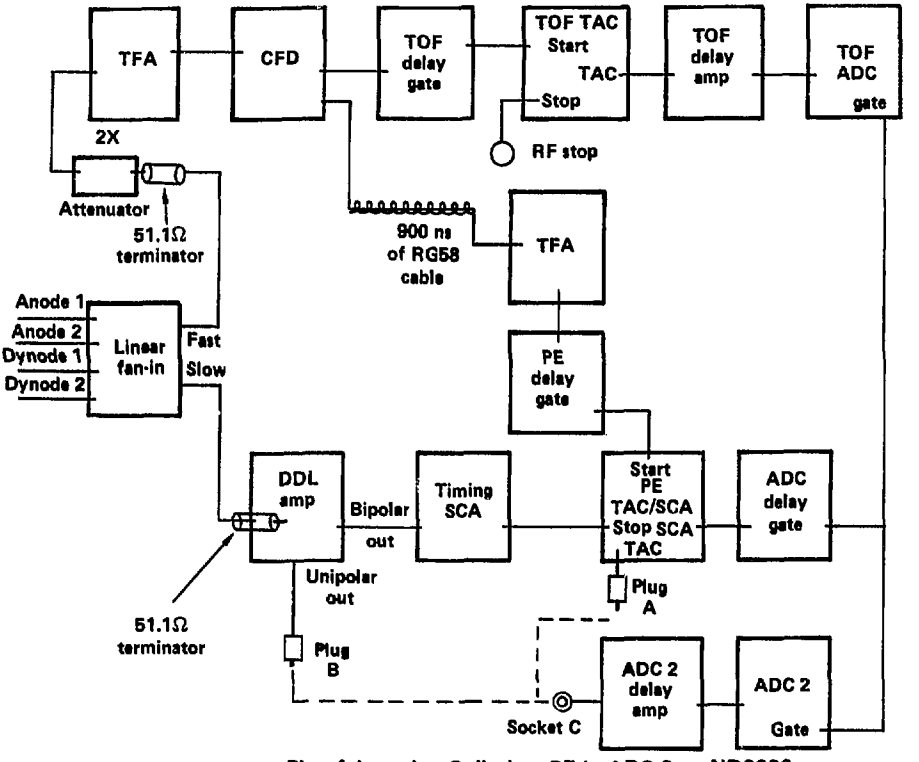

Plug A in socket C displays PE in ADC 2 on ND6620
Plug B in socket C displays pulse-height in ADC 2 on ND6620

Description of Modules

Linear fan-in	≡ LeCroy Model 127C Dual Bipolar Linear Fan-In
2 X attenuator	≡ 50Ω Tektronix 011-0069-02 2 X Attenuator
TFA	≡ EG&G Ortec 454 Timing Filter Amplifier
CFD	≡ EG&G Ortec 473A Constant Fraction Discriminator
TOF delay gate PE delay gate ADC delay gate	≡ EG&G Ortec Model 416A Gate and Delay Generator
TOF delay amp ADC2 delay amp	≡ EG&G Ortec Model 427A Delay Amplifier
TOF TAC	≡ Canberra Time Analyzer Model 1443
PE TAC/SCA	≡ EG&G Ortec Model 467 Time to Pulse Height Converter and SCA
DDL amp	≡ EG&G Ortec Model 460 Delay Line Amplifier
Timing SCA	≡ EG&G Ortec Model 551 Timing Single-Channel Analyzer

Figure 10
April 1983 Large Detector Circuit

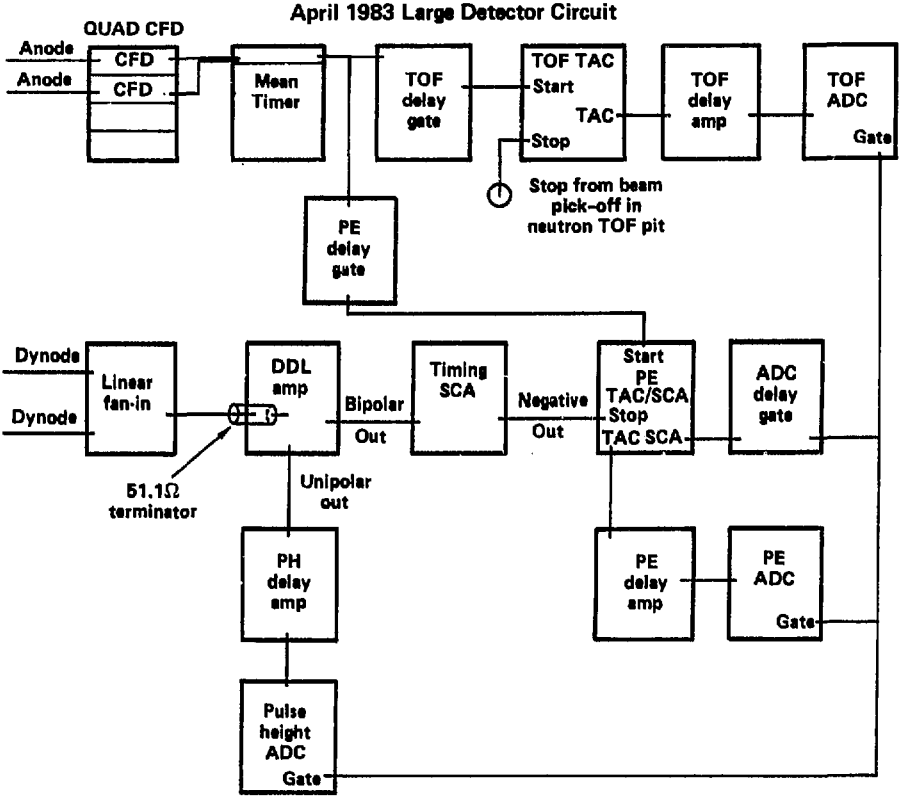

Description of Modules

QUAD CFD	≡ EG&G Ortec Model 934 Quad Constant-Fraction 100-MHz Discriminator
TFA	≡ EG&G Ortec Model 474 Timing Filter Amplifier
Mean Timer	≡ LeCroy 624 Octal Meantimer
TOF delay gate PE delay gate ADC delay gate	≡ EG&G Ortec Model 416A Gate and Delay Generator
TOF delay amp PH delay amp PE delay amp	≡ EG&G Ortec Model 427A Delay Amplifier
TOF TAC PE TAC/SCA	≡ EG&G Ortec Model 467 Time to Pulse Height Converter and SCA
Linear fan-in	≡ LeCroy Model 127C Dual Bipolar Linear Fan-In
DDL amp	≡ EG&G Ortec Model 460 Delay Line Amplifier
Timing SCA	≡ EG&G Ortec Model 551 Timing Single-Channel Analyzer

Figure 11
15-Detector Electronics
(Detector no. 4 is not
connected to this circuit
for our (p,n) runs)

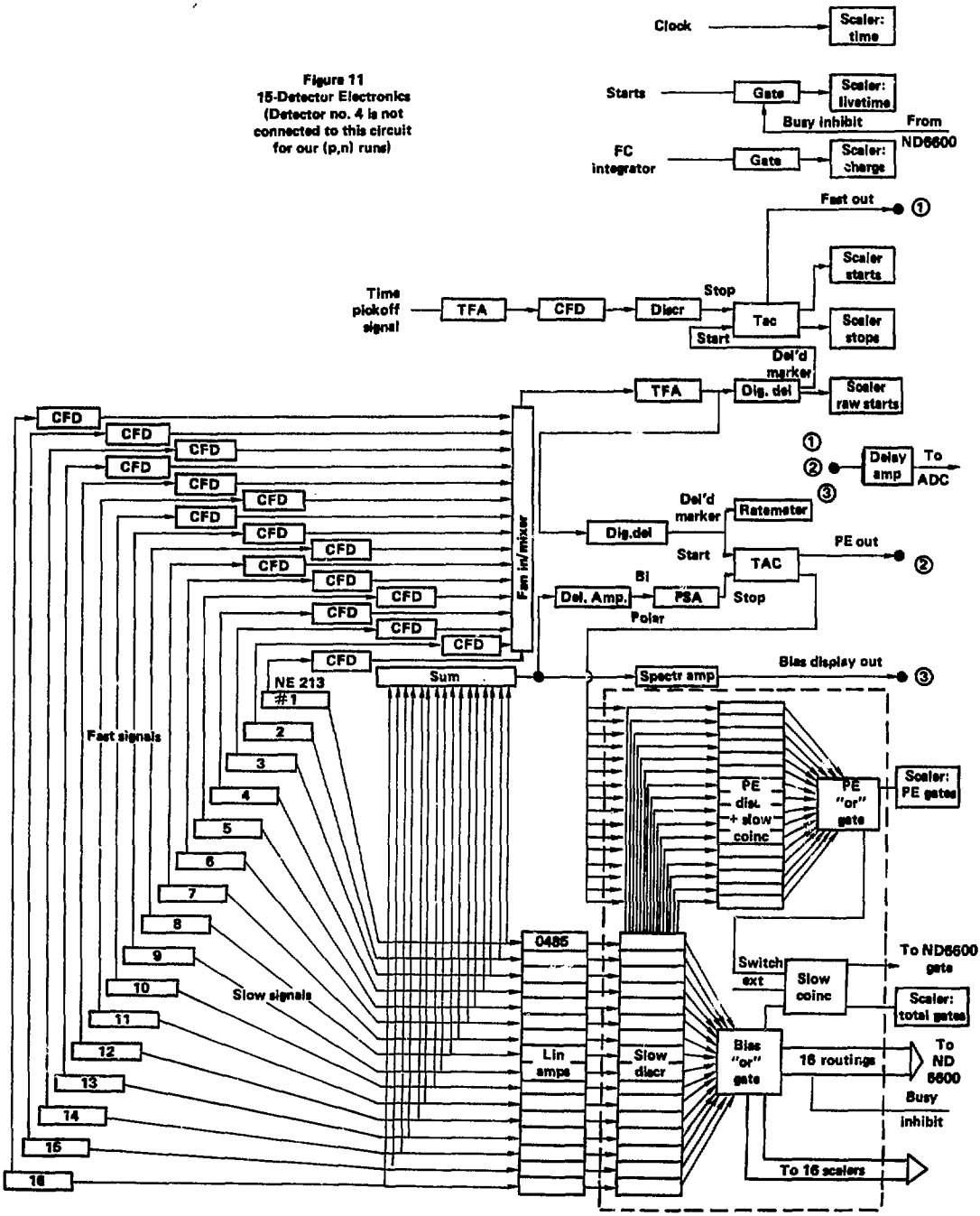

Figure 12
Pulse Height

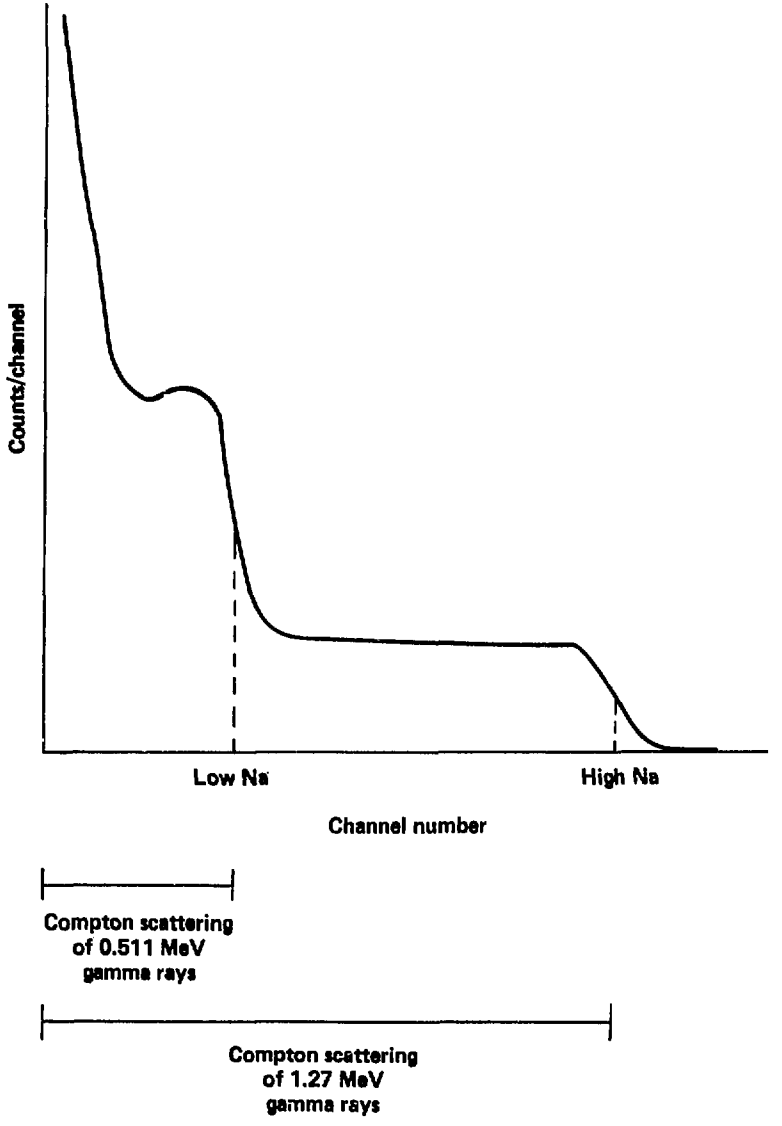

Figure 13

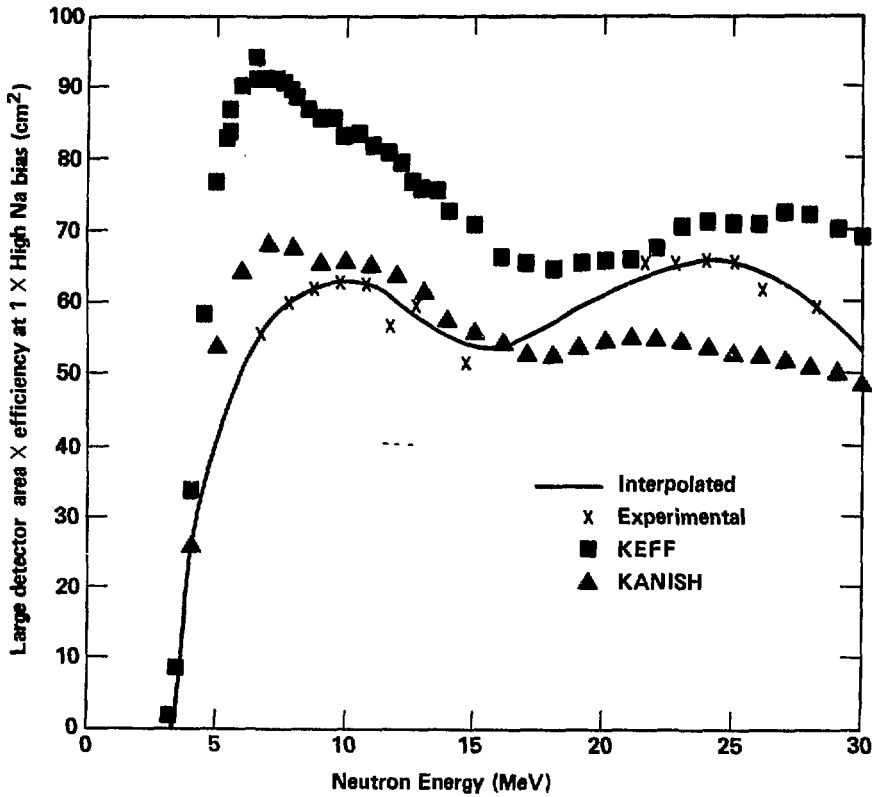
Large detector area X efficiency at 1 X High Na bias (cm²)
Neutron Energy (MeV)
Interpolated
Experimental
KEFF
KANISH
0
10
20
30
40
50
60
70
80
90
100
0
5
10
15
20
25
30

Figure 14

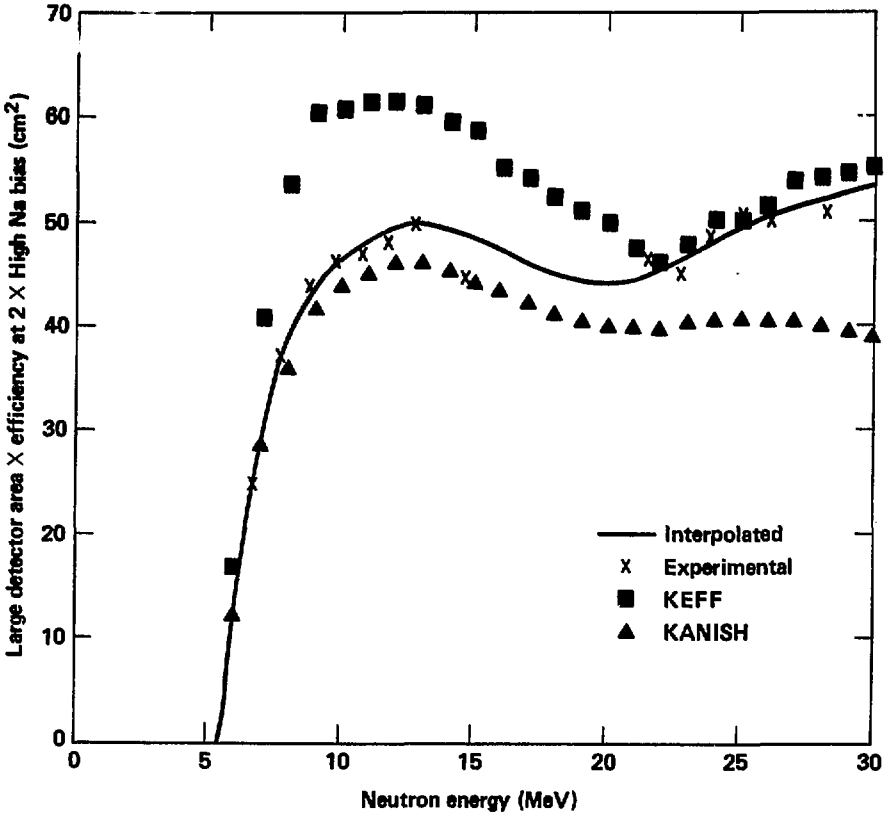
Large detector area X efficiency at 2 X High Na bias (cm²)
70
60
50
40
30
20
10
0
0
5
10
15
20
25
30
Neutron energy (MeV)
Interpolated
Experimental
KEFF
KANISH

Figure 15

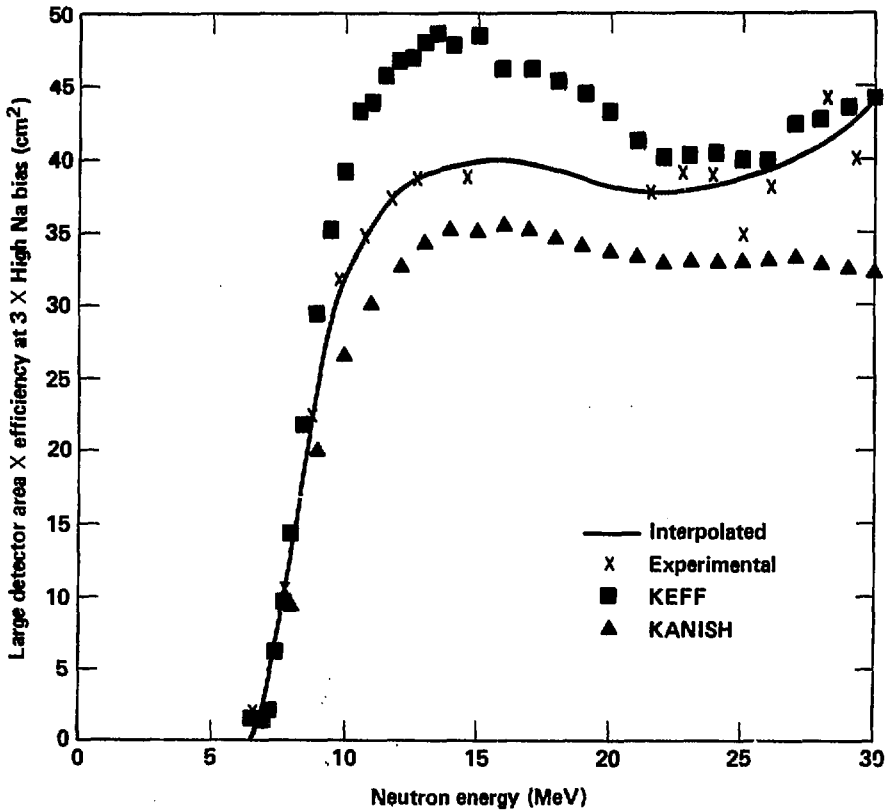
Large detector area X efficiency at 3 X High Na bias (cm²)
Neutron energy (MeV)
Interpolated
Experimental
KEFF
KANISH
0
5
10
15
20
25
30
35
40
45
50

Figure 16

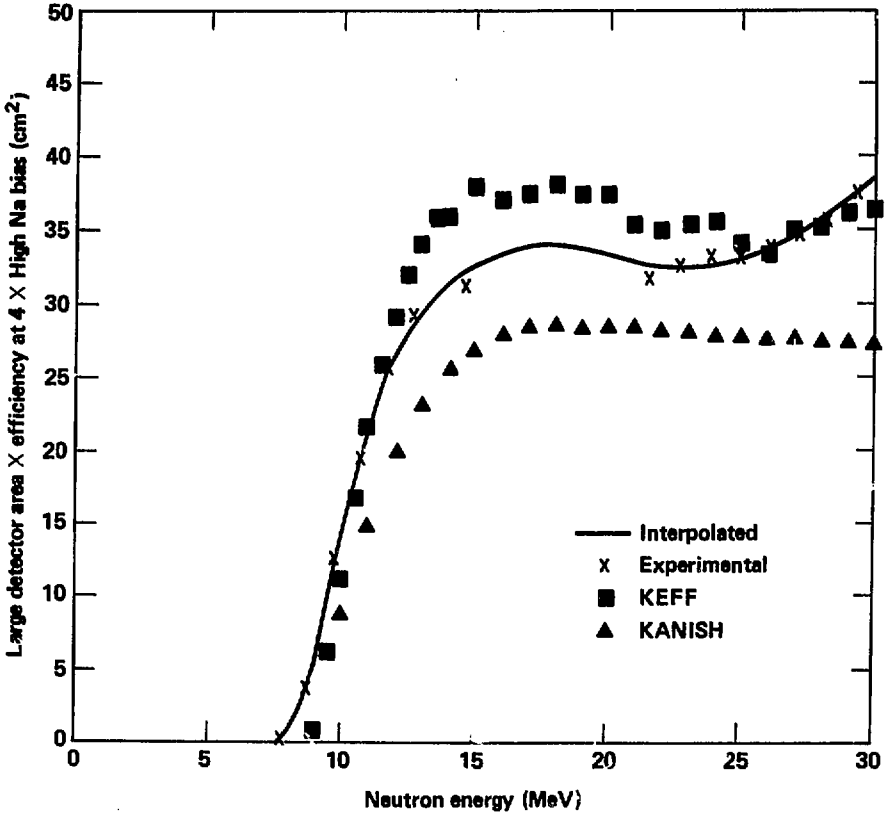
Large detector area X efficiency at 4 X High Na bias (cm²)
Neutron energy (MeV)
Interpolated
Experimental
KEFF
KANISH
0
5
10
15
20
25
30
35
40
45
50

Figure 17

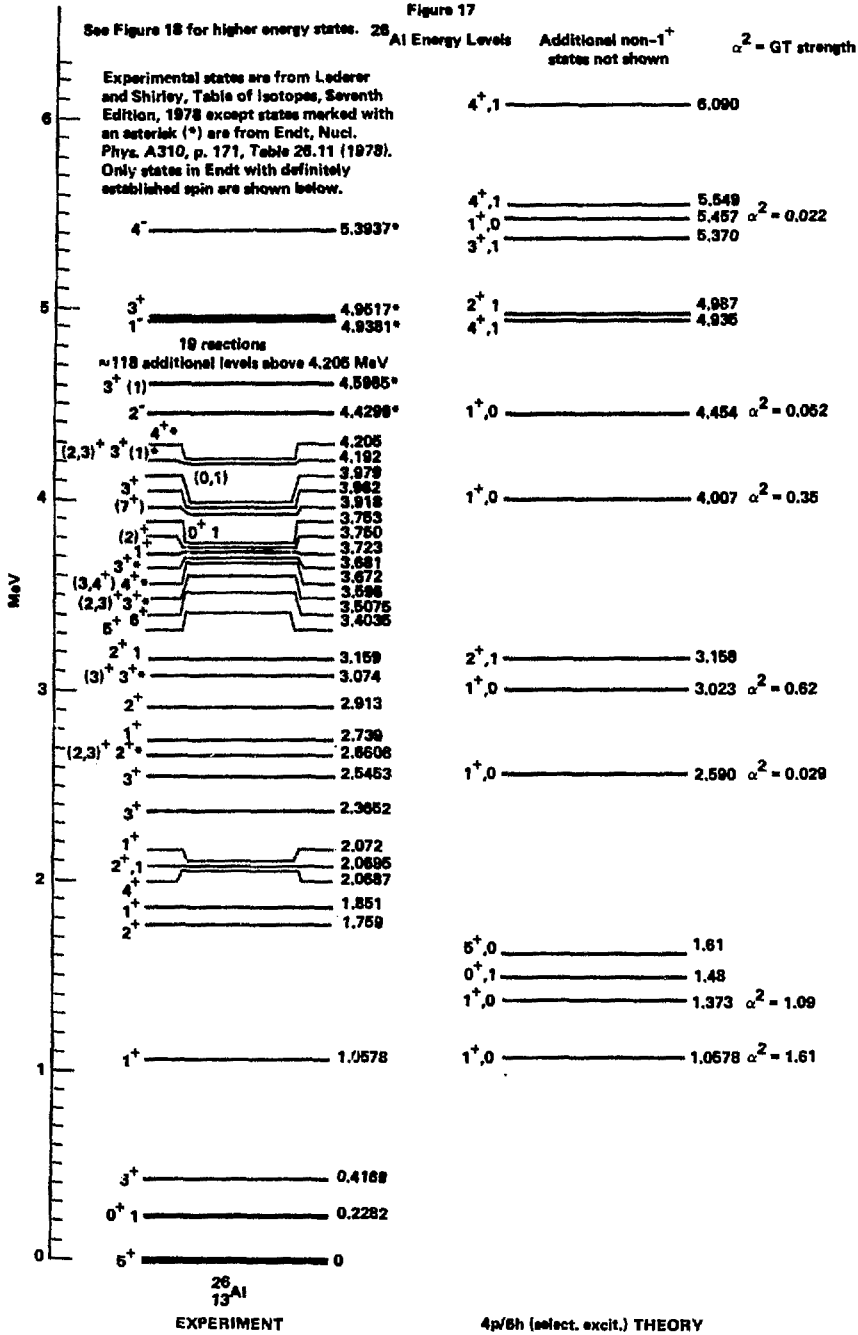
See Figure 18 for higher energy states.
$^{26}_{13}$Al Energy Levels
Additional non-1$^+$ states not shown
α^2 = GT strength
Experimental states are from Lederer and Shirley, Table of Isotopes, Seventh Edition, 1978 except states marked with an asterisk (*) are from Endt, Nucl. Phys. A310, p. 171, Table 26.11 (1978). Only states in Endt with definitely established spin are shown below.
MeV
19 reactions
≈118 additional levels above 4.206 MeV
$^{26}_{13}$Al
EXPERIMENT
4p/6h (select. excit.) THEORY

Figure 18

^{28}Al Energy Levels (continued)
[T = 1 levels]

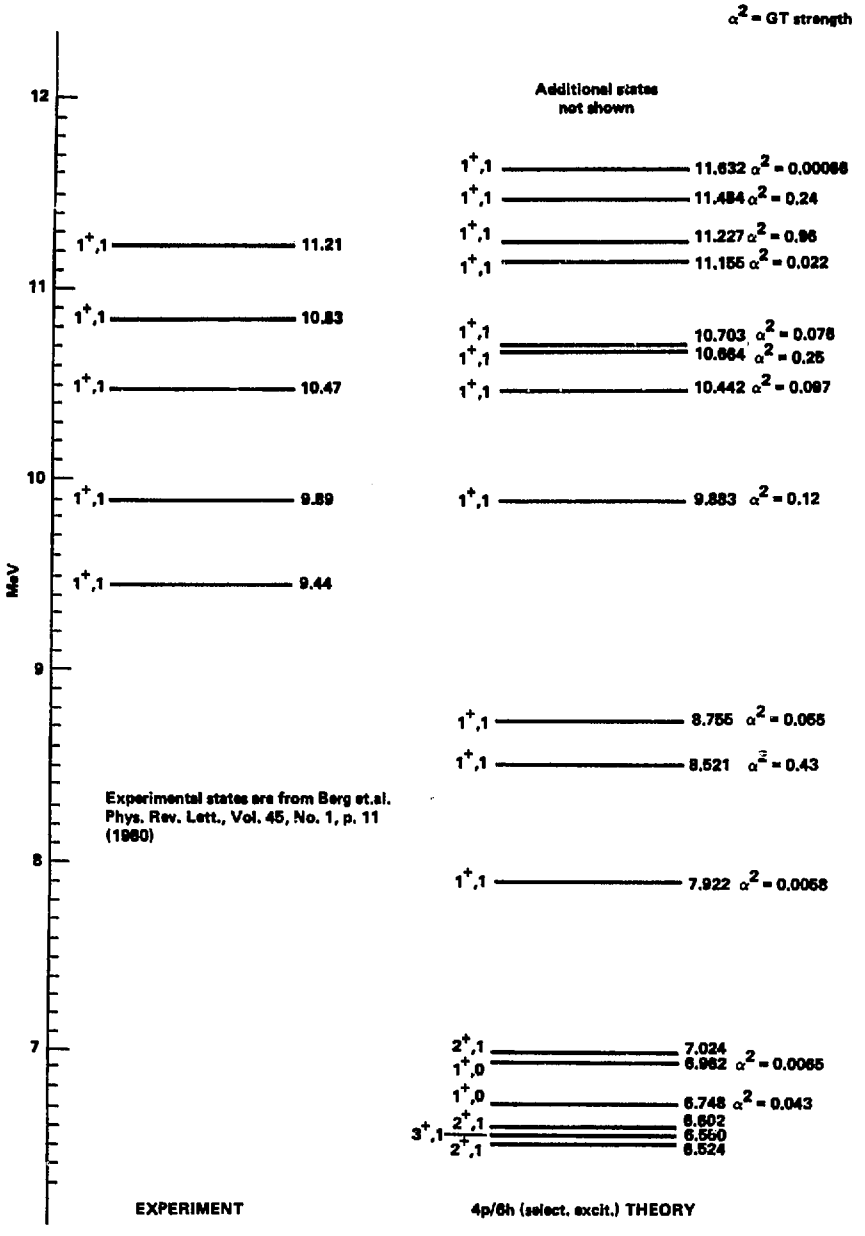

Figure 19
^{54}Co Energy Levels

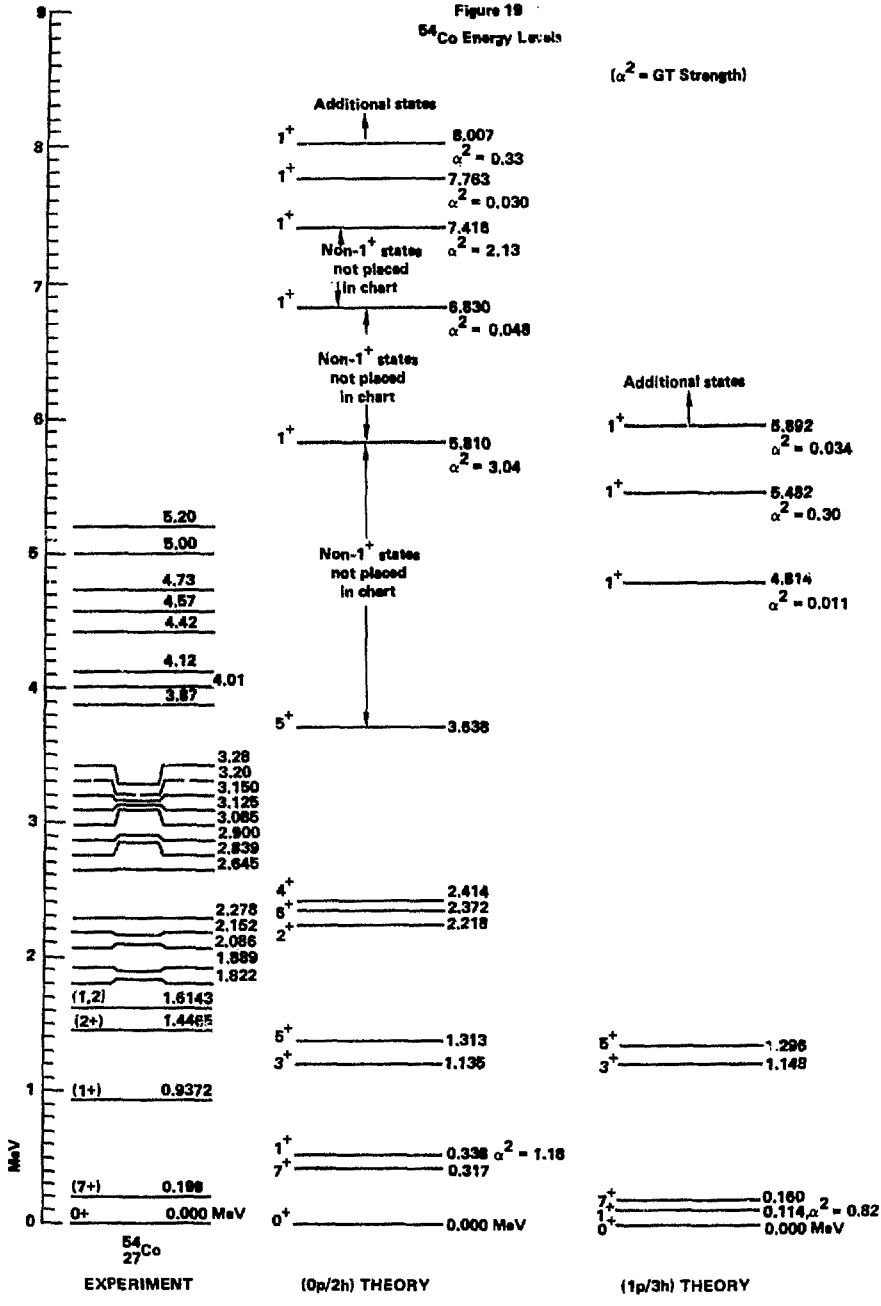

Experimental states are from Lederer and Shirley, Table of Isotopes, Seventh Edition, 1978.

Figure 20
^{56}Co Energy Levels

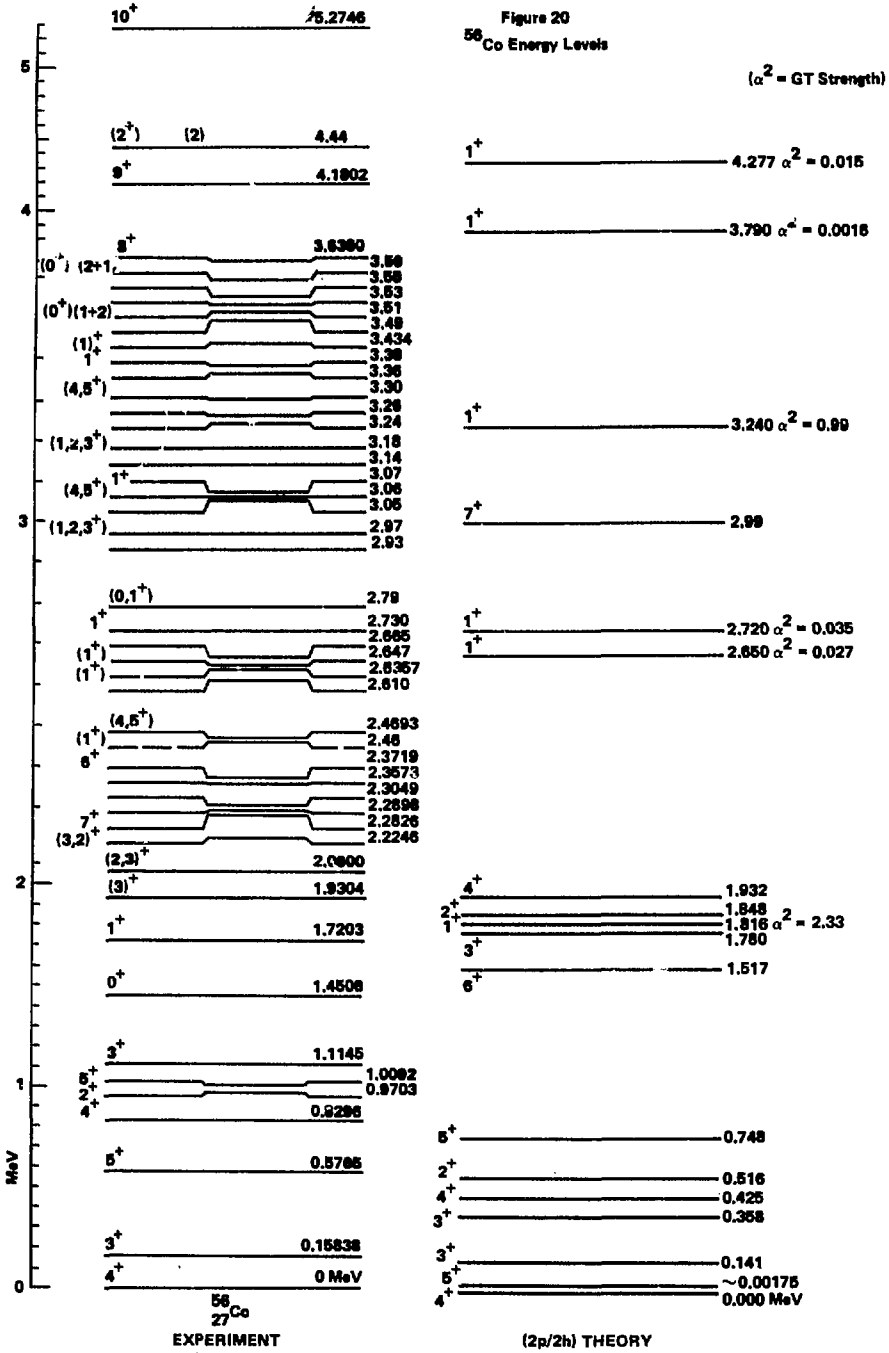

Experimental states are from Lederer and Shirley, Table of Isotopes, Seventh, Edition, 1978.

Figure 21
$^{56}Fe(p,n)^{56}Co$, Ep = 19.11 MeV
Large detector TOF spectrum
(θ_{Lab} = 23.8°)

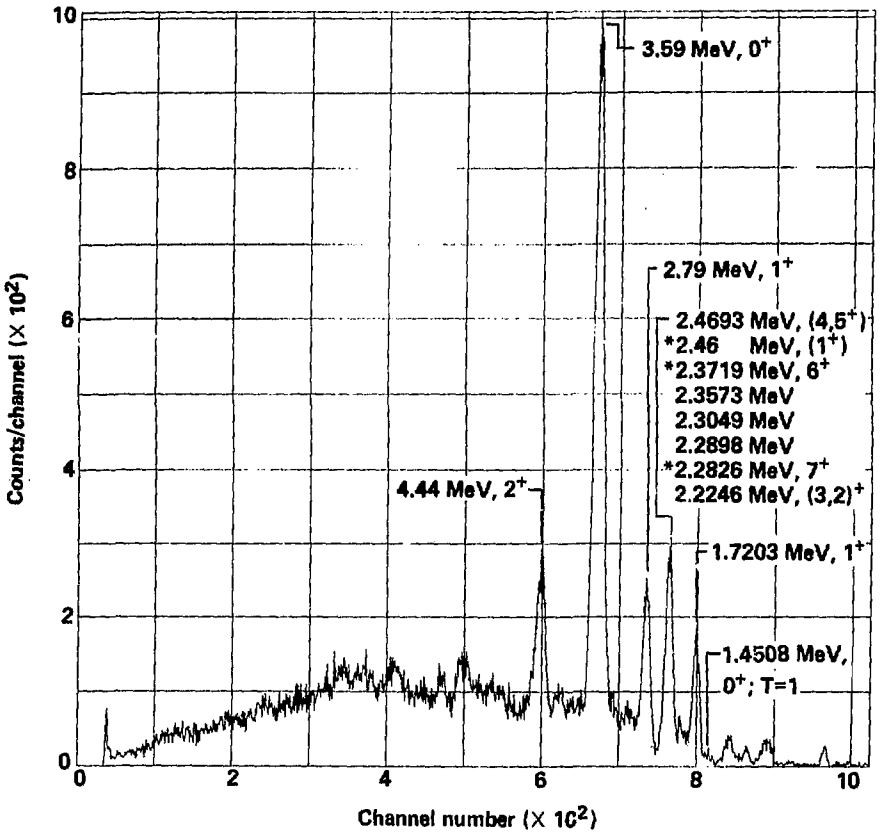

States are from Lederer and Shirley, Table of Isotopes, Seventh Edition, 1978.
States labelled with an asterisk are not listed as being populated by $^{56}Fe(p,n)$ or $^{56}Fe(p,n\gamma)$ in Lederer and Shirley.
Locations of states are approximate.

Figure 22
$^{56}Fe(p,n)^{56}Co$, Ep = 19.11 MeV
Small detector TOF spectrum
(θ_{Lab} = 32.3°)

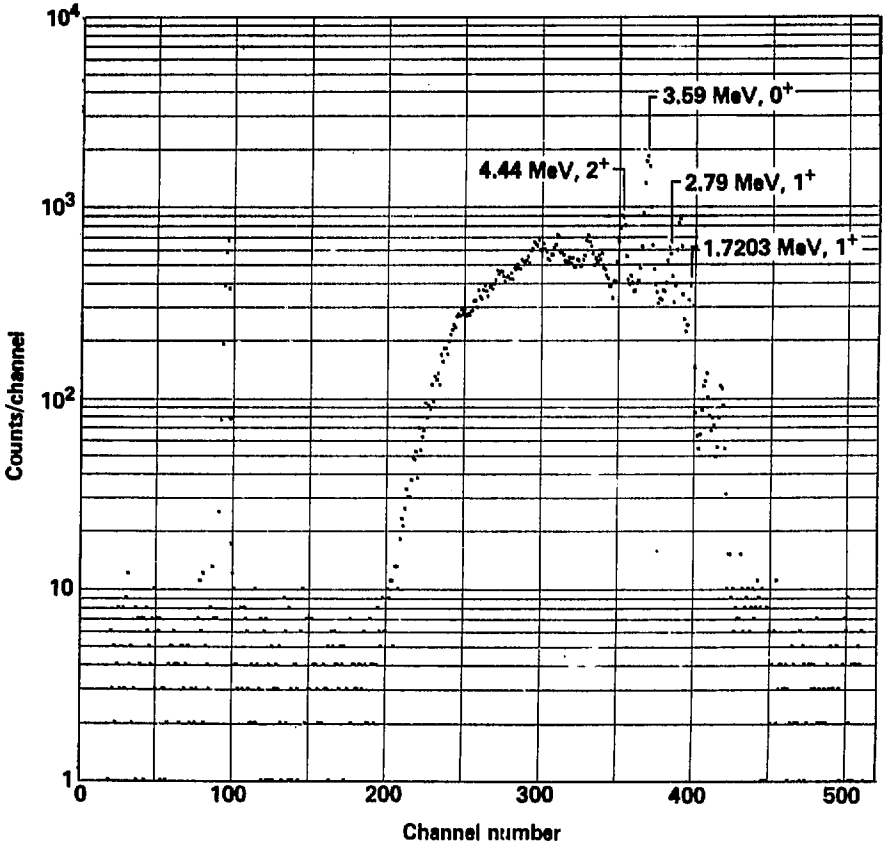

Figure 23
$^{26}Mg(p,n)^{26}Al$, Ep = 19.12 MeV
Large detector TOFFEE spectrum
(θ_{Lab} = 23.8°)
Averaged data

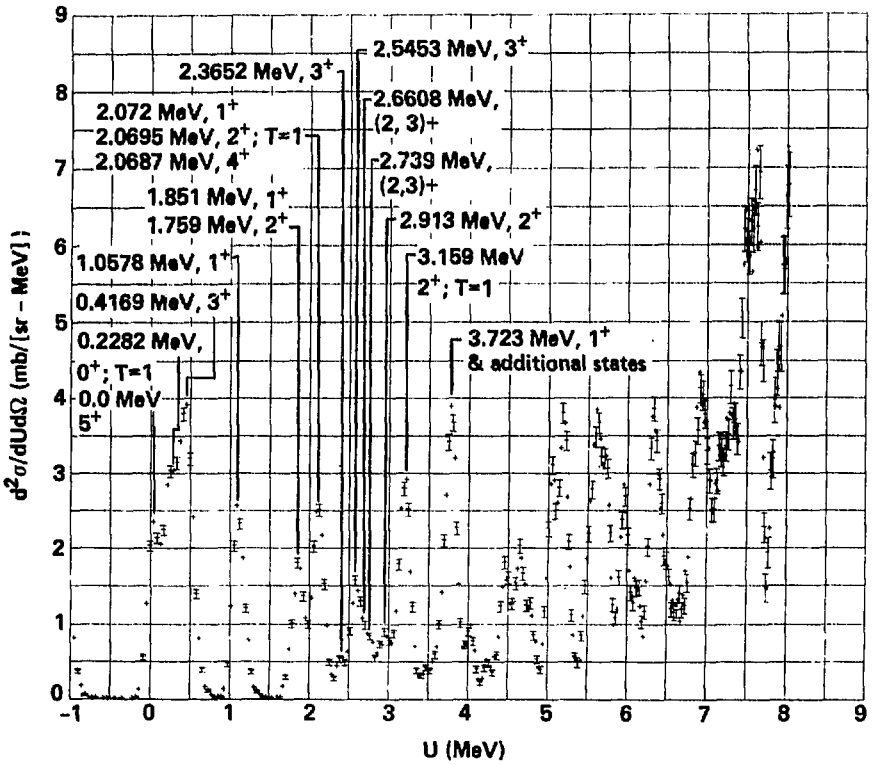

States are from Lederer and Shirley, Table of Isotopes, Seventh Edition, 1978.
Locations of states are approximate.

Figure 24
$^{26}Mg(p,n)^{26}Al$, Ep = 19.12 MeV
Large detector TOFFEE spectrum
(θ_{Lab} = 23.8°)
Unaveraged data
Expanded scale with hand drawn curves

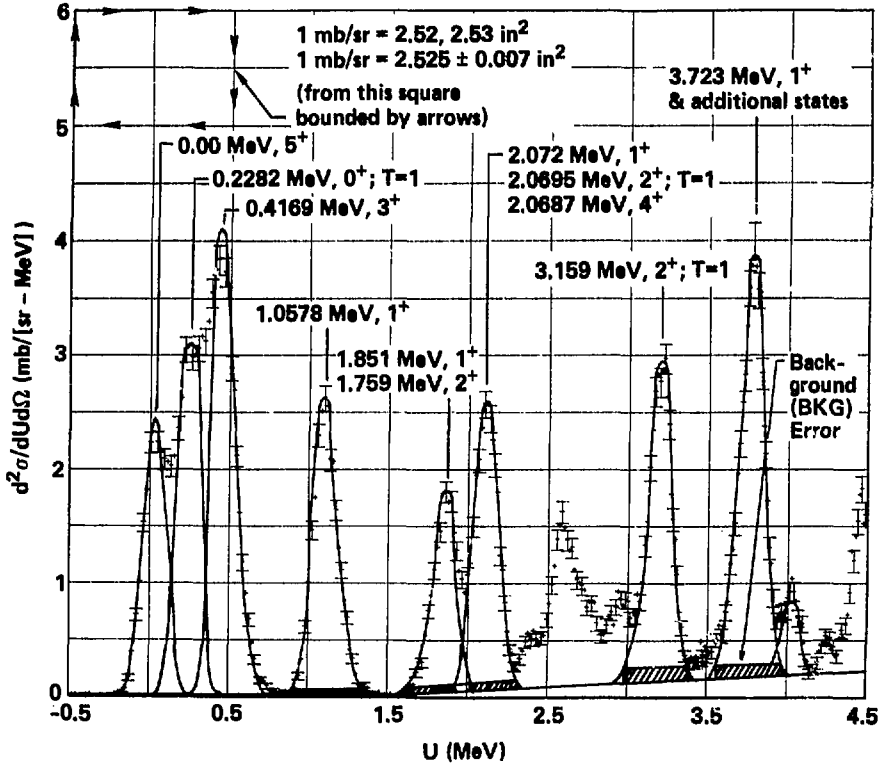

Figure 25
$^{26}Mg(p,n)^{26}Al$, Ep = 24.97 MeV
Large detector TOFFEE spectrum
(θ_{Lab} = 23.8°)
Averaged data

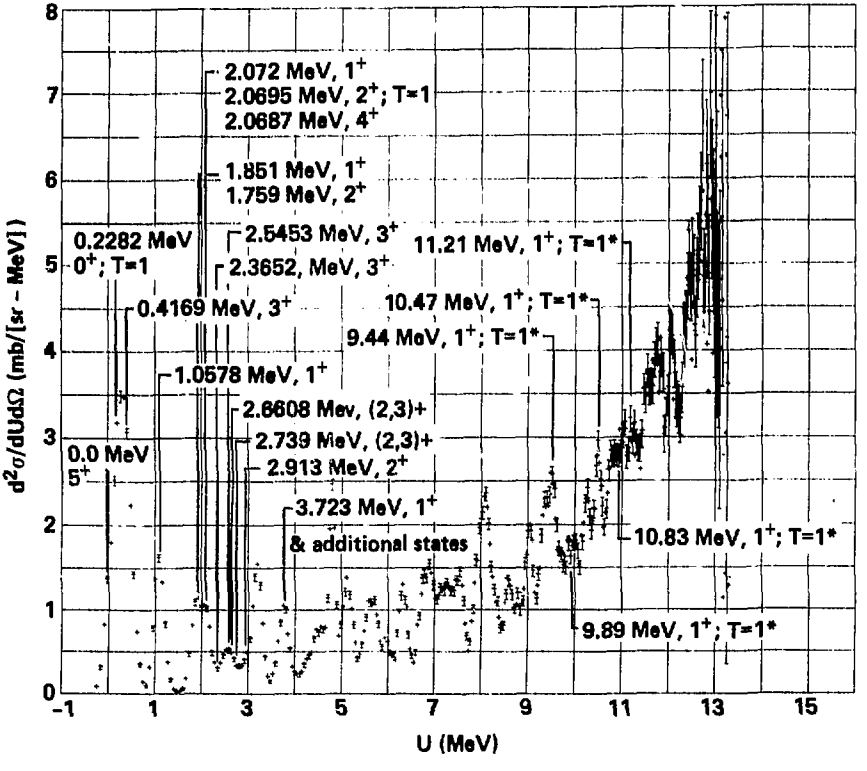

States are from Lederer and Shirley, Table of Isotopes, Seventh Edition, 1978; except states with asterisk are from Phys. Rev. Lett. Vol. 45, No. 1, 7 July 1980.
Locations of states are approximate.

Figure 26
$^{54}Fe(p,n)^{54}Co$, Ep = 17.20 MeV
Large detector TOFFEE spectrum
(θ_{Lab} = 23.8°)
Averaged data

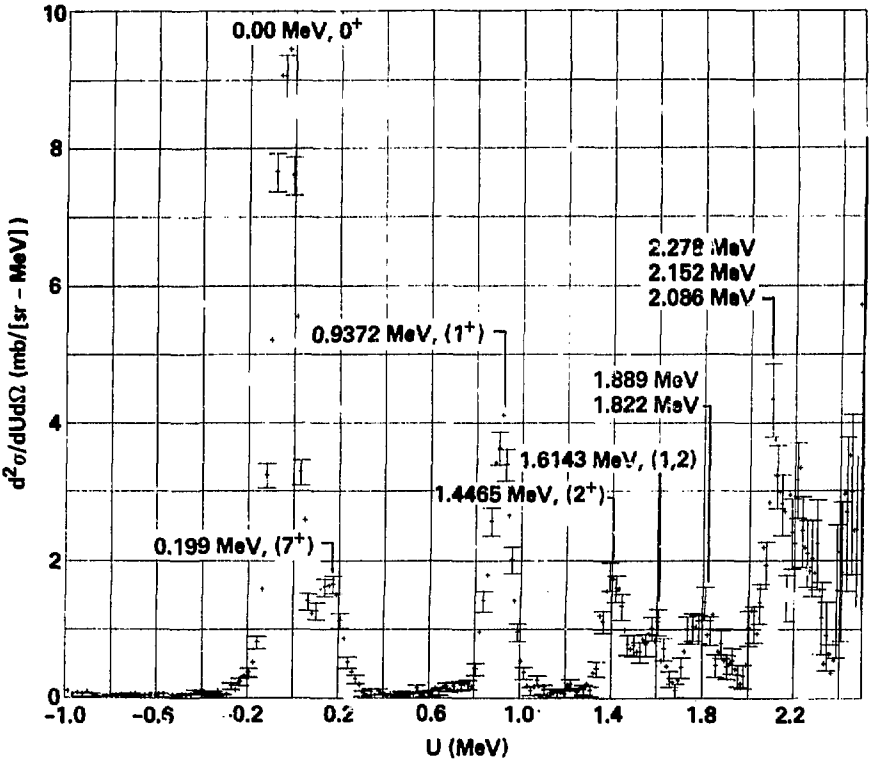

States are from Lederer and Shirley, Table of Isotopes, Seventh Edition, 1978.
Locations of states are approximate.

Figure 27
$^{54}Fe(p,n)^{54}Co$, Ep = 18.60 MeV
Large detector TOFFEE spectrum
(θ_{Lab} = 23.8°)
Averaged data

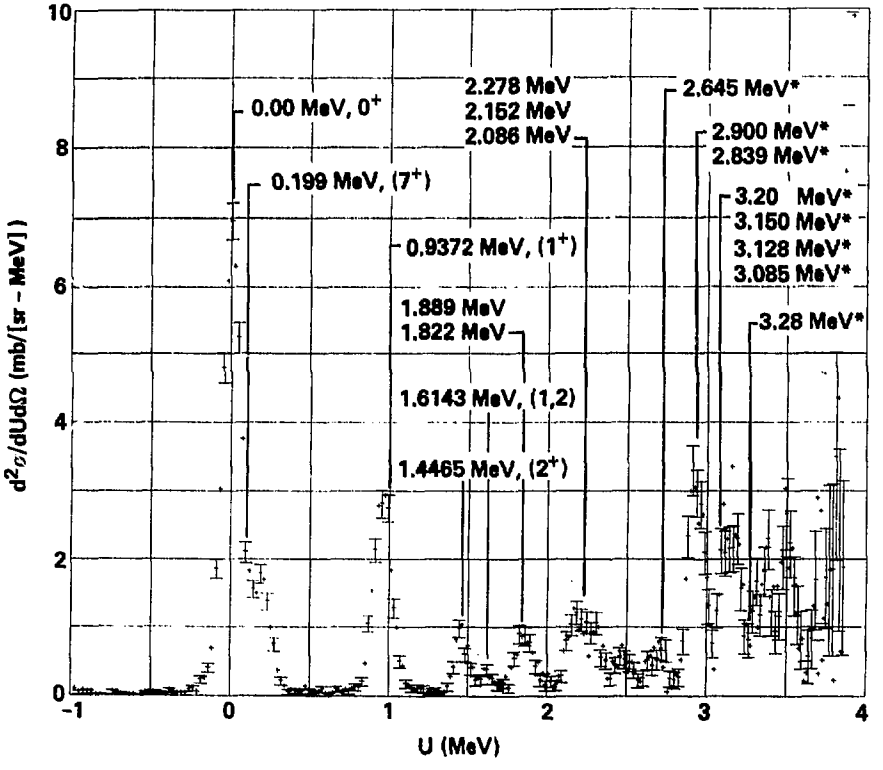

States are from Lederer and Shirley, Table of Isotopes, Seventh Edition, 1978.
States labelled with an asterisk are not listed as being populated by $^{54}Fe(p,n\gamma)$ or $^{54}Fe(p,n)$ in Lederer and Shirley.
Locations of states are approximate.

Figure 28
^{54}Fe(p,n)^{54}Co, Ep = 24.60 MeV
Large detector TOFFEE spectrum
(θ_{Lab} = 23.8°)
Averaged data

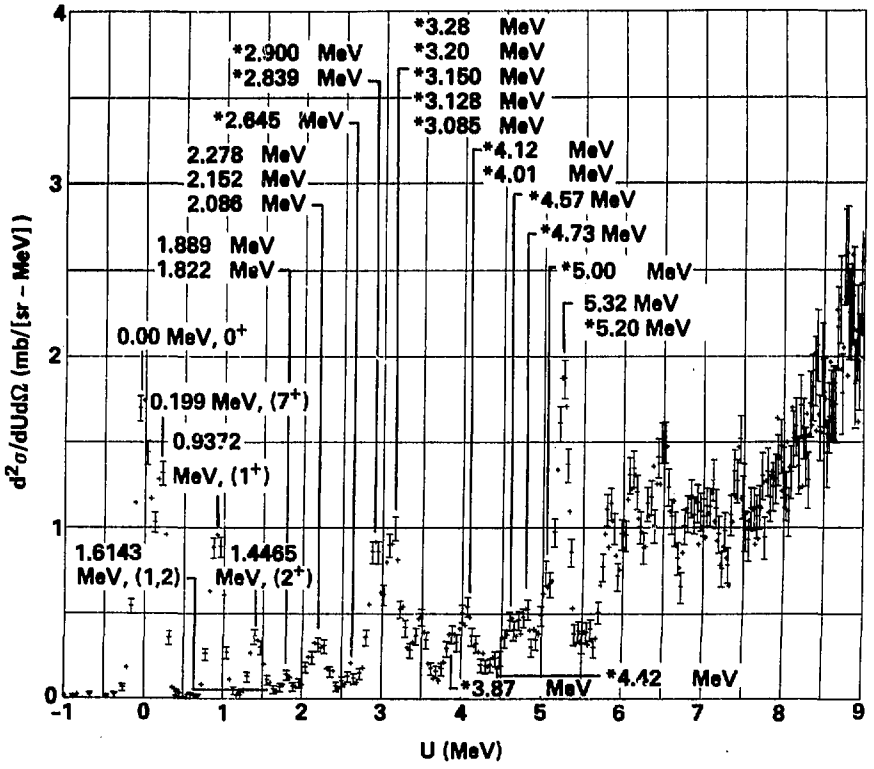

States are from Lederer and Shirley, Table of Isotopes, Seventh Edition, 1978; with the exception of the 5.32 MeV state which is from the PRL 47(5), 301-304 (3 Aug. 1981).
States labelled with an asterisk are not listed as being populated by ^{54}Fe(p,n) or ^{54}Fe(p,nγ) in Lederer and Shirley.
Locations of states are approximate.

Figure 29
$^{56}Fe(p,n)^{56}Co$, Ep = 19.11 MeV
Large detector TOFFEE spectrum
(θ_{Lab} = 23.8°)
Averaged data

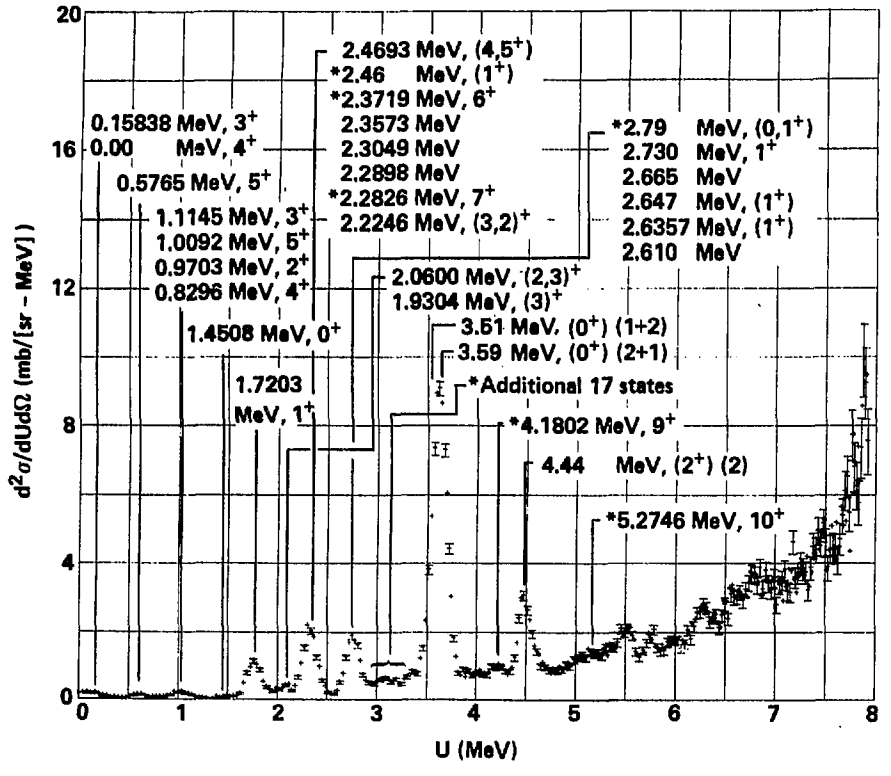

States are from Lederer and Shirley, Table of Isotopes, Seventh Edition, 1978.
States labelled with an asterisk are not listed as being populated by $^{56}Fe(p,n)$ or $^{56}Fe(p,n\gamma)$ in Lederer and Shirley.
Locations of states are approximate.

Figure 30
^{56}Fe(p,n)^{56}Co, Ep = 24.59 MeV
Large detector TOFFEE
Spectrum (θ_{Lab} = 23.8°)
Averaged data

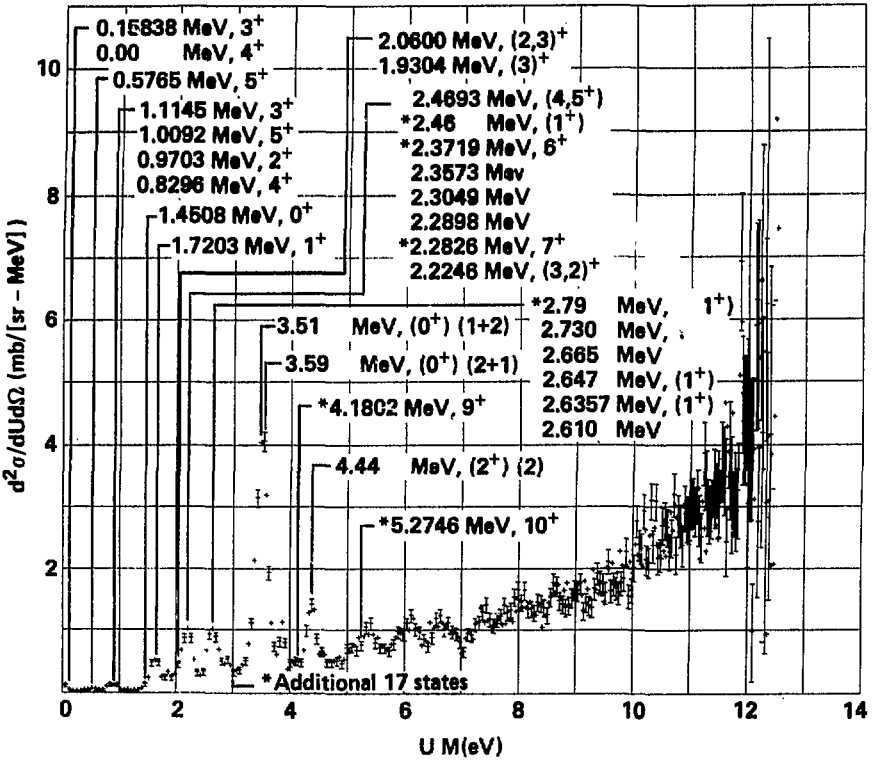

States are from Lederer and Shirley, Table of Isotopes, Seventh Edition, 1978.
States labelled with an asterisk are not listed as being populated by ^{56}Fe (p,n) or ^{56}Fe (p,nγ) in Lederer and Shirley.
Locations of states are approximate.

Figure 31

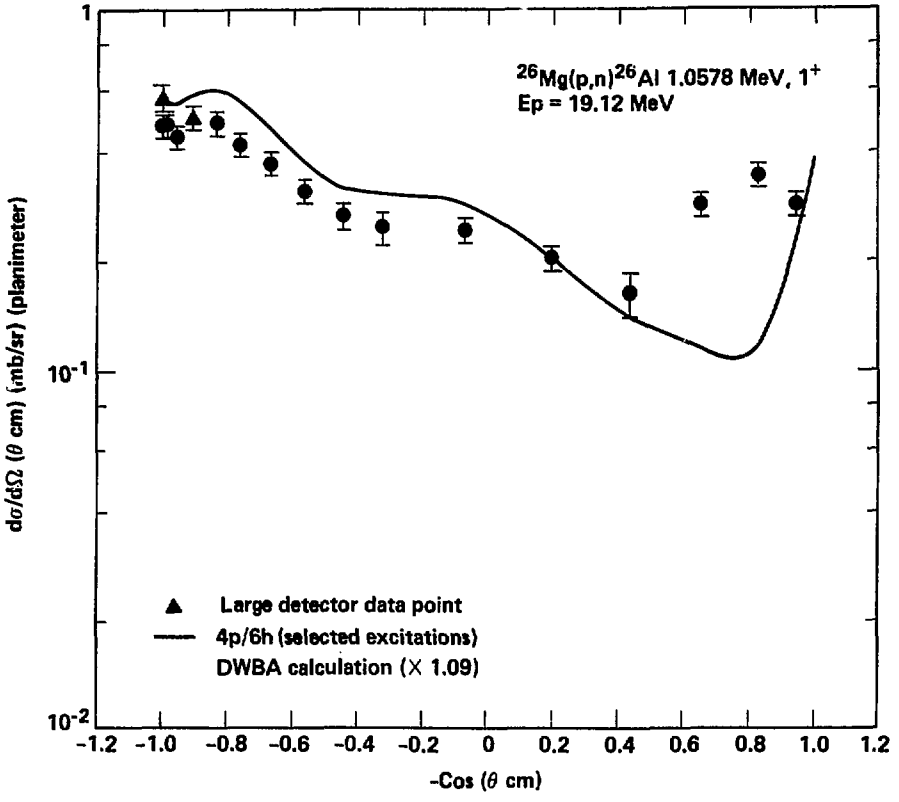

Differential Cross Sections

-Cos (θ cm)	dσ/dΩ (θ cm) (mb/sr)	Error of dσ/dΩ (θ cm) (mb/sr)
-1.00E+00	5.72E-01	5.0E-02
-9.98E-01	4.76E-01	3.6E-02
-9.86E-01	4.78E-01	3.6E-02
-9.54E-01	4.43E-01	3.3E-02
-9.07E-01	5.03E-01	3.8E-02
-8.32E-01	4.83E-01	3.6E-02
-7.62E-01	4.21E-01	3.2E-02
-6.66E-01	3.74E-01	2.8E-02
-5.61E-01	3.12E-01	2.3E-02
-4.42E-01	2.66E-01	2.3E-02
-3.23E-01	2.46E-01	2.6E-02
-6.89E-02	2.42E-01	1.9E-02
1.97E-01	2.02E-01	1.5E-02
4.33E-01	1.62E-01	2.1E-02
6.53E-01	2.83E-01	2.1E-02
8.24E-01	3.43E-01	2.6E-02
9.39E-01	2.84E-01	2.1E-02

DWBA σ_{total} = 3.27 mb Exp. σ_{total} = 3.58 ± 0.27 mb

Figure 32

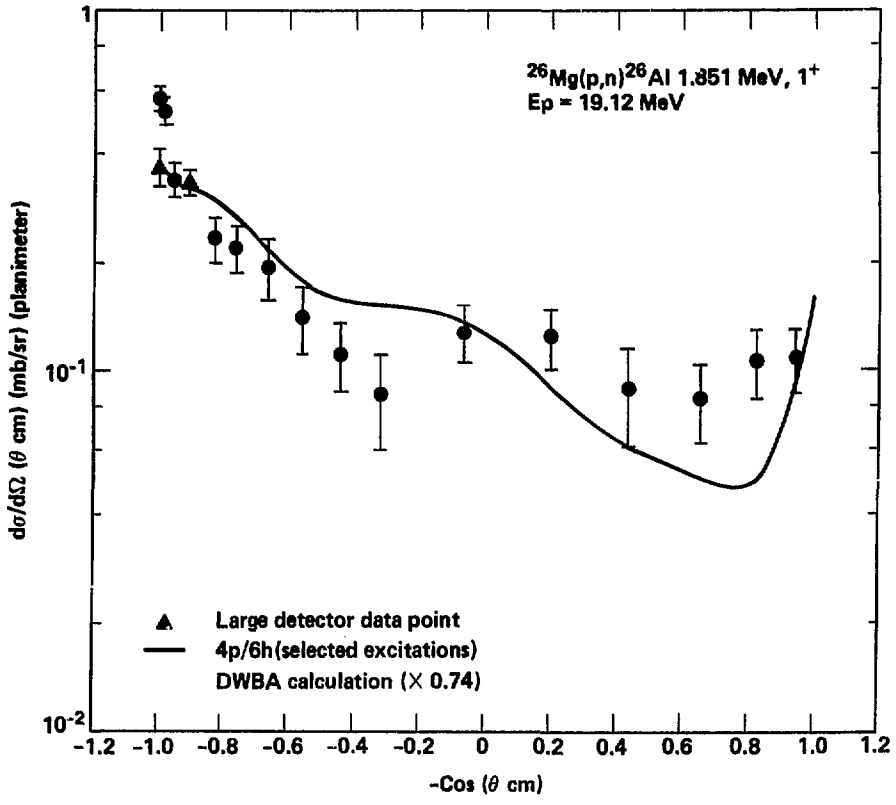

Differential Cross Sections

-Cos (θ cm)	dσ/dΩ (θ cm) (mb/sr)	Error of dσ/dΩ (θ cm) (mb/sr)
-1.00E+00	3.70E-01	4.3E-02
-9.98E-01	5.72E-01	4.6E-02
-9.86E-01	5.28E-01	4.5E-02
-9.54E-01	3.42E-01	3.8E-02
-9.07E-01	3.33E-01	2.5E-02
-8.31E-01	2.32E-01	3.4E-02
-7.61E-01	2.19E-01	3.2E-02
-6.65E-01	1.94E-01	3.8E-02
-5.60E-01	1.41E-01	2.9E-02
-4.41E-01	1.12E-01	2.4E-02
-3.21E-01	8.59E-02	2.5E-02
-6.74E-02	1.28E-01	2.3E-02
1.98E-01	1.24E-01	2.3E-02
4.34E-01	8.85E-02	2.7E-02
6.54E-01	8.32E-02	2.0E-02
8.24E-01	1.06E-01	2.3E-02
9.40E-01	1.00E-01	2.2E-02

DWBA σ_{total} = 2.36 mb Exp. σ_{total} = 1.74 ± 0.13 mb

Figure 33

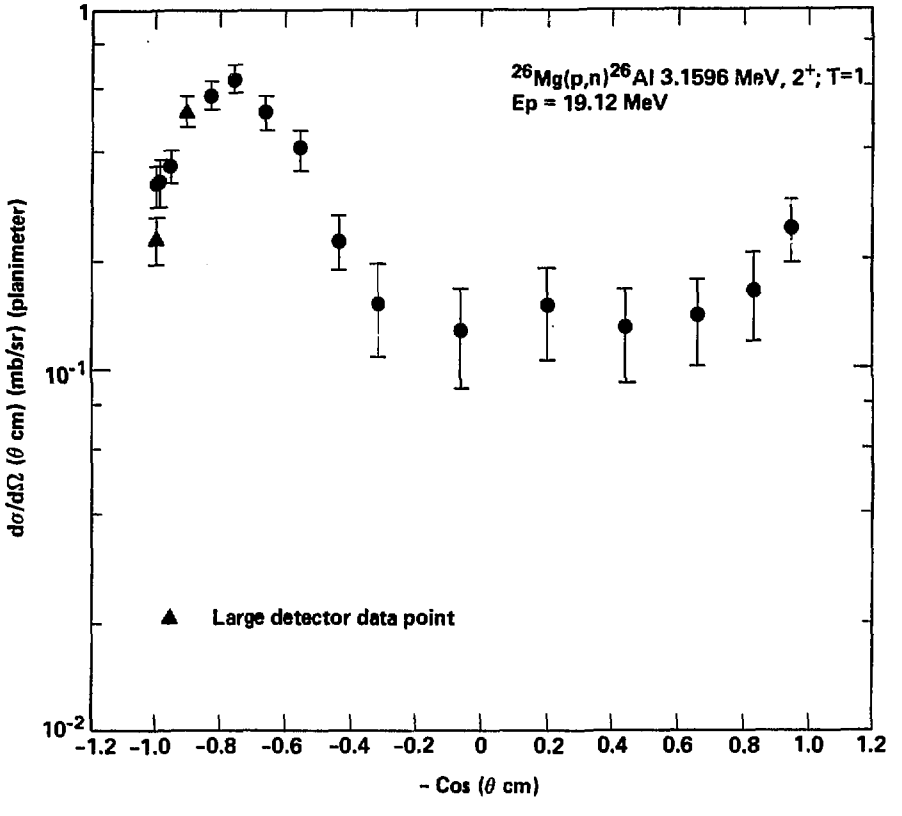

Differential Cross Sections

-Cos (θ cm)	dσ/dΩ (θ cm) (mb/sr)	Error of dσ/dΩ (θ cm) (mb/sr)
-1.ØØE+ØØ	2.29E-Ø1	3.4E-Ø2
-9.98E-Ø1	3.22E-Ø1	4.1E-Ø2
-9.86E-Ø1	3.29E-Ø1	4.8E-Ø2
-9.Ø7E-Ø1	5.17E-Ø1	5.ØE-Ø2
-9.54E-Ø1	3.63E-Ø1	3.9E-Ø2
-8.3ØE-Ø1	5.72E-Ø1	5.1E-Ø2
-7.6ØE-Ø1	6.35E-Ø1	5.6E-Ø2
-6.64E-Ø1	5.1ØE-Ø1	5.5E-Ø2
-5.58E-Ø1	4.ØØE-Ø1	5.1E-Ø2
-4.39E-Ø1	2.27E-Ø1	3.9E-Ø2
-3.19E-Ø1	1.52E-Ø1	4.4E-Ø2
-6.45E-Ø2	1.28E-Ø1	4.ØE-Ø2
2.Ø1E-Ø1	1.48E-Ø1	4.3E-Ø2
4.37E-Ø1	1.29E-Ø1	3.7E-Ø2
6.56E-Ø1	1.39E-Ø1	3.8E-Ø2
8.25E-Ø1	1.64E-Ø1	4.5E-Ø2
9.4ØE-Ø1	2.44E-Ø1	4.8E-Ø2

Exp. σ_{total} = 2.99 ± 0.22 mb

Figure 34

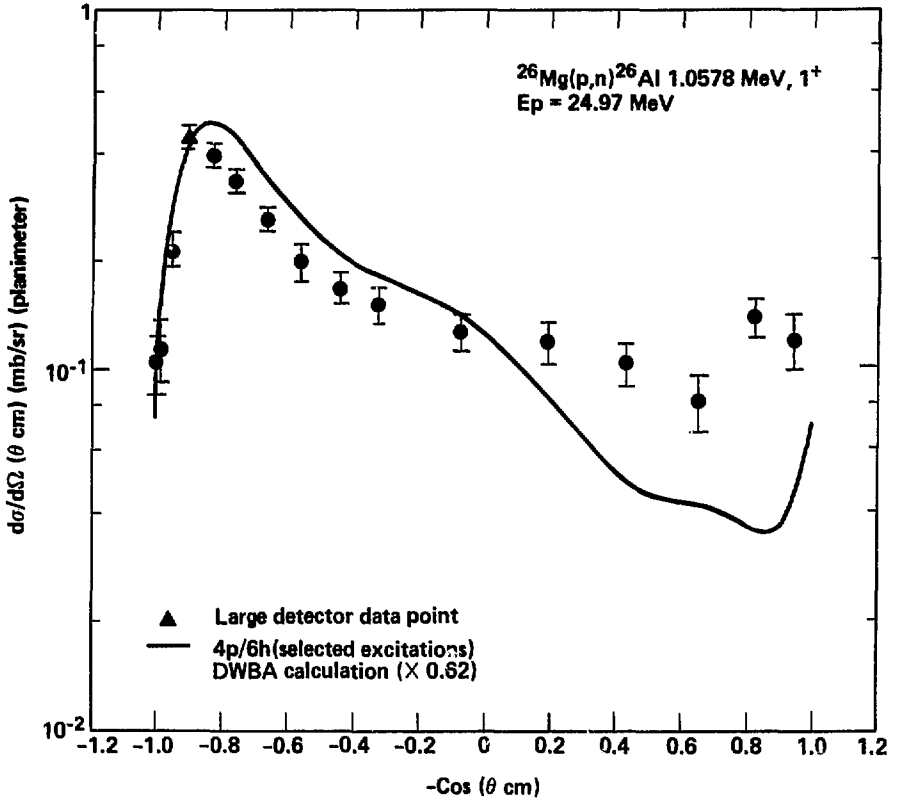

Differential Cross Sections

-Cos (θ cm)	dσ/dΩ (θ cm) (mb/sr)	Error of dσ/dΩ (θ cm) (mb/sr)
-9.98E-01	1.05E-01	1.9E-02
-9.86E-01	1.15E-01	2.2E-02
-9.54E-01	2.16E-01	2.3E-02
-9.08E-01	4.45E-01	3.3E-02
-8.32E-01	3.94E-01	3.0E-02
-7.63E-01	3.35E-01	2.5E-02
-6.67E-01	2.60E-01	1.9E-02
-5.63E-01	1.98E-01	2.3E-02
-4.44E-01	1.68E-01	1.7E-02
-3.25E-01	1.51E-01	1.7E-02
-7.12E-02	1.27E-01	1.4E-02
1.94E-01	1.18E-01	1.5E-02
4.31E-01	1.03E-01	1.4E-02
6.52E-01	8.09E-02	1.4E-02
8.23E-01	1.38E-01	1.6E-02
9.39E-01	1.19E-01	2.1E-02

DWBA σ_{total} = 3.28 mb Exp. σ_{total} = 2.04 ± 0.17 mb

Figure 35

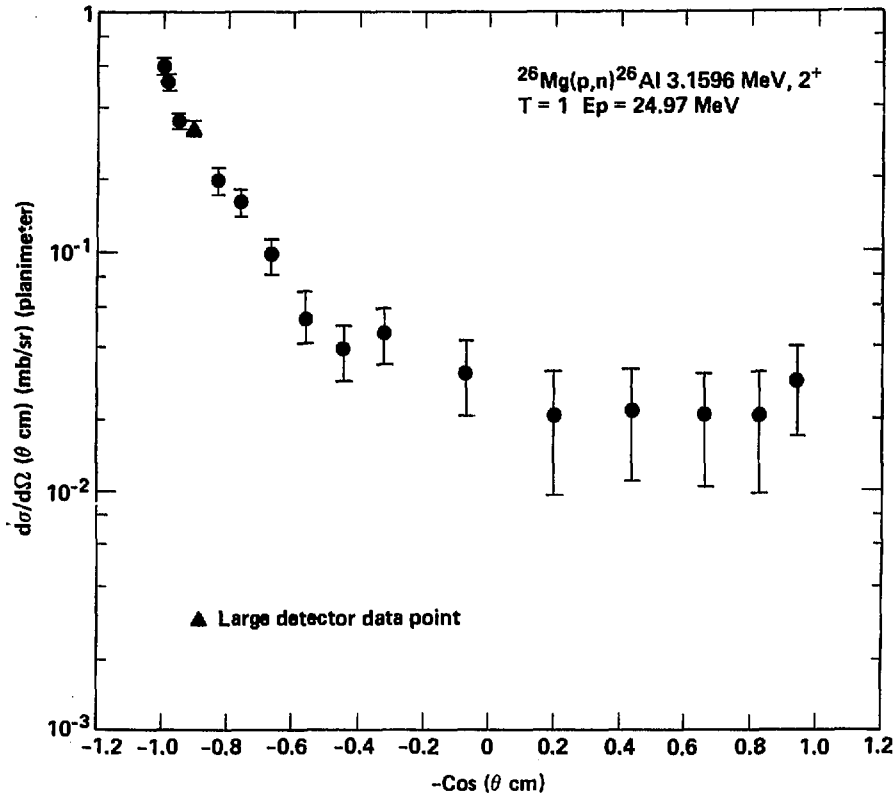

Differential Cross Sections

-Cos (θ cm)	dσ/dΩ (θ cm) (mb/sr)	Error of dσ/dΩ (θ cm) (mb/sr)
-9.98E-Ø1	5.99E-Ø1	4.2E-Ø2
-9.86E-Ø1	5.12E-Ø1	3.8E-Ø2
-9.54E-Ø1	3.51E-Ø1	2.6E-Ø2
-9.Ø7E-Ø1	3.26E-Ø1	2.5E-Ø2
-8.32E-Ø1	1.96E-Ø1	2.4E-Ø2
-7.62E-Ø1	1.6ØE-Ø1	2.1E-Ø2
-6.66E-Ø1	9.66E-Ø2	1.6E-Ø2
-5.61E-Ø1	5.52E-Ø2	1.3E-Ø2
-4.42E-Ø1	3.94E-Ø2	1.ØE-Ø2
-3.22E-Ø1	4.64E-Ø2	1.2E-Ø2
-6.84E-Ø2	3.16E-Ø2	1.1E-Ø2
1.97E-Ø1	2.Ø7E-Ø2	1.1E-Ø2
4.33E-Ø1	2.17E-Ø2	1.1E-Ø2
6.53E-Ø1	2.Ø7E-Ø2	1.ØE-Ø2
8.24E-Ø1	2.Ø7E-Ø2	1.1E-Ø2
9.4ØE-Ø1	2.86E-Ø2	1.2E-Ø2

Exp. σ_{total} = 0.84 ± 0.07 mb

Figure 36

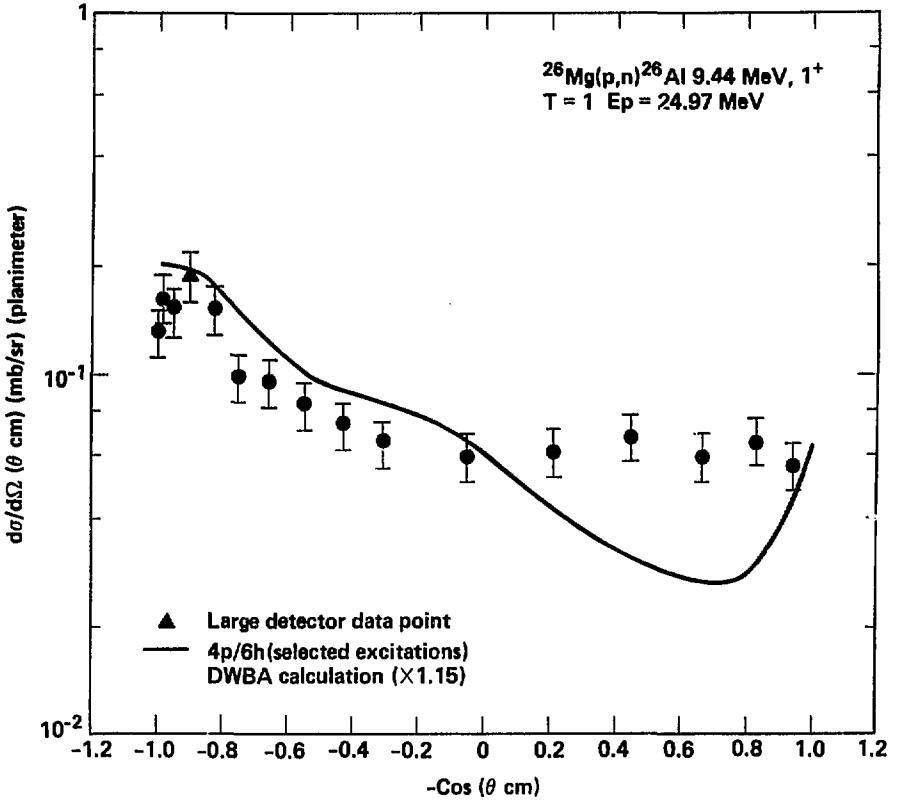

Differential Cross Sections

-Cos (θ cm)	dσ/dΩ (θ cm) (mb/sr)	Error of dσ/dΩ (θ cm) (mb/sr)
-9.98E-Ø1	1.32E-Ø1	2.ØE-Ø2
-9.86E-Ø1	1.64E-Ø1	2.5E-Ø2
-9.53E-Ø1	1.5ØE-Ø1	2.3E-Ø2
-9.Ø5E-Ø1	1.88E-Ø1	2.8E-Ø2
-8.28E-Ø1	1.52E-Ø1	2.3E-Ø2
-7.56E-Ø1	9.92E-Ø2	1.5E-Ø2
-6.59E-Ø1	9.59E-Ø2	1.4E-Ø2
-5.52E-Ø1	8.27E-Ø2	1.2E-Ø2
-4.32E-Ø1	7.28E-Ø2	1.1E-Ø2
-3.1ØE-Ø1	6.45E-Ø2	9.7E-Ø3
-5.53E-Ø2	5.95E-Ø2	8.9E-Ø3
2.1ØE-Ø1	6.12E-Ø2	9.2E-Ø3
4.44E-Ø1	6.78E-Ø2	1.ØE-Ø2
6.61E-Ø1	5.95E-Ø2	8.9E-Ø3
8.28E-Ø1	6.61E-Ø2	9.9E-Ø3
9.41E-Ø1	5.62E-Ø2	8.4E-Ø3

DWBA σ_{total} = 0.84 mb Exp. σ_{total} = 0.96 ± 0.07 mb

Figure 37

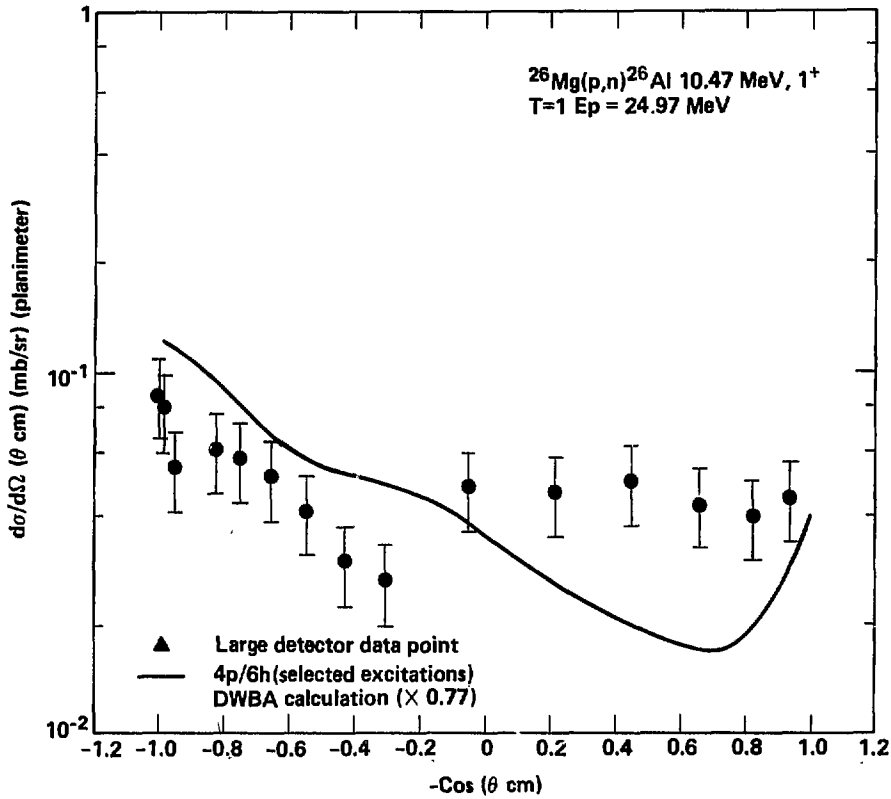

Differential Cross Sections

-Cos (θ cm)	dσ/dΩ (θ cm) (mb/sr)	Error of dσ/dΩ (θ cm) (mb/sr)
-9.98E-Ø1	8.76E-Ø2	2.2E-Ø2
-9.86E-Ø1	7.94E-Ø2	2.ØE-Ø2
-9.52E-Ø1	5.46E-Ø2	1.4E-Ø2
-8.27E-Ø1	6.12E-Ø2	1.5E-Ø2
-7.55E-Ø1	5.79E-Ø2	1.5E-Ø2
-6.57E-Ø1	5.13E-Ø2	1.3E-Ø2
-5.5ØE-Ø1	4.13E-Ø2	1.ØE-Ø2
-4.29E-Ø1	2.98E-Ø2	7.4E-Ø3
-3.Ø7E-Ø1	2.65E-Ø2	6.6E-Ø3
-5.19E-Ø2	4.79E-Ø2	1.2E-Ø2
2.13E-Ø1	4.63E-Ø2	1.2E-Ø2
4.47E-Ø1	4.96E-Ø2	1.2E-Ø2
6.63E-Ø1	4.3ØE-Ø2	1.1E-Ø2
8.3ØE-Ø1	3.97E-Ø2	9.9E-Ø3
9.42E-Ø1	4.46E-Ø2	1.1E-Ø2

DWBA σ_{total} = 0.73 mb Exp. σ_{total} = 0.56 ± 0.05 mb

Figure 38

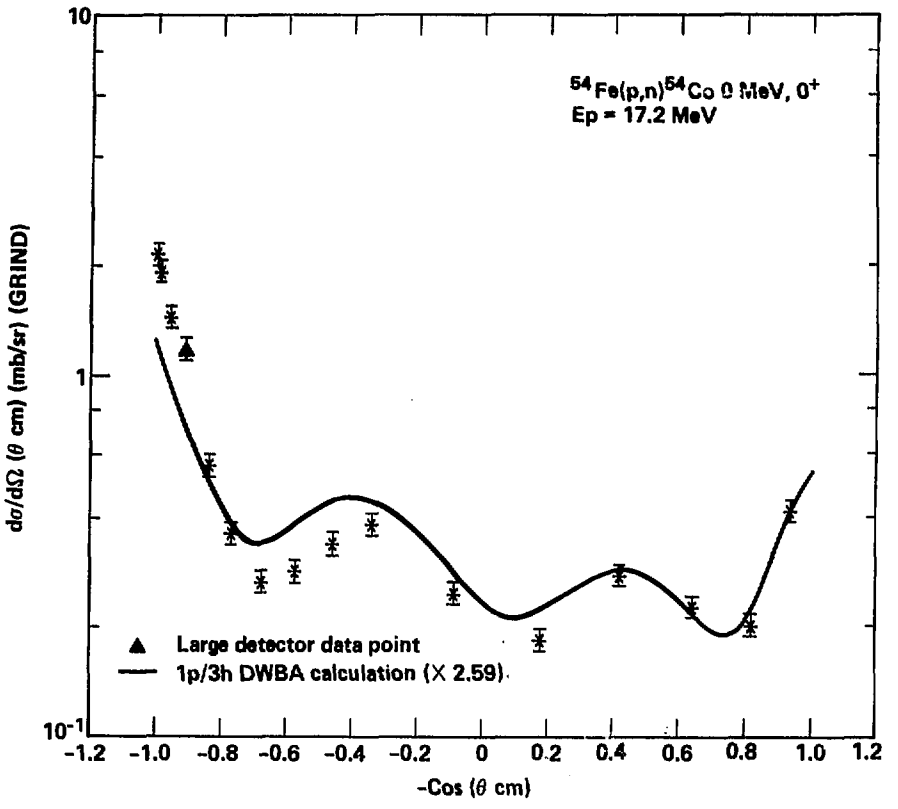

Differential Cross Sections

-Cos (θ cm)	dσ/dΩ (θ cm) (mb/sr)	Error of dσ/dΩ (θ cm) (mb/sr)
-9.98E-01	2.15E+00	1.5E-01
-9.86E-01	1.94E+00	1.4E-01
-9.56E-01	1.45E+00	1.0E-01
-9.11E-01	1.19E+00	8.3E-02
-8.37E-01	5.61E-01	3.9E-02
-7.70E-01	3.63E-01	2.5E-02
-6.77E-01	2.67E-01	1.9E-02
-5.74E-01	2.87E-01	2.0E-02
-4.58E-01	3.43E-01	2.4E-02
-3.40E-01	3.85E-01	2.7E-02
-8.81E-02	2.48E-01	1.7E-02
1.78E-01	1.84E-01	1.3E-02
4.17E-01	2.78E-01	1.9E-02
6.42E-01	2.27E-01	1.6E-02
8.17E-01	2.02E-01	1.4E-02
9.37E-01	4.18E-01	2.9E-02

DWBA σ_{total} = 1.74 mb Exp. σ_{total} = 4.50 ± 0.73 mb

Figure 39

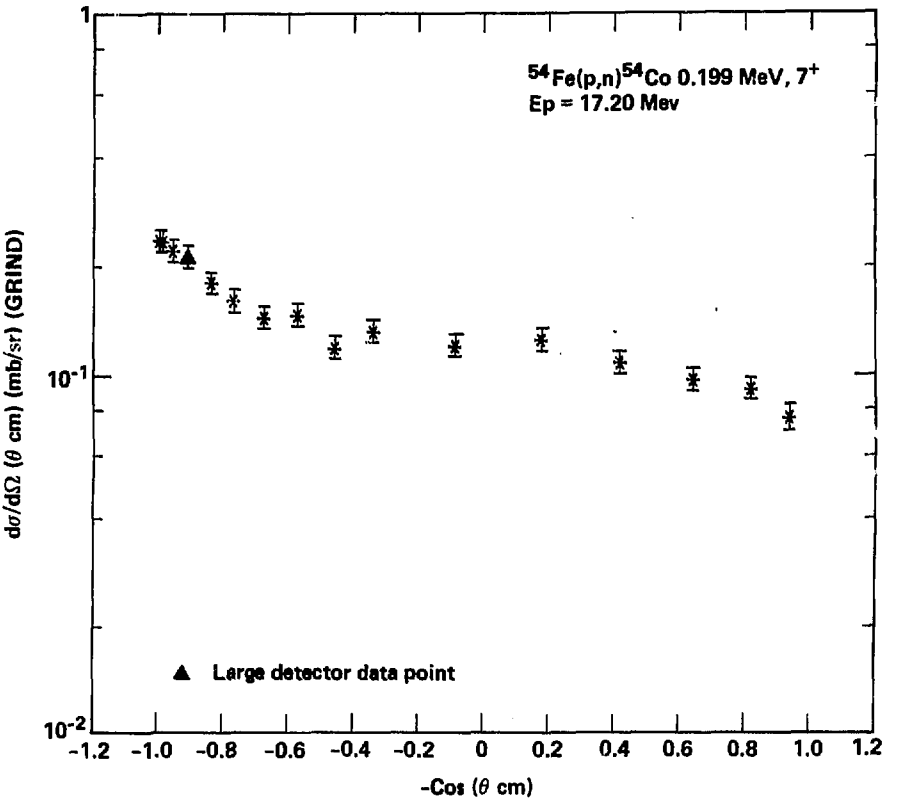

Differential Cross Sections

-Cos (θ cm)	dσ/dΩ (θ cm) (mb/sr)	Error of dσ/dΩ (θ cm) (mb/sr)
-9.98E-Ø1	2.35E-Ø1	1.6E-Ø2
-9.86E-Ø1	2.35E-Ø1	1.6E-Ø2
-9.56E-Ø1	2.21E-Ø1	1.6E-Ø2
-9.1ØE-Ø1	2.14E-Ø1	1.5E-Ø2
-8.37E-Ø1	1.81E-Ø1	1.3E-Ø2
-7.7ØE-Ø1	1.61E-Ø1	1.1E-Ø2
-6.76E-Ø1	1.45E-Ø1	1.ØE-Ø2
-5.74E-Ø1	1.48E-Ø1	1.ØE-Ø2
-4.57E-Ø1	1.2ØE-Ø1	8.4E-Ø3
-3.39E-Ø1	1.33E-Ø1	9.3E-Ø3
-8.78E-Ø2	1.22E-Ø1	8.5E-Ø3
1.78E-Ø1	1.26E-Ø1	9.8E-Ø3
4.17E-Ø1	1.Ø9E-Ø1	7.6E-Ø3
6.42E-Ø1	9.76E-Ø2	6.8E-Ø3
8.17E-Ø1	9.21E-Ø2	6.4E-Ø3
9.37E-Ø1	7.66E-Ø2	6.5E-Ø3

Exp. σ_{total} = 1.59 ± 0.12 mb

Figure 40

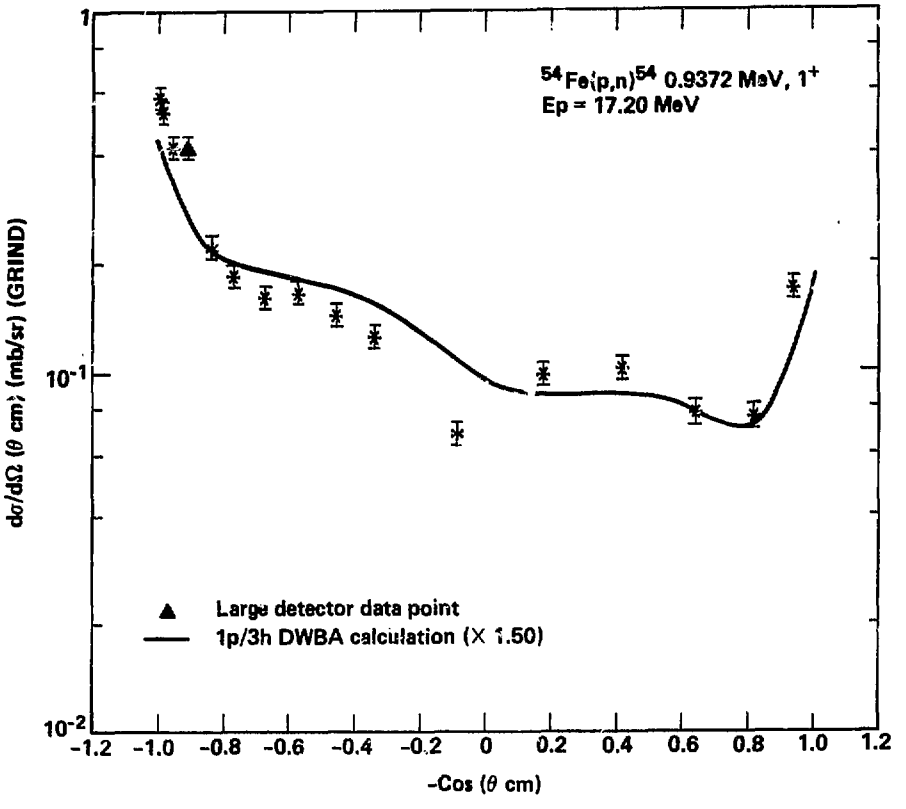

-Cos (θ cm)	Differential Cross Sections dσ/dΩ (θ cm) (mb/sr)	Error of dσ/dΩ (θ cm) (mb/sr)
-9.98E-01	5.76E-01	4.0E-02
-9.86E-01	5.25E-01	3.7E-02
-9.55E-01	4.20E-01	2.9E-02
-9.10E-01	4.18E-01	2.9E-02
-8.37E-01	2.22E-01	1.6E-02
-7.69E-01	1.83E-01	1.3E-02
-6.76E-01	1.61E-01	1.1E-02
-5.73E-01	1.66E-01	1.2E-02
-4.56E-01	1.43E-01	1.0E-02
-3.38E-01	1.25E-01	8.8E-03
-8.63E-02	6.90E-02	4.8E-03
1.79E-01	9.83E-02	6.9E-03
4.13E-01	1.02E-01	7.1E-03
6.43E-01	7.71E-02	6.0E-03
8.18E-01	7.50E-02	5.6E-03
9.37E-01	1.69E-01	1.2E-02

DWBA σ_{total} = 1.13 mb Exp. σ_{total} = 1.70 ± 0.13 mb

Figure 41

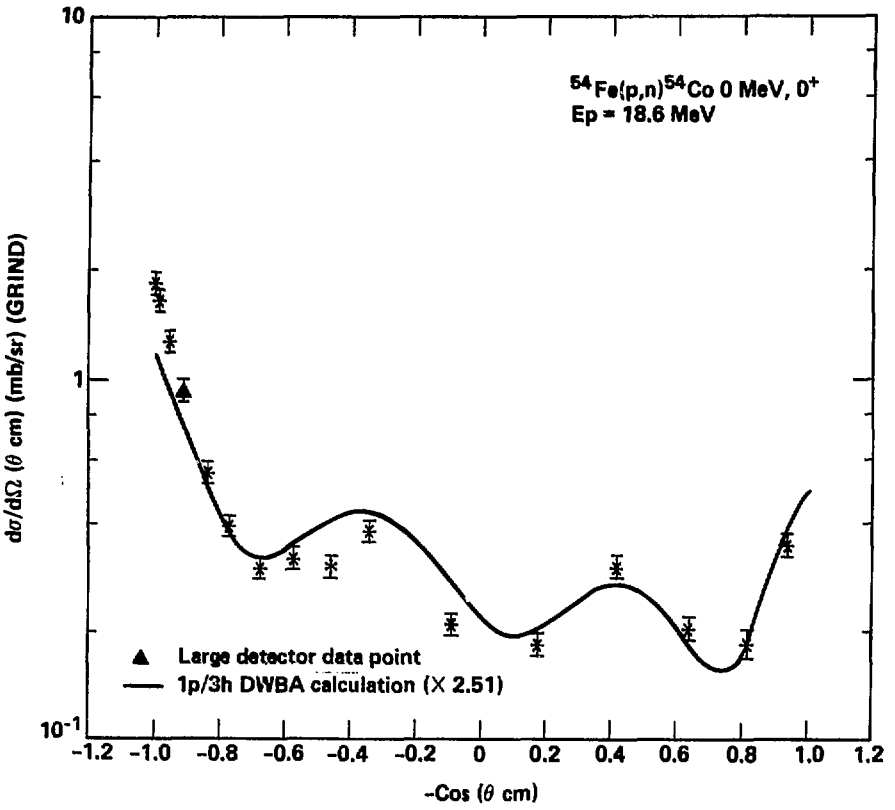

Differential Cross Sections

-Cos (θ cm)	dσ/dΩ (θ cm) (mb/sr)	Error of dσ/dΩ (θ cm) (mb/sr)
-9.98E-Ø1	1.84E+ØØ	1.3E-Ø1
-9.87E-Ø1	1.66E+ØØ	1.2E-Ø1
-9.56E-Ø1	1.28E+ØØ	8.9E-Ø2
-9.11E-Ø1	9.35E-Ø1	6.5E-Ø2
-8.38E-Ø1	5.56E-Ø1	3.9E-Ø2
-7.7ØE-Ø1	3.96E-Ø1	2.8E-Ø2
-6.77E-Ø1	3.Ø3E-Ø1	2.1E-Ø2
-5.75E-Ø1	3.22E-Ø1	2.3E-Ø2
-4.59E-Ø1	3.Ø4E-Ø1	2.1E-Ø2
-3.41E-Ø1	3.82E-Ø1	2.7E-Ø2
-8.92E-Ø2	2.1ØE-Ø1	1.5E-Ø2
1.77E-Ø1	1.84E-Ø1	1.3E-Ø2
4.16E-Ø1	3.Ø4E-Ø1	2.1E-Ø2
6.41E-Ø1	2.Ø4E-Ø1	1.4E-Ø2
8.17E-Ø1	1.85E-Ø1	1.7E-Ø2
9.37E-Ø1	3.49E-Ø1	2.4E-Ø2

DWEA σ_{total} = 1.67 mb Exp. σ_{total} = 4.19 ± 0.31 mb

Figure 42

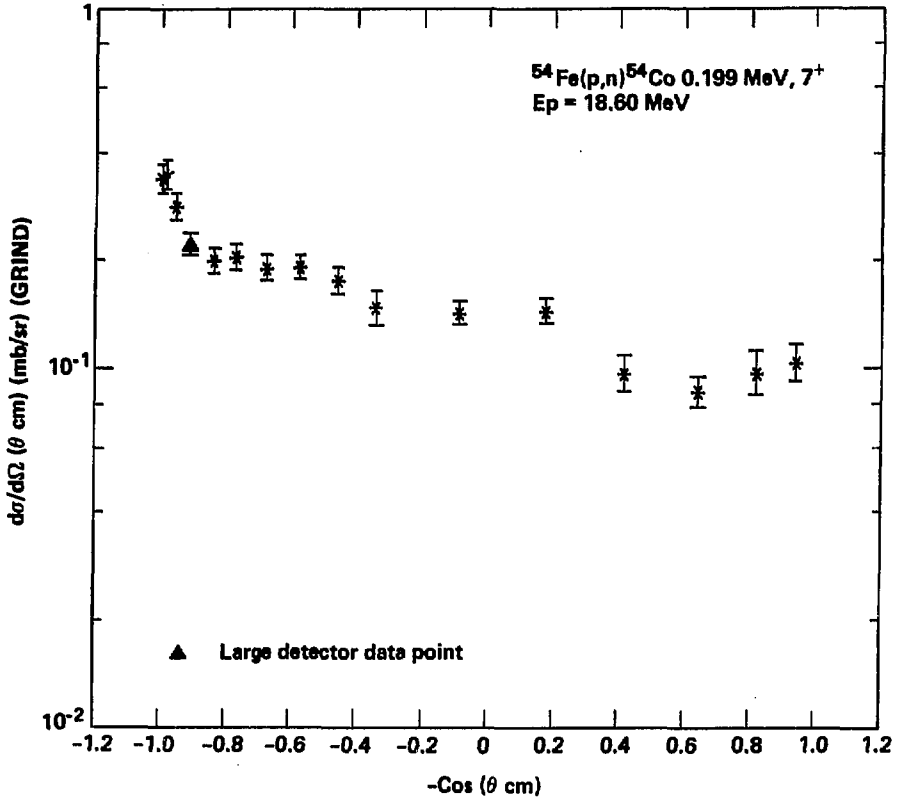

Differential Cross Sections

-Cos (θ cm)	dσ/dΩ (θ cm) (mb/sr)	Error of dσ/dΩ (θ cm) (mb/sr)
-9.98E-01	3.39E-01	3.3E-02
-9.87E-01	3.48E-01	3.4E-02
-9.56E-01	2.82E-01	2.4E-02
-9.11E-01	2.21E-01	1.5E-02
-8.38E-01	1.98E-01	1.6E-02
-7.78E-01	2.03E-01	1.7E-02
-6.77E-01	1.91E-01	1.6E-02
-5.75E-01	1.91E-01	1.4E-02
-4.50E-01	1.75E-01	1.5E-02
-3.48E-01	1.47E-01	1.6E-02
-8.89E-02	1.42E-01	1.8E-02
1.77E-01	1.44E-01	1.1E-02
4.16E-01	9.73E-02	1.1E-02
6.41E-01	8.64E-02	7.8E-03
8.17E-01	9.79E-02	1.3E-02
9.37E-01	1.04E-01	1.2E-02

Exp. σ_{total} = 1.82 ± 0.14 mb

Figure 43

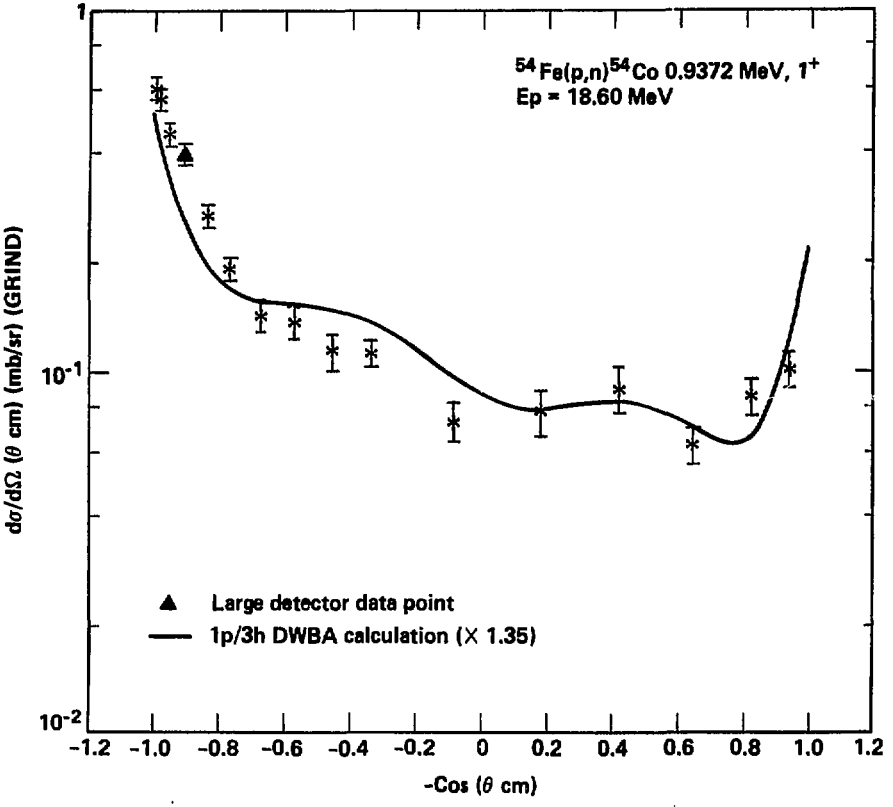

Differential Cross Sections

-Cos (θ cm)	dσ/dΩ (θ cm) (mb/sr)	Error of dσ/dΩ (θ cm) (mb/sr)
-9.98E-01	6.87E-01	4.3E-02
-9.86E-01	5.64E-01	4.0E-02
-9.56E-01	4.53E-01	3.2E-02
-9.10E-01	4.00E-01	2.8E-02
-8.37E-01	2.71E-01	2.0E-02
-7.70E-01	1.93E-01	1.4E-02
-6.76E-01	1.44E-01	1.5E-02
-5.74E-01	1.38E-01	1.4E-02
-4.57E-01	1.14E-01	1.3E-02
-3.39E-01	1.13E-01	9.2E-03
-8.78E-02	7.31E-02	9.0E-03
1.78E-01	7.77E-02	1.1E-02
4.17E-01	8.94E-02	1.3E-02
6.42E-01	6.28E-02	7.7E-03
8.17E-01	8.54E-02	1.0E-02
9.37E-01	1.02E-01	1.1E-02

DWBA σ_{total} = 1.16 mb Exp. σ_{total} = 1.56 ± 0.12 mb

Figure 44

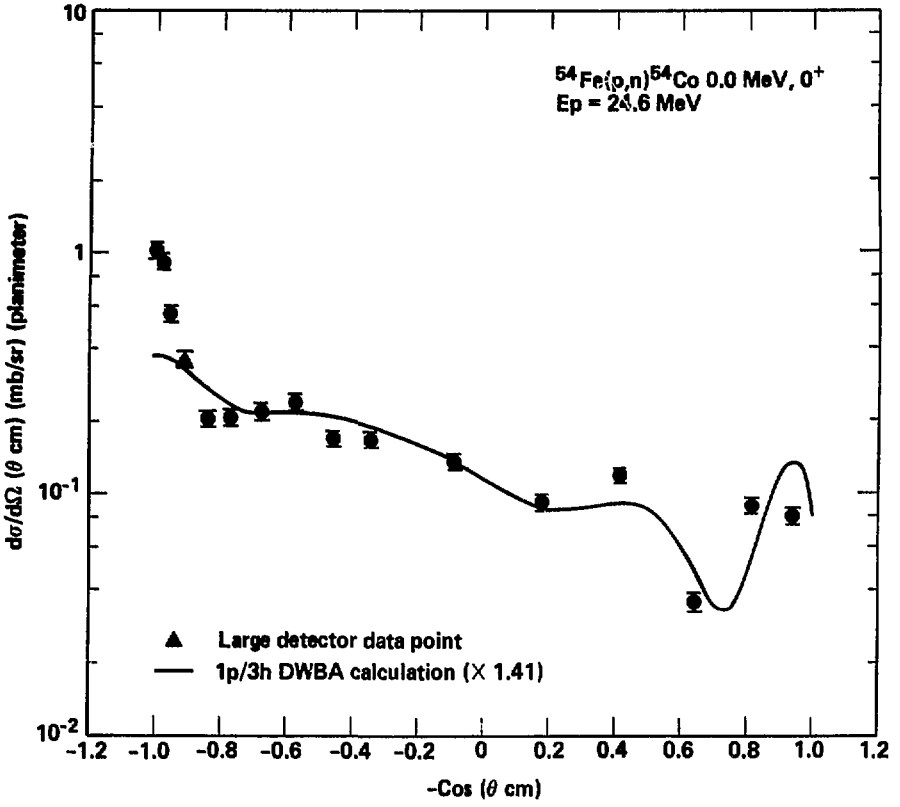

Differential Cross Sections

-Cos (θ cm)	dσ/dΩ (θ cm) (mb/sr)	Error of dσ/dΩ (θ cm) (mb/sr)
-9.98E-Ø1	1.ØØE+ØØ	7.7E-Ø2
-9.87E-Ø1	9.18E-Ø1	6.9E-Ø2
-9.56E-Ø1	5.59E-Ø1	4.2E-Ø2
-9.11E-Ø1	3.63E-Ø1	2.7E-Ø2
-8.59E-Ø1	2.Ø5E-Ø1	1.5E-Ø2
-7.71E-Ø1	2.Ø7E-Ø1	1.6E-Ø2
-6.79E-Ø1	2.18E-Ø1	1.7E-Ø2
-5.77E-Ø1	2.38E-Ø1	1.8E-Ø2
-4.61E-Ø1	1.69E-Ø1	1.3E-Ø2
-3.43E-Ø1	1.68E-Ø1	1.3E-Ø2
-9.18E-Ø2	1.36E-Ø1	1.ØE-Ø2
1.74E-Ø1	9.17E-Ø2	6.9E-Ø3
4.14E-Ø1	1.18E-Ø1	8.9E-Ø3
6.39E-Ø1	3.57E-Ø2	3.3E-Ø3
8.16E-Ø1	8.9ØE-Ø2	6.7E-Ø3
9.37E-Ø1	8.Ø2E-Ø2	6.ØE-Ø3

DWBA σ_{total} = 1.32 mb Exp. σ_{total} = 1.87 ± 0.14 mb

Figure 45

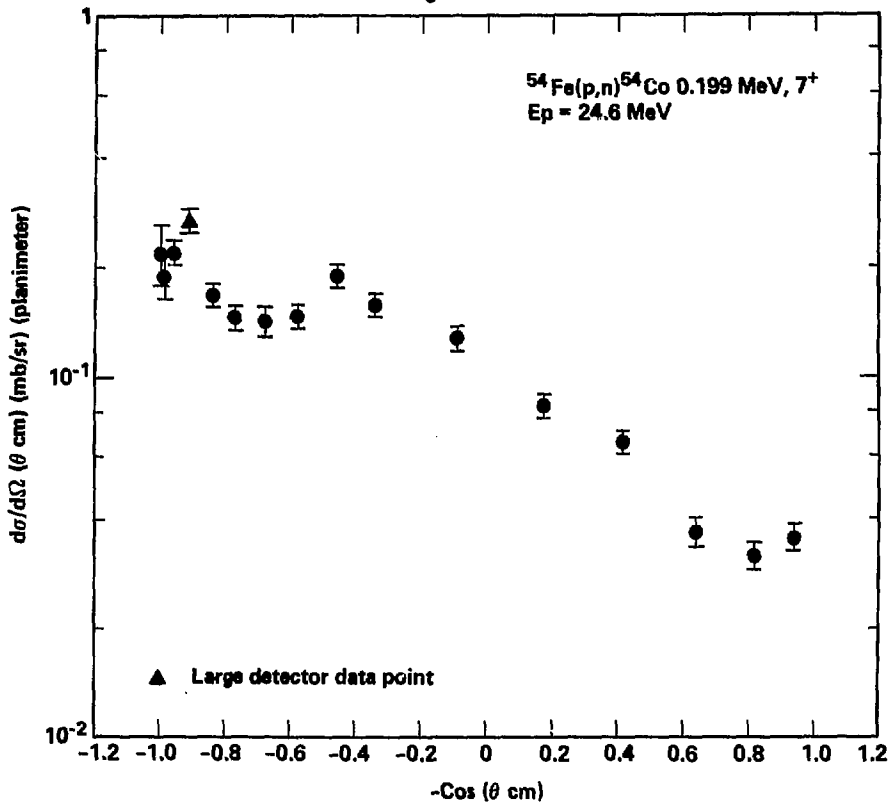

Differential Cross Sections

-Cos (θ cm)	dσ/dΩ (θ cm) (mb/sr)	Error of dσ/dΩ (θ cm) (mb/sr)
-9.98E-01	2.20E-01	4.1E-02
-9.87E-01	1.90E-01	2.6E-02
-9.56E-01	2.20E-01	1.7E-02
-9.11E-01	2.70E-01	2.0E-02
-8.38E-01	1.68E-01	1.3E-02
-7.71E-01	1.45E-01	1.1E-02
-6.78E-01	1.42E-01	1.4E-02
-5.77E-01	1.46E-01	1.1E-02
-4.60E-01	1.89E-01	1.4E-02
-3.43E-01	1.57E-01	1.2E-02
-9.17E-02	1.27E-01	9.5E-03
1.74E-01	8.30E-02	6.2E-03
4.14E-01	6.59E-02	4.9E-03
6.39E-01	3.72E-02	3.4E-03
8.16E-01	3.20E-02	2.9E-03
9.37E-01	3.60E-02	3.0E-03

Exp. σ_{total} = 1.36 ± 0.10 mb

Figure 46

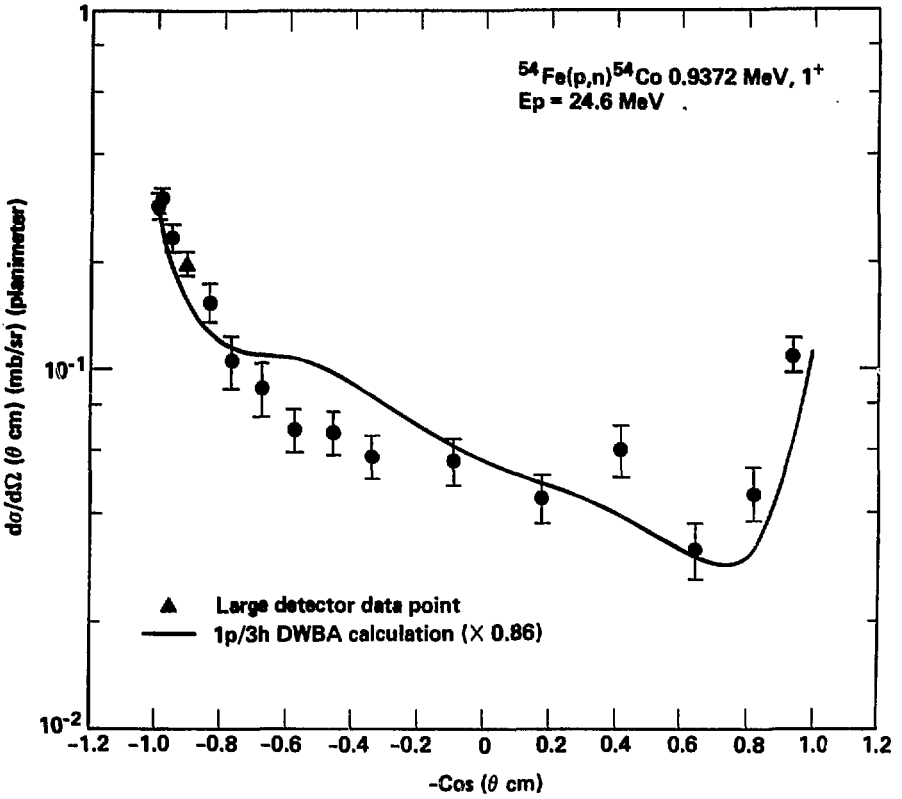

Differential Cross Sections

-Cos (θ cm)	dσ/dΩ (θ cm) (mb/sr)	Error of dσ/dΩ (θ cm) (mb/sr)
-9.98E-Ø1	2.85E-Ø1	2.3E-Ø2
-9.87E-Ø1	2.96E-Ø1	2.5E-Ø2
-9.56E-Ø1	2.33E-Ø1	2.1E-Ø2
-9.11E-Ø1	1.98E-Ø1	1.5E-Ø2
-8.38E-Ø1	1.54E-Ø1	1.8E-Ø2
-7.71E-Ø1	1.Ø6E-Ø1	1.7E-Ø2
-6.78E-Ø1	8.93E-Ø2	1.5E-Ø2
-5.76E-Ø1	6.86E-Ø2	9.6E-Ø3
-4.6ØE-Ø1	6.72E-Ø2	9.3E-Ø3
-3.42E-Ø1	5.8ØE-Ø2	8.2E-Ø3
-9.11E-Ø2	5.62E-Ø2	8.5E-Ø3
1.75E-Ø1	4.42E-Ø2	6.7E-Ø3
4.14E-Ø1	6.Ø3E-Ø2	9.9E-Ø3
6.4ØE-Ø1	3.18E-Ø2	5.5E-Ø3
8.16E-Ø1	4.56E-Ø2	7.7E-Ø3
9.37E-Ø1	1.1ØE-Ø1	1.2E-Ø2

DWBA σ_{total} = 1.07 mb Exp. σ_{total} = 0.92 ± 0.069 mb

Figure 47

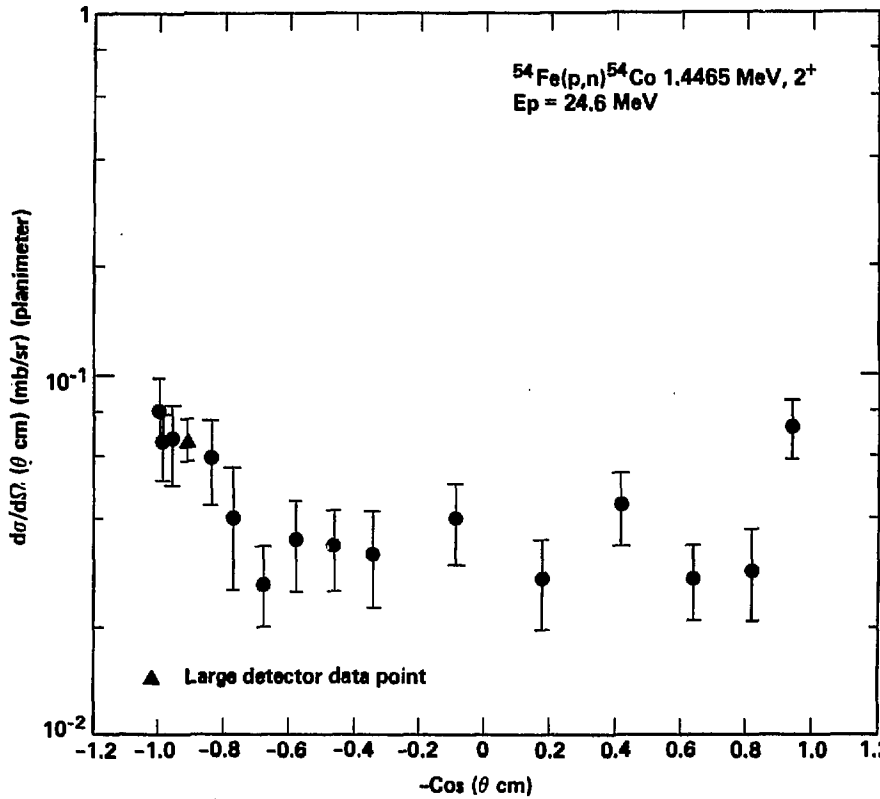

Differential Cross Sections

-Cos (θ cm)	dσ/dΩ (θ cm) (mb/sr)	Error of dσ/dΩ (θ cm) (mb/sr)
-9.98E-Ø1	8.13E-Ø2	1.7E-Ø2
-9.87E-Ø1	6.6ØE-Ø2	1.5E-Ø2
-9.56E-Ø1	6.67E-Ø2	1.7E-Ø2
-9.11E-Ø1	6.72E-Ø2	9.1E-Ø3
-8.38E-Ø1	5.94E-Ø2	1.6E-Ø2
-7.71E-Ø1	4.Ø5E-Ø2	1.5E-Ø2
-6.78E-Ø1	2.67E-Ø2	6.8E-Ø3
-5.76E-Ø1	3.5ØE-Ø2	1.ØE-Ø2
-4.6ØE-Ø1	3.36E-Ø2	8.6E-Ø3
-3.42E-Ø1	3.22E-Ø2	9.7E-Ø3
-9.Ø6E-Ø2	4.ØØE-Ø2	1.ØE-Ø2
1.75E-Ø1	2.72E-Ø2	7.8E-Ø3
4.15E-Ø1	4.37E-Ø2	1.ØE-Ø2
6.4ØE-Ø1	2.72E-Ø2	6.4E-Ø3
8.16E-Ø1	2.9ØE-Ø2	8.4E-Ø3
9.37E-Ø1	7.27E-Ø2	1.4E-Ø2

Exp. σ_{total} = 0.47 ± 0.036 mb

Figure 48

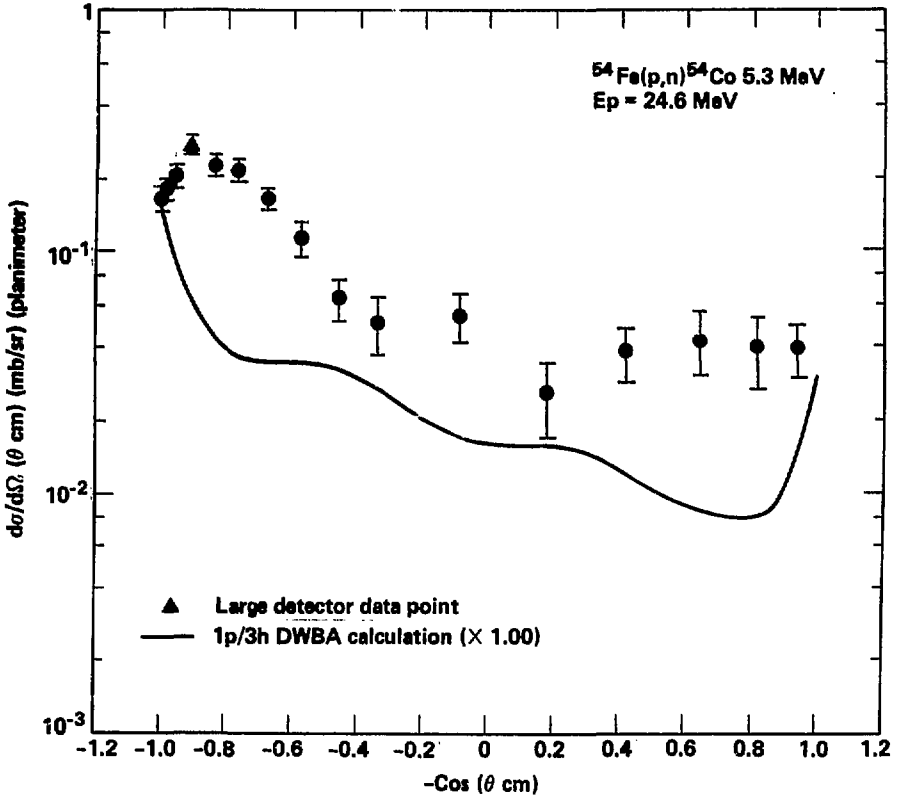

Differential Cross Sections

-Cos (θ cm)	dσ/dΩ (θ cm) (mb/sr)	Error of dσ/dΩ (θ cm) (mb/sr)
-9.98E-Ø1	1.67E-Ø1	2.ØE-Ø2
-9.86E-Ø1	1.82E-Ø1	1.8E-Ø2
-9.55E-Ø1	2.Ø6E-Ø1	2.1E-Ø2
-9.1ØE-Ø1	2.76E-Ø1	2.5E-Ø2
-8.37E-Ø1	2.28E-Ø1	2.3E-Ø2
-7.69E-Ø1	2.18E-Ø1	2.3E-Ø2
-6.76E-Ø1	1.67E-Ø1	1.7E-Ø2
-5.73E-Ø1	1.14E-Ø1	1.9E-Ø2
-4.56E-Ø1	6.41E-Ø2	1.3E-Ø2
-3.38E-Ø1	5.Ø8E-Ø2	1.4E-Ø2
-8.62E-Ø2	5.4ØE-Ø2	1.2E-Ø2
1.8ØE-Ø1	2.57E-Ø2	8.5E-Ø3
4.18E-Ø1	3.8ØE-Ø2	9.5E-Ø3
6.43E-Ø1	4.31E-Ø2	1.3E-Ø2
8.18E-Ø1	3.96E-Ø2	1.3E-Ø2
9.37E-Ø1	3.93E-Ø2	9.6E-Ø3

DWBA σ_{total} = 0.31 mb Exp. σ_{total} = 0.98 ± 0.074 mb

Figure 49

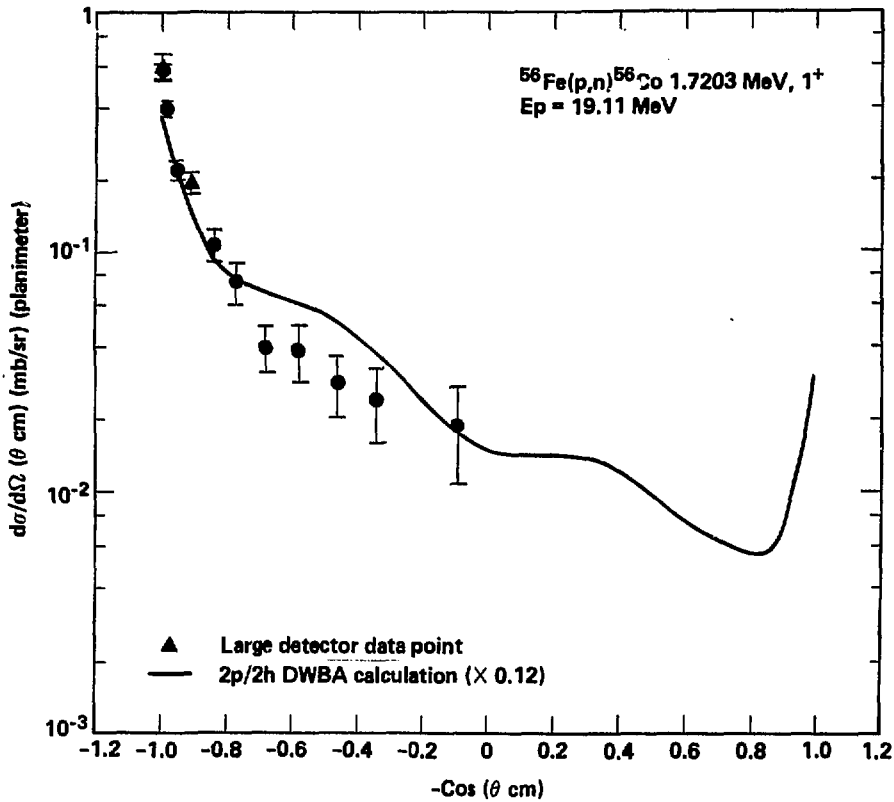

Differential Cross Sections

-Cos (θ cm)	dσ/dΩ (θ cm) (mb/sr)	Error of dσ/dΩ (θ cm) (mb/sr)
-1.ØØE+ØØ	6.Ø1E-Ø1	7.2E-Ø2
-9.98E-Ø1	5.05E-Ø1	4.2E-Ø2
-9.87E-Ø1	3.94E-Ø1	3.ØE-Ø2
-9.56E-Ø1	2.19E-Ø1	2.ØE-Ø2
-9.11E-Ø1	1.93E-Ø1	1.9E-Ø2
-8.39E-Ø1	1.Ø7E-Ø1	1.7E-Ø2
-7.72E-Ø1	7.45E-Ø2	1.5E-Ø2
-6.79E-Ø1	3.99E-Ø2	8.6E-Ø3
-5.77E-Ø1	3.88E-Ø2	1.ØE-Ø2
-4.61E-Ø1	2.83E-Ø2	8.ØE-Ø3
-3.44E-Ø1	2.41E-Ø2	8.2E-Ø3
-9.26E-Ø2	1.89E-Ø2	8.2E-Ø3

DWBA σ_{total} = 4.06 mb Exp. σ_{total} is not available

Figure 50

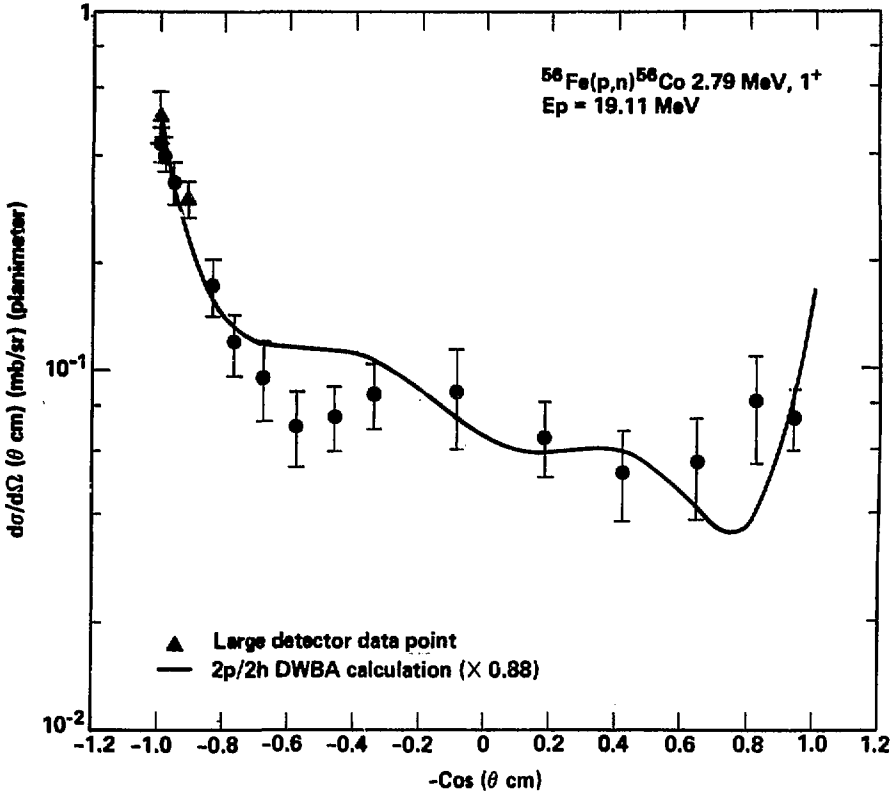

Differential Cross Sections

-Cos (θ cm)	dσ/dΩ (θ cm) (mb/sr)	Error of dσ/dΩ (θ cm) (mb/sr)
-1.ØØE+ØØ	5.12E-Ø1	8.2E-Ø2
-9.98E-Ø1	4.26E-Ø1	4.8E-Ø2
-9.87E-Ø1	3.99E-Ø1	4.4E-Ø2
-9.56E-Ø1	3.34E-Ø1	4.5E-Ø2
-9.11E-Ø1	2.99E-Ø1	3.3E-Ø2
-8.38E-Ø1	1.72E-Ø1	3.1E-Ø2
-7.71E-Ø1	1.19E-Ø1	2.3E-Ø2
-6.78E-Ø1	9.54E-Ø2	2.4E-Ø2
-5.77E-Ø1	7.Ø3E-Ø2	1.7E-Ø2
-4.6ØE-Ø1	7.45E-Ø2	1.6E-Ø2
-3.43E-Ø1	8.6ØE-Ø2	1.8E-Ø2
-9.15E-Ø2	8.7ØE-Ø2	2.7E-Ø2
1.74E-Ø1	6.61E-Ø2	1.6E-Ø2
4.14E-Ø1	5.24E-Ø2	1.5E-Ø2
6.4ØE-Ø1	5.56E-Ø2	1.8E-Ø2
8.16E-Ø1	8.18E-Ø2	2.7E-Ø2
9.37E-Ø1	7.34E-Ø2	1.4E-Ø2

DWBA σ_{total} = 1.35 mb Exp. σ_{total} = 1.18 ± 0.089 mb

Figure 51

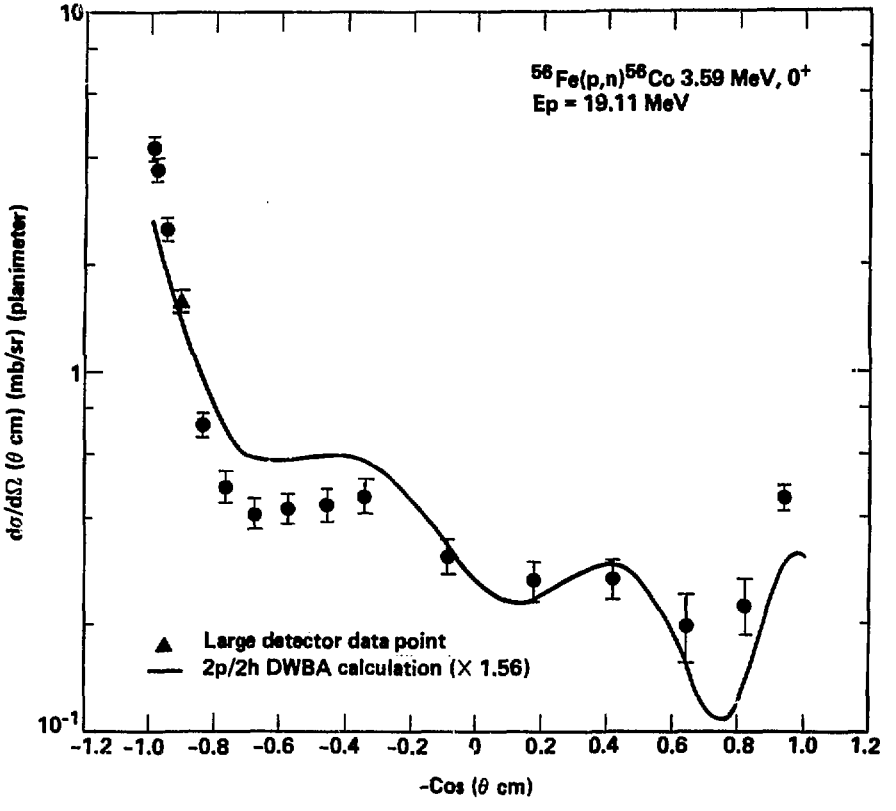

Differential Cross Sections

-Cos (θ cm)	dσ/dΩ (θ cm) (mb/sr)	Error of dσ/dΩ (θ cm) (mb/sr)
-9.98E-Ø1	4.24E+ØØ	3.2E-Ø1
-9.87E-Ø1	3.69E+ØØ	2.8E-Ø1
-9.56E-Ø1	2.51E+ØØ	1.9E-Ø1
-9.11E-Ø1	1.58E+ØØ	1.2E-Ø1
-8.38E-Ø1	7.22E-Ø1	5.4E-Ø2
-7.71E-Ø1	4.87E-Ø1	5.ØE-Ø2
-6.78E-Ø1	4.1ØE-Ø1	4.2E-Ø2
-5.76E-Ø1	4.24E-Ø1	4.1E-Ø2
-4.6ØE-Ø1	4.33E-Ø1	4.7E-Ø2
-3.42E-Ø1	4.59E-Ø1	5.1E-Ø2
-9.Ø6E-Ø2	3.12E-Ø1	3.5E-Ø2
1.75E-Ø1	2.66E-Ø1	3.5E-Ø2
4.15E-Ø1	2.71E-Ø1	3.5E-Ø2
6.4ØE-Ø1	1.99E-Ø1	4.2E-Ø2
8.17E-Ø1	2.27E-Ø1	4.ØE-Ø2
9.37E-Ø1	4.53E-Ø1	3.6E-Ø2

DWBA σ_{total} = 3.79 mb Exp. σ_{total} = 5.89 ± 0.44 mb

Figure 52

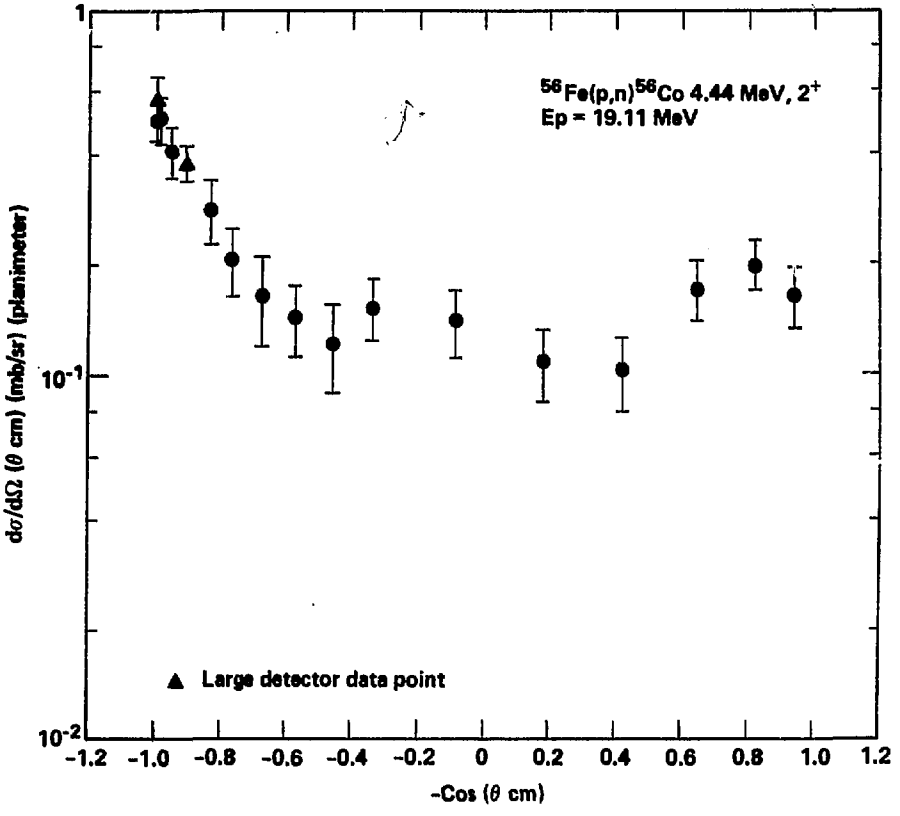

Differential Cross Sections

-Cos (θ cm)	dσ/dΩ (θ cm) (mb/sr)	Error of dσ/dΩ (θ cm) (mb/sr)
-1.00E+00	5.72E-01	8.7E-02
-9.98E-01	4.96E-01	5.9E-02
-9.87E-01	5.01E-01	7.2E-02
-9.56E-01	4.10E-01	6.5E-02
-9.11E-01	3.01E-01	4.3E-02
-8.38E-01	2.83E-01	5.7E-02
-7.70E-01	2.07E-01	4.2E-02
-6.77E-01	1.65E-01	4.5E-02
-5.75E-01	1.44E-01	3.1E-02
-4.69E-01	1.23E-01	3.3E-02
-3.41E-01	1.53E-01	2.8E-02
-8.94E-02	1.41E-01	2.9E-02
1.76E-01	1.09E-01	2.4E-02
4.16E-01	1.03E-01	2.3E-02
6.41E-01	1 72E-01	3.2E-02
8.17E-01	2.01E-01	3.1E-02
9.37E-01	1.6[illegible]01	3.1E-02

Exp. σ_{total} = 2.10 ± 0.16 mb

Figure 53

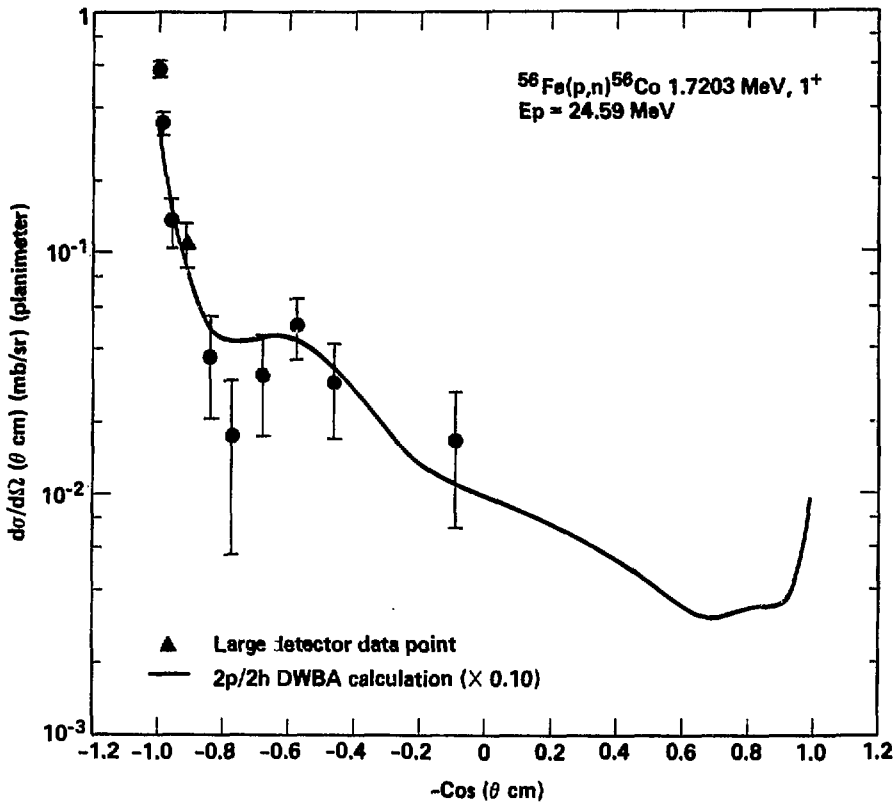

Differential Cross Sections

-Cos (θ cm)	dσ/dΩ (θ cm) (mb/sr)	Error of dσ/dΩ (θ cm) (mb/sr)
-9.98E-01	5.80E-01	4.5E-02
-9.87E-01	3.45E-01	3.7E-02
-9.56E-01	1.35E-01	3.0E-02
-9.12E-01	1.09E-01	2.3E-02
-8.39E-01	3.77E-02	1.7E-02
-7.72E-01	1.78E-02	1.2E-02
-6.80E-01	3.14E-02	1.4E-02
-5.78E-01	5.03E-02	1.4E-02
-4.62E-01	2.94E-02	1.2E-02
-9.40E-02	1.68E-02	9.6E-03

DWBA σ_{total} = 3.08 mb Exp. σ_{total} is not available

Figure 54

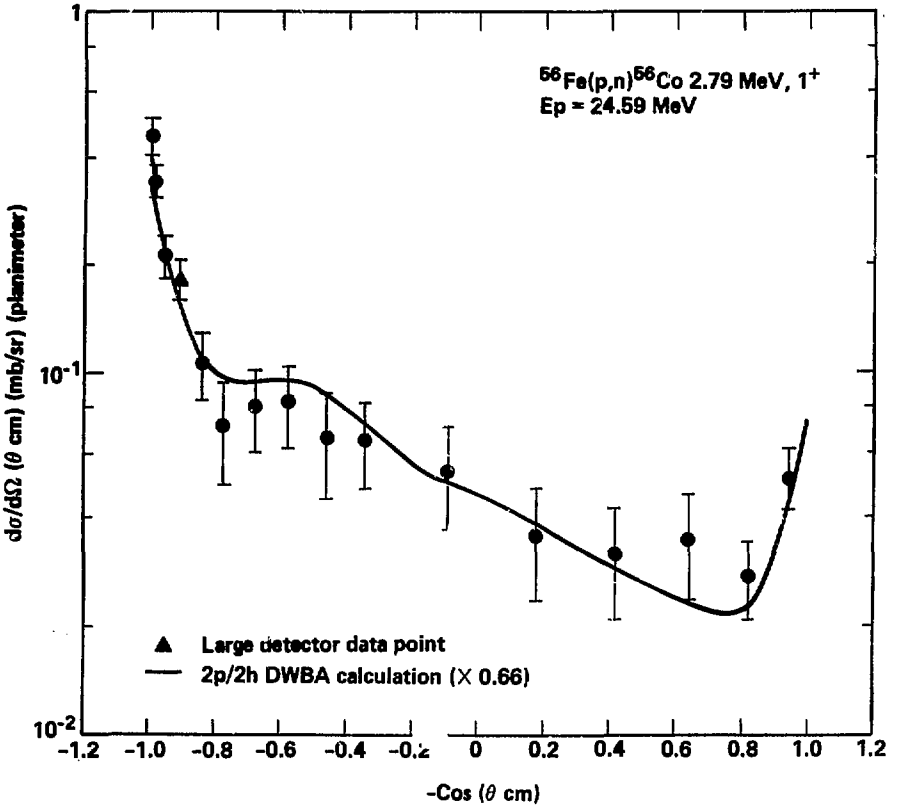

Differential Cross Sections

-Cos (θ cm)	dσ/dΩ (θ cm) (mb/sr)	Error of dσ/dΩ (θ cm) (mb/sr)
-9.98E-01	4.57E-01	5.0E-02
-9.87E-01	3.43E-01	3.7E-02
-9.56E-01	2.11E-01	2.9E-02
-9.11E-01	1.82E-01	2.4E-02
-8.39E-01	1.06E-01	2.2E-02
-7.72E-01	7.13E-02	2.2E-02
-6.79E-01	8.07E-02	2.1E-02
-5.78E-01	8.28E-02	2.1E-02
-4.62E-01	6.60E-02	2.1E-02
-3.44E-01	6.50E-02	1.7E-02
-9.33E-02	5.35E-02	1.7E-02
1.73E-01	3.56E-02	1.2E-02
4.12E-01	3.14E-02	1.1E-02
6.39E-01	3.46E-02	1.1E-02
8.16E-01	2.73E-02	6.5E-03
9.36E-01	5.14E-02	9.9E-03

DWBA σ_{total} = 1.19 mb Exp. σ_{total} = 0.78 ± 0.059 mb

Figure 55

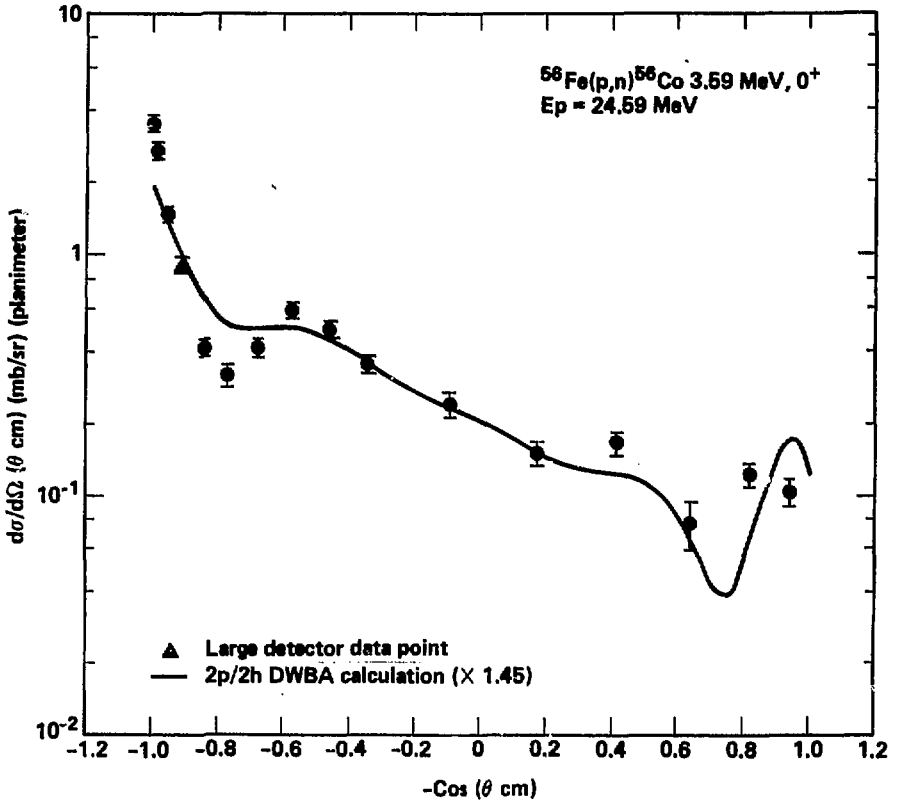

Differential Cross Sections

-Cos (θ cm)	dσ/dΩ (θ cm) (mb/sr)	Error of dσ/dΩ (θ cm) (mb/sr)
-9.98E-01	3.49E+00	2.6E-01
-9.87E-01	2.69E+00	2.0E-01
-9.56E-01	1.49E+00	1.1E-01
-9.11E-01	9.12E-01	6.8E-02
-8.39E-01	4.14E-01	3.4E-02
-7.72E-01	3.19E-01	3.3E-02
-6.79E-01	4.13E-01	3.7E-02
-5.77E-01	5.92E-01	4.4E-02
-4.61E-01	4.93E-01	3.7E-02
-3.44E-01	3.54E-01	2.7E-02
-9.27E-02	2.42E-01	2.9E-02
1.73E-01	1.51E-01	1.7E-02
4.13E-01	1.66E-01	1.9E-02
6.39E-01	7.78E-02	1.7E-02
8.16E-01	1.23E-01	1.4E-02
9.36E-01	1.84E-01	1.4E-02

DWBA σ_{total} = 2.75 mb Exp. σ_{total} = 4.00 ± 0.30 mb

Figure 56

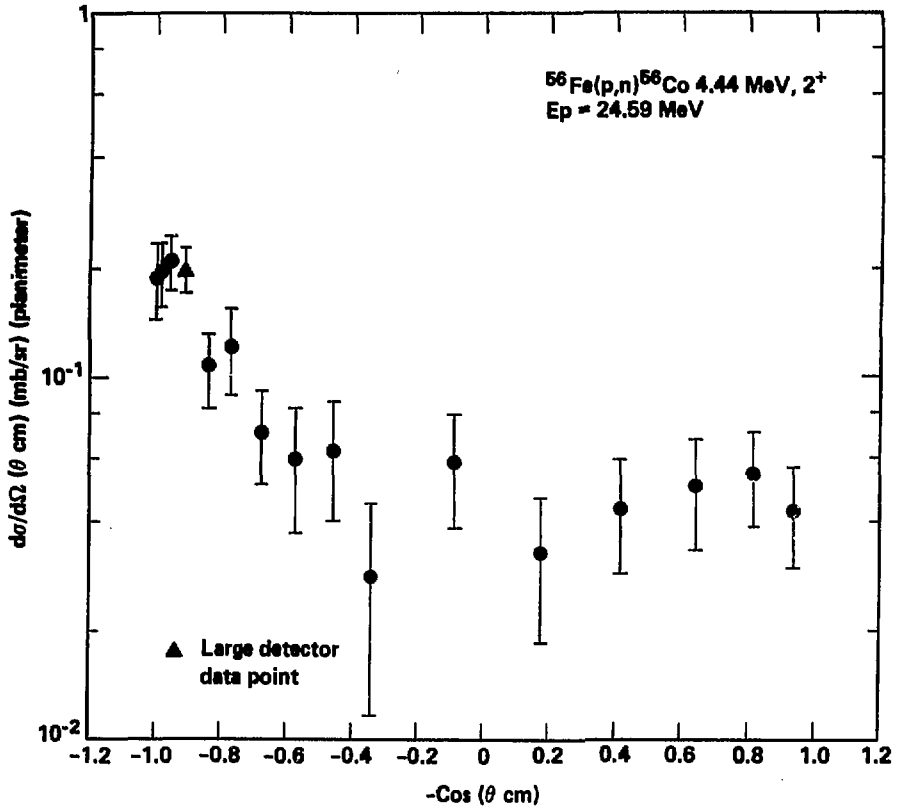

Differential Cross Sections

-Cos (θ cm)	dσ/dΩ (θ cm) (mb/sr)	Error of dσ/dΩ (θ cm) (mb/sr)
-9.98E-01	1.09E-01	4.4E-02
-9.87E-01	1.95E-01	4.0E-02
-9.56E-01	2.09E-01	3.6E-02
-9.11E-01	1.99E-01	2.8E-02
-8.39E-01	1.07E-01	2.5E-02
-7.71E-01	1.22E-01	3.3E-02
-6.79E-01	7.13E-02	2.0E-02
-5.77E-01	5.97E-02	2.3E-02
-4.61E-01	6.29E-02	2.3E-02
-3.43E-01	2.83E-02	1.7E-02
-9.21E-02	5.87E-02	2.1E-02
1.74E-01	3.25E-02	1.4E-02
4.13E-01	4.40E-02	1.5E-02
6.39E-01	5.03E-02	1.7E-02
8.16E-01	5.45E-02	1.6E-02
9.37E-01	4.30E-02	1.3E-02

Exp. σ_{total} = 0.75 ± 0.057 mb

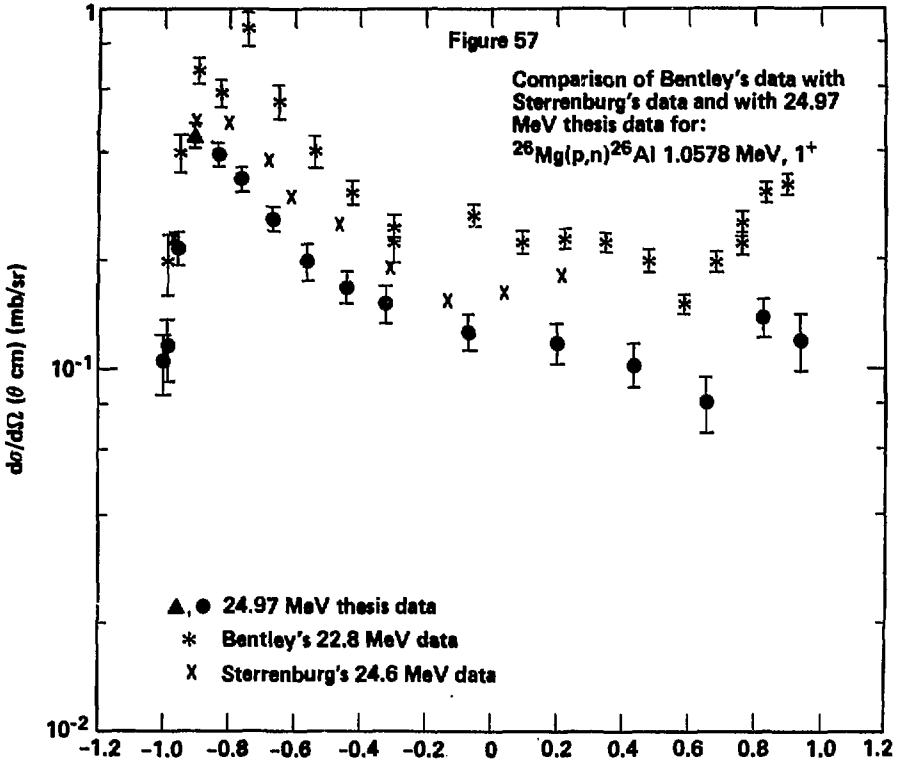

Differential Cross Sections

Bentley			Sterrenburg		Thesis		
-Cos (θ cm)	dσ/dΩ (θ cm) (mb/sr)	Error of dσ/dΩ (θ cm) (mb/sr)	-Cos (θ cm)	dσ/dΩ (θ cm) (mb/sr)	-Cos (θ cm)	dσ/dΩ (θ cm) (mb/sr)	Error of dσ/dΩ (θ cm) (mb/sr)
-9.834E-01	1.978E-01	3.868E-02	-9.6E-01	2.3E-01	-9.98E-01	1.85E-01	1.9E-02
-9.494E-01	3.971E-01	4.788E-02	-9.8E-01	4.9E-01	-9.86E-01	1.15E-01	2.2E-02
-8.979E-01	6.744E-01	5.638E-02	-8.8E-01	4.8E-01	-9.54E-01	2.16E-01	2.3E-02
-8.297E-01	5.823E-01	4.898E-02	-6.9E-01	3.8E-01	-9.08E-01	4.45E-01	3.3E-02
-7.465E-01	8.738E-01	9.858E-02	-6.2E-01	3.8E-01	-8.32E-01	3.94E-01	3.8E-02
-6.588E-01	5.586E-01	6.828E-02	-4.7E-01	2.5E-01	-7.63E-01	3.36E-01	2.5E-02
-5.428E-01	3.996E-01	4.878E-02	-3.1E-01	1.9E-01	-6.67E-01	2.68E-01	1.9E-02
-4.248E-01	3.879E-01	2.498E-02	-1.4E-01	1.5E-01	-5.63E-01	1.98E-01	2.3E-02
-3.887E-01	2.238E-01	2.688E-02	3.5E-02	1.6E-01	-4.44E-01	1.68E-01	1.7E-02
-3.887E-01	2.476E-01	1.748E-02	2.1E-01	1.8E-01	-3.25E-01	1.51E-01	1.7E-02
-5.861E-02	2.668E-01	1.858E-02			-7.12E-02	1.27E-01	1.4E-02
8.994E-02	2.231E-01	1.618E-02			1.94E-01	1.18E-01	1.5E-02
2.185E-01	2.281E-01	1.368E-02			4.31E-01	1.83E-01	1.4E-02
3.427E-01	2.233E-01	1.368E-02			6.52E-01	8.89E-02	1.4E-02
4.755E-01	1.989E-01	1.528E-02			8.23E-01	1.38E-01	1.6E-02
5.838E-01	1.584E-01	9.888E-03			9.39E-01	1.19E-01	2.1E-02
6.821E-01	1.968E-01	1.348E-02					
7.581E-01	2.211E-01	1.588E-02					
7.581E-01	2.583E-01	1.908E-02					
8.341E-01	3.869E-01	2.878E-02					
8.967E-01	3.226E-01	2.888E-02					

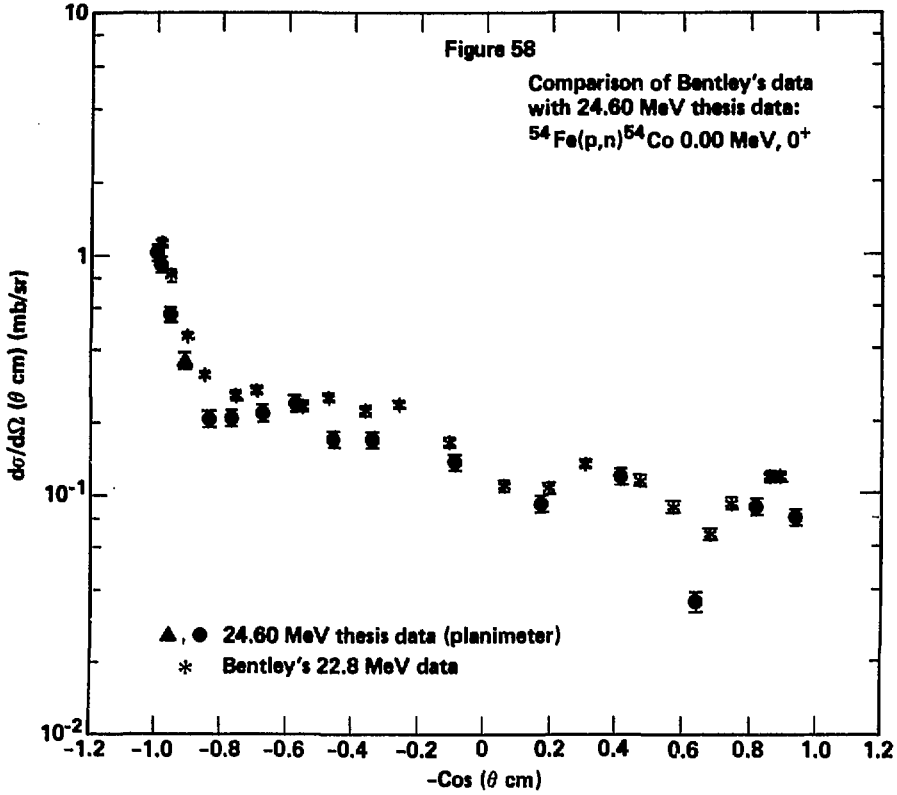

Differential Cross Sections

Bentley			Thesis		
-Cos (θ cm)	dσ/dΩ (θ cm) (mb/sr)	Error of dσ/dΩ (θ cm) (mb/sr)	-Cos (θ cm)	dσ/dΩ (θ cm) (mb/sr)	Error of dσ/dΩ (θ cm) (mb/sr)
-9.841E-01	1.142E+00	3.400E-02	-9.98E-01	1.03E+00	7.7E-02
-9.841E-01	1.121E+00	3.300E-02	-9.87E-01	9.18E-01	6.9E-02
-9.552E-01	8.441E-01	2.710E-02	-9.56E-01	5.59E-01	4.2E-02
-9.552E-01	7.909E-01	2.250E-02	-9.11E-01	3.63E-01	2.7E-02
-9.019E-01	4.589E-01	1.350E-02	-8.39E-01	2.05E-01	1.5E-02
-8.496E-01	3.151E-01	9.800E-03	-7.71E-01	2.07E-01	1.6E-02
-7.559E-01	2.578E-01	1.200E-02	-6.79E-01	2.18E-01	1.7E-02
-6.909E-01	2.707E-01	1.010E-02	-5.77E-01	2.38E-01	1.8E-02
-5.570E-01	2.321E-01	9.200E-03	-4.61E-01	1.69E-01	1.3E-02
-4.815E-01	2.523E-01	9.700E-03	-3.43E-01	1.68E-01	1.3E-02
-3.649E-01	2.222E-01	8.900E-03	-9.18E-02	1.36E-01	1.0E-02
-2.647E-01	2.363E-01	8.600E-03	1.74E-01	9.17E-02	6.9E-03
-1.097E-01	1.644E-01	7.800E-03	4.14E-01	1.18E-01	8.9E-03
5.948E-02	1.085E-01	5.100E-03	6.39E-01	3.57E-02	3.3E-03
1.975E-01	1.057E-01	5.500E-03	8.16E-01	8.90E-02	6.7E-03
3.065E-01	1.331E-01	5.500E-03	9.37E-01	8.02E-02	6.0E-03
4.689E-01	1.137E-01	5.800E-03			
5.783E-01	8.934E-02	4.670E-03			
6.788E-01	6.822E-02	3.980E-03			
7.427E-01	9.217E-02	4.950E-03			
8.575E-01	1.177E-01	5.800E-03			
8.906E-01	1.176E-01	5.500E-03			

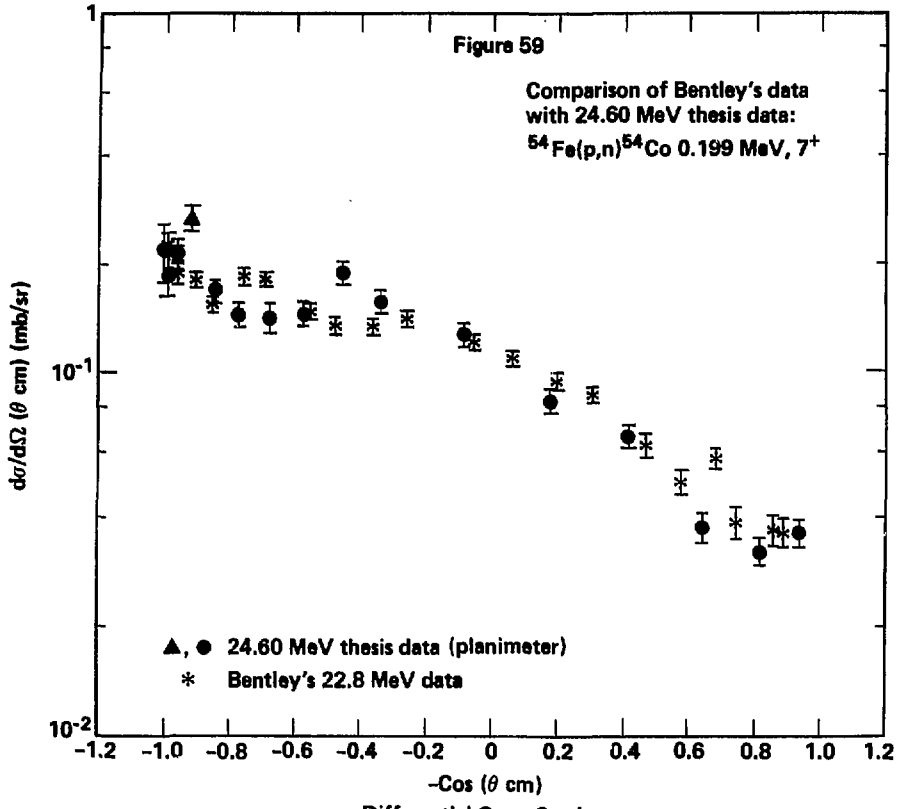

Differential Cross Sections

Bentley			Thesis		
-Cos (θ cm)	dσ/dΩ (θ cm) (mb/sr)	Error of dσ/dΩ (θ cm) (mb/sr)	-Cos (θ cm)	dσ/dΩ (θ cm) (mb/sr)	Error of dσ/dΩ (θ cm) (mb/sr)
-9.84ØE-Ø1	2.127E-Ø1	1.68ØE-Ø2	-9.98E-Ø1	2.2ØE-Ø1	4.1E-Ø2
-9.84ØE-Ø1	2.296E-Ø1	1.74ØE-Ø2	-9.87E-Ø1	1.9ØE-Ø1	2.6E-Ø2
-9.552E-Ø1	2.Ø99E-Ø1	1.58ØE-Ø2	-9.56E-Ø1	2.2ØE-Ø1	1.7E-Ø2
-9.552E-Ø1	1.888E-Ø1	1.25ØE-Ø2	-9.11E-Ø1	2.7ØE-Ø1	2.ØE-Ø2
-9.Ø18E-Ø1	1.812E-Ø1	8.8ØØE-Ø3	-8.38E-Ø1	1.68E-Ø1	1.3E-Ø2
-8.496E-Ø1	1.546E-Ø1	7.1ØØE-Ø3	-7.71E-Ø1	1.45E-Ø1	1.1E-Ø2
-7.557E-Ø1	1.85ØE-Ø1	1.Ø2ØE-Ø2	-6.78E-Ø1	1.42E-Ø1	1.4E-Ø2
-6.9ØØE-Ø1	1.818E-Ø1	8.4ØØE-Ø3	-5.77E-Ø1	1.46E-Ø1	1.1E-Ø2
-5.569E-Ø1	1.481E-Ø1	7.4ØØE-Ø3	-4.6ØE-Ø1	1.89E-Ø1	1.4E-Ø2
-4.813E-Ø1	1.349E-Ø1	7.4ØØE-Ø3	-3.43E-Ø1	1.57E-Ø1	1.2E-Ø2
-3.647E-Ø1	1.336E-Ø1	7.2ØØE-Ø3	-9.17E-Ø2	1.27E-Ø1	9.5E-Ø3
-2.646E-Ø1	1.4Ø4E-Ø1	6.8ØØE-Ø3	1.74E-Ø1	8.3ØE-Ø2	6.2E-Ø3
-5.739E-Ø2	1.21ØE-Ø1	6.2ØØE-Ø3	4.14E-Ø1	6.59E-Ø2	4.9E-Ø3
5.965E-Ø2	1.Ø87E-Ø1	5.1ØØE-Ø3	6.39E-Ø1	3.72E-Ø2	3.4E-Ø3
1.977E-Ø1	9.381E-Ø2	5.26ØE-Ø3	8.16E-Ø1	3.2ØE-Ø2	2.9E-Ø3
3.Ø67E-Ø1	8.594E-Ø2	4.52ØE-Ø3	9.37E-Ø1	3.6ØE-Ø2	3.ØE-Ø3
4.69ØE-Ø1	6.233E-Ø2	4.61ØE-Ø3			
5.7Ø4E-Ø1	4.937E-Ø2	3.76ØE-Ø3			
6.789E-Ø1	5.719E-Ø2	3.7ØØE-Ø3			
7.428E-Ø1	3.856E-Ø2	3.79ØE-Ø3			
8.575E-Ø1	3.671E-Ø2	3.41ØE-Ø3			
8.9Ø7E-Ø1	3.618E-Ø2	3.13ØE-Ø3			

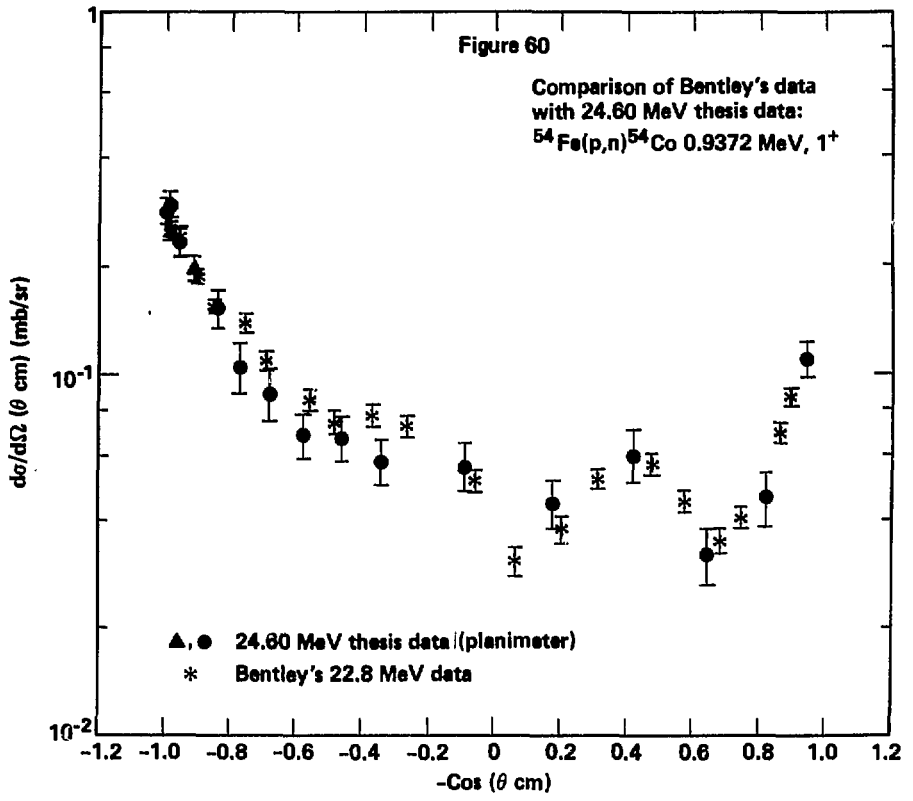

Differential Cross Sections

-Cos (θ cm)	Bentley $d\sigma/d\Omega$ (θ cm) (mb/sr)	Error of $d\sigma/d\Omega$ (θ cm) (mb/sr)	-Cos (θ cm)	Thesis $d\sigma/d\Omega$ (θ cm) (mb/sr)	Error of $d\sigma/d\Omega$ (θ cm) (mb/sr)
-9.84ØE-Ø1	2.577E-Ø1	1.5ØØE-Ø2	-9.98E-Ø1	2.85E-Ø1	2.3E-Ø2
-9.84ØE-Ø1	2.515E-Ø1	1.48ØE-Ø2	-9.87E-Ø1	2.96E-Ø1	2.5E-Ø2
-9.552E-Ø1	2.443E-Ø1	1.32ØE-Ø2	-9.56E-Ø1	2.33E-Ø1	2.1E-Ø2
-9.552E-Ø1	2.25ØE-Ø1	1.12ØE-Ø2	-9.11E-Ø1	1.98E-Ø1	1.5E-Ø2
-9.Ø17E-Ø1	1.888E-Ø1	8.3ØØE-Ø3	-8.38E-Ø1	1.54E-Ø1	1.8E-Ø2
-8.494E-Ø1	1.56ØE-Ø1	6.6ØØE-Ø3	-7.71E-Ø1	1.Ø6E-Ø1	1.7E-Ø2
-7.554E-Ø1	1.4ØØE-Ø1	8.8ØØE-Ø3	-6.78E-Ø1	8.93E-Ø2	1.6E-Ø2
-6.9Ø4E-Ø1	1.1ØØE-Ø1	6.7ØØE-Ø3	-5.76E-Ø1	6.86E-Ø2	9.6E-Ø3
-5.564E-Ø1	8.538E-Ø2	5.68ØE-Ø3	-4.6ØE-Ø1	6.72E-Ø2	9.3E-Ø3
-4.8Ø8E-Ø1	7.414E-Ø2	5.45ØE-Ø3	-3.42E-Ø1	5.8ØE-Ø2	8.2E-Ø3
-3.641E-Ø1	7.756E-Ø2	5.51ØE-Ø3	-9.11E-Ø2	5.62E-Ø2	8.5E-Ø3
-2.639E-Ø1	7.18ØE-Ø2	4.72ØE-Ø3	1.76E-Ø1	4.42E-Ø2	6.7E-Ø3
-5.669E-Ø2	5.1Ø6E-Ø2	3.61ØE-Ø3	4.14E-Ø1	6.Ø3E-Ø2	9.9E-Ø3
6.Ø35E-Ø2	3.Ø76E-Ø2	2.73ØE-Ø3	6.4ØE-Ø1	3.18E-Ø2	5.5E-Ø3
1.983E-Ø1	3.739E-Ø2	3.14ØE-Ø3	8.16E-Ø1	4.56E-Ø2	7.7E-Ø3
3.Ø74E-Ø1	5.163E-Ø2	3.25ØE-Ø3	9.37E-Ø1	1.1ØE-Ø1	1.2E-Ø2
4.695E-Ø1	5.646E-Ø2	3.95ØE-Ø3			
5.7Ø9E-Ø1	4.483E-Ø2	3.Ø7ØE-Ø3			
6.793E-Ø1	3.474E-Ø2	2.57ØE-Ø3			
7.43ØE-Ø1	4.Ø24E-Ø2	2.82ØE-Ø3			
8.578E-Ø1	6.858E-Ø2	4.39ØE-Ø3			
8.9Ø9E-Ø1	8.583E-Ø2	4.57ØE-Ø3			

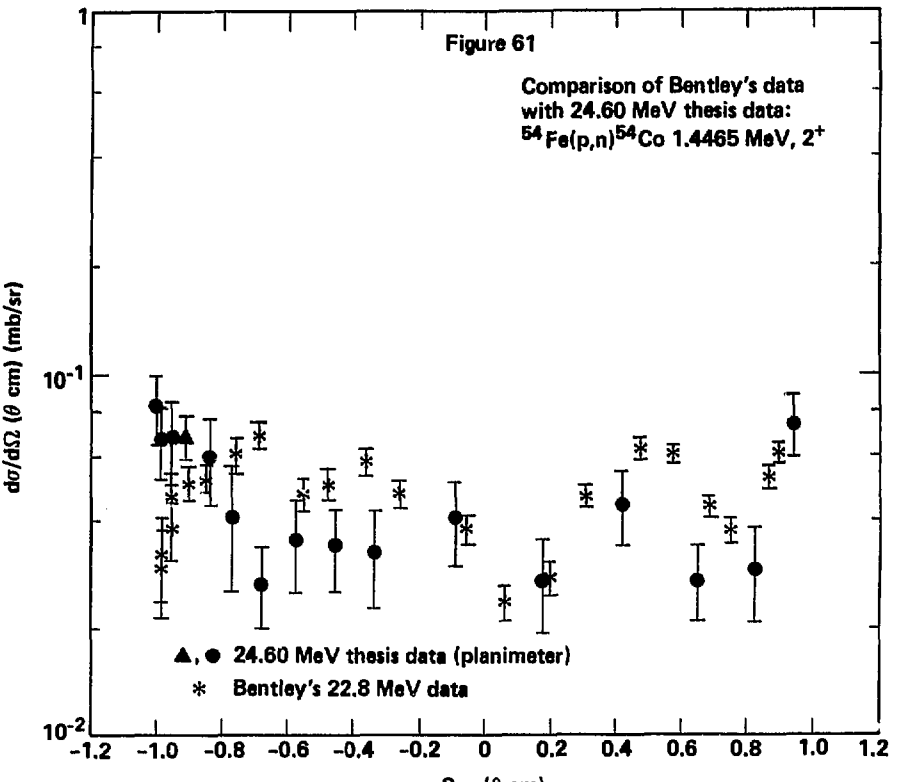

Differential Cross Sections

-Cos (θ cm)	Bentley dσ/dΩ (θ cm) (mb/sr)	Error of dσ/dΩ (θ cm) (mb/sr)	-Cos (θ cm)	Thesis dσ/dΩ (θ cm) (mb/sr)	Error of dσ/dΩ (θ cm) (mb/sr)
-9.84ØE-Ø1	2.926E-Ø2	7.91ØE-Ø3	-9.98E-Ø1	8.13E-Ø2	1.7E-Ø2
-9.84ØE-Ø1	3.191E-Ø2	8.34ØE-Ø3	-9.87E-Ø1	6.6ØE-Ø2	1.5E-Ø2
-9.651E-Ø1	4.536E-Ø2	7.71ØE-Ø3	-9.56E-Ø1	6.67E-Ø2	1.7E-Ø2
-9.551E-Ø1	3.745E-Ø2	6.64ØE-Ø3	-9.11E-Ø1	6.72E-Ø2	9.1E-Ø3
-9.Ø16E-Ø1	5.Ø26E-Ø2	5.32ØE-Ø3	-8.38E-Ø1	5.94E-Ø2	1.6E-Ø2
-8.493E-Ø1	5.156E-Ø2	4.56ØE-Ø3	-7.71E-Ø1	4.Ø5E-Ø2	1.5E-Ø2
-7.552E-Ø1	5.98ØE-Ø2	6.75ØE-Ø3	-6.78E-Ø1	2.67E-Ø2	6.8E-Ø3
-6.9Ø1E-Ø1	6.799E-Ø2	5.86ØE-Ø3	-5.76E-Ø1	3.5ØE-Ø2	1.ØE-Ø2
-5.56ØE-Ø1	4.668E-Ø2	4.75ØE-Ø3	-4.6ØE-Ø1	3.36E-Ø2	8.6E-Ø3
-4.8Ø4E-Ø1	4.993E-Ø2	4.86ØE-Ø3	-3.42E-Ø1	3.22E-Ø2	9.7E-Ø3
-3.637E-Ø1	5.724E-Ø2	4.94ØE-Ø3	-9.Ø6E-Ø2	4.ØØE-Ø2	1.ØE-Ø2
-2.634E-Ø1	4.669E-Ø2	4.16ØE-Ø3	1.75E-Ø1	2.72E-Ø2	7.8E-Ø3
-5.617E-Ø2	3.748E-Ø2	3.35ØE-Ø3	4.15E-Ø1	4.37E-Ø2	1.ØE-Ø2
6.Ø87E-Ø2	2.36ØE-Ø2	2.58ØE-Ø3	6.4ØE-Ø1	2.72E-Ø2	6.4E-Ø3
1.989E-Ø1	2.756E-Ø2	2.95ØE-Ø3	8.16E-Ø1	2.9ØE-Ø2	8.4E-Ø3
3.879E-Ø1	4.598E-Ø2	3.13ØE-Ø3	9.37E-Ø1	7.27E-Ø2	1.4E-Ø2
4.699E-Ø1	6.221E-Ø2	4.16ØE-Ø3			
5.713E-Ø1	5.98ØE-Ø2	3.46ØE-Ø3			
6.796E-Ø1	4.275E-Ø2	2.82ØE-Ø3			
7.433E-Ø1	3.676E-Ø2	2.76ØE-Ø3			
8.579E-Ø1	5.162E-Ø2	3.88ØE-Ø3			
8.9Ø9E-Ø1	6.Ø29E-Ø2	3.85ØE-Ø3			

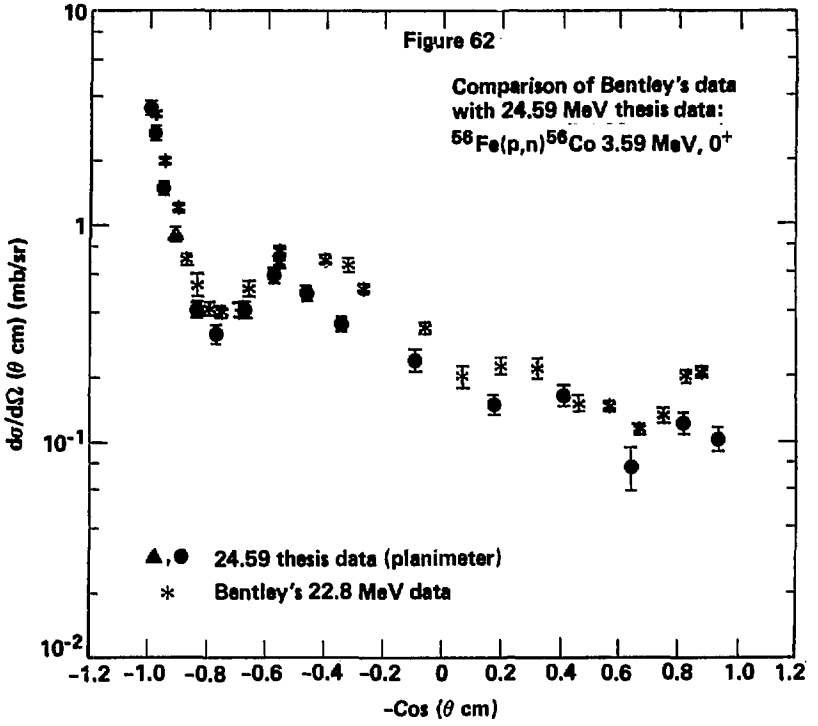

Differential Cross Sections

Bentley			Thesis		
-Cos (θ cm)	dσ/dΩ (θ cm) (mb/sr)	Error of dσ/dΩ (θ cm) (mb/sr)	-Cos (θ cm)	dσ/dΩ (θ cm) (mb/sr)	Error of dσ/dΩ (θ cm) (mb/sr)
-9.841E-01	3.262E+00	8.400E-02	-9.98E-01	3.49E+00	2.6E-01
-9.515E-01	1.993E+00	7.800E-02	-9.87E-01	2.69E+00	2.0E-01
-9.021E-01	1.210E+00	5.700E-02	-9.56E-01	1.49E+00	1.1E-01
-8.716E-01	6.984E-01	3.970E-02	-9.11E-01	9.12E-01	6.8E-02
-8.365E-01	5.357E-01	6.380E-02	-8.39E-01	4.14E-01	3.4E-02
-8.365E-01	4.194E-01	3.430E-02	-7.72E-01	3.19E-01	3.3E-02
-7.965E-01	4.209E-01	3.040E-02	-6.79E-01	4.13E-01	3.7E-02
-7.562E-01	4.063E-01	2.450E-02	-5.77E-01	5.92E-01	4.4E-02
-6.952E-01	4.142E-01	3.180E-02	-4.61E-01	4.93E-01	3.7E-02
-6.626E-01	5.181E-01	4.090E-02	-3.44E-01	3.54E-01	2.7E-02
-5.576E-01	7.503E-01	5.320E-02	-9.27E-02	2.42E-01	2.9E-02
-5.576E-01	6.703E-01	3.480E-02	1.73E-01	1.51E-01	1.7E-02
-4.015E-01	6.952E-01	3.290E-02	4.13E-01	1.66E-01	1.9E-02
-3.211E-01	6.581E-01	4.810E-02	6.39E-01	7.70E-02	1.7E-02
-2.656E-01	5.133E-01	2.330E-02	8.16E-01	1.23E-01	1.4E-02
-6.366E-02	3.387E-01	2.000E-02	9.36E-01	1.04E-01	1.4E-02
6.714E-02	2.025E-01	2.320E-02			
1.965E-01	2.257E-01	1.990E-02			
3.221E-01	2.202E-01	2.540E-02			
4.650E-01	1.526E-01	1.360E-02			
5.654E-01	1.468E-01	8.300E-03			
6.668E-01	1.155E-01	6.000E-03			
7.479E-01	1.329E-01	9.700E-03			
8.269E-01	2.011E-01	1.300E-02			
8.802E-01	2.100E-01	1.210E-02			

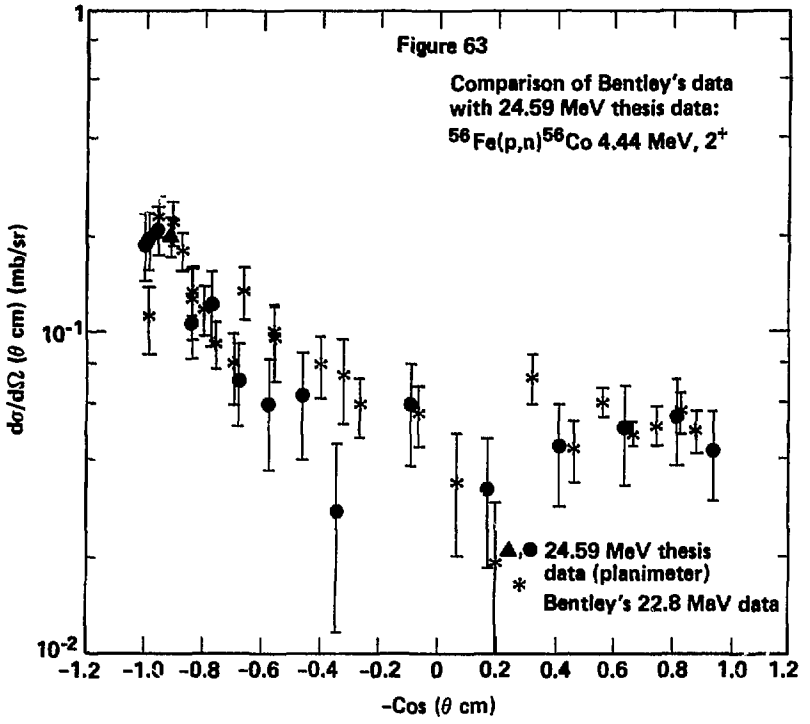

Differential Cross Sections

Bentley			Thesis		
-Cos (θ cm)	dσ/dΩ (θ cm) (mb/sr)	Error of dσ/dΩ (θ cm) (mb/sr)	-Cos (θ cm)	dσ/dΩ (θ cm) (mb/sr)	Error of dσ/dΩ (θ cm) (mb/sr)
-9.841E-01	1.114E-01	2.63ØE-02	-9.98E-01	1.89E-01	4.4E-02
-9.515E-01	2.3Ø5E-01	3.31ØE-02	-9.87E-01	1.95E-01	4.ØE-02
-9.Ø19E-01	2.2Ø1E-01	3.4ØØE-02	-9.56E-01	2.Ø9E-01	3.6E-02
-8.715E-01	1.792E-01	2.41ØE-02	-9.11E-01	1.99E-01	2.8E-02
-8.363E-01	1.268E-01	3.24ØE-02	-8.39E-01	1.Ø7E-01	2.5E-02
-8.363E-01	1.344E-01	2.29ØE-02	-7.71E-01	1.22E-01	3.3E-02
-7.962E-01	1.179E-01	2.Ø9ØE-02	-6.79E-01	7.13E-02	2.ØE-02
-7.559E-01	9.153E-02	1.523E-02	-5.77E-01	5.97E-02	2.3E-02
-6.948E-01	7.885E-02	1.974E-02	-4.61E-01	6.29E-02	2.3E-02
-6.622E-01	1.336E-01	2.48ØE-02	-3.43E-01	2.83E-02	1.7E-02
-5.572E-01	9.442E-02	2.5Ø3E-02	-9.21E-02	5.87E-02	2.1E-02
-5.572E-01	1.Ø15E-01	1.97ØE-02	1.74E-01	3.25E-02	1.4E-02
-4.ØØ8E-01	7.897E-02	1.7Ø9E-02	4.13E-01	4.4ØE-02	1.5E-02
-3.285E-01	7.318E-02	2.141E-02	6.39E-01	5.Ø3E-02	1.7E-02
-2.649E-01	5.914E-02	1.234E-02	8.16E-01	5.45E-02	1.6E-02
-6.296E-02	5.559E-02	1.173E-02	9.37E-01	4.3ØE-02	1.3E-02
6.8Ø2E-02	3.488E-02	1.389E-02			
1.973E-01	1.896E-02	1.Ø68E-02			
3.228E-01	7.173E-02	1.272E-02			
4.656E-01	4.321E-02	9.34ØE-03			
5.66ØE-01	6.Ø29E-02	6.1ØØE-03			
6.673E-01	4.817E-02	4.2ØØE-03			
7.483E-01	5.113E-02	6.96ØE-03			
8.271E-01	5.611E-02	8.Ø6ØE-03			
8.8Ø3E-01	4.9Ø3E-02	7.38ØE-03			

APPENDIX: COMPUTER CODES

This appendix presents a brief description of the computer programs named in this thesis.

DWBA79 is essentially the distorted-wave Born approximation code DWBA70, with a few minor modifications. DWBA70 was written by R. Schaeffer and J. Raynal of the Centre d'Etudes Nucléaires de Saclay, B.P. No. 2, 91-Gif-sur-Yvette, France. DWBA79 was used to calculate (p,n) differential cross sections and angle-integrated cross sections for transitions to 0^+ and 1^+ states.

EFFIC calculates the efficiency of a neutron detector using only (n,p) cross sections. The code was produced by E-division at Livermore. EFFIC was used to help determine the efficiency of the 11.4 cm dia. x 5.1 cm long NE213 small detectors.

GRIND calculates differential cross sections from the integrated counts under peaks in time-of-flight (TOF) spectra. GRIND produces a set of differential cross sections for the 16 angles at which detectors are positioned in the neutron TOF pit. The code also generates the neutron energy at each angle, and the center of mass angle corresponding to the detector angle in the laboratory system of reference. GRIND was produced by E-division at Livermore. The code was used to generate ^{54}Fe(p,n)^{54}Co cross sections at two proton bombarding energies. The code was also used to generate D(d,n)^{3}He and T(d,n)^{4}He cross sections for detector efficiency measurements.

KANISH uses Monte Carlo methods to calculate the neutron detection efficiency of hydrocarbon scintillators. It considers both n-p scattering, and n-C interactions. The code was developed by Günter Kanisch of the University of Hamburg, Germany. KANISH is documented in: Günter Kanisch, "Ein Programm zur Berechnung des Neutronen-Ansprechvermögens von organischen Szintillatoren

und dessen Anwendung bei der Spektrometrie von Neutronen aus der Reaktion $^{197}Au(p,n)^{197}Hg$" (Hamburg, Germany: University of Hamburg, 1976). The KANISH calculated Area x Efficiency (AE) of our NE213 detectors were compared with the measured AE.

KEFF also uses Monte Carlo methods to calculate the efficiency of hydrocarbon scintillators in detecting neutrons. The code considers the interaction of neutrons with carbon nuclei, as well as n-p scattering. The code is described in: R.A. Cecil, B.D. Anderson, and R. Madey, "Improved Predictions of Neutron Detection Efficiency for Hydrocarbon Scintillators from 1 MeV to about 300 MeV," *Nucl. Instr. and Meth.* 161, 439 (1979). KEFF was used to calculate the Area x Efficiency (AE) of the our NE213 detectors for comparison with the measured AE.

LEGENDRE fits a sum of Legendre polynomials to a set of differential cross sections and calculates the angle-integrated cross section. Three or more Legendre polynomials can be used in the sum; we use the angle-integrated cross section of the set giving the best fit to the data. The code was produced by E-division at Livermore. The code was used to determine values of the angle-integrated cross section exp. σ_{total}.

NDFOXE fits Gaussian curves, Gaussian curves with tails, or Lorentzian curves, to peaks in TOF spectra. NDFOXE integrates the area under the curves and provides an error for the integrated area. The code was produced by E-division at Livermore. NDFOXE areas were used by GRIND to compute differential cross sections.

NPCS uses a Legendre polynomial expansion with Drosg's Legendre coefficients (these coefficients are tabulated in No. 38 of section VI) to generate differential cross sections for $D(d,n)^3He$ and $T(d,n)^4He$ reactions. The code was

produced by E-division at Livermore. NPCS was used to calculate differential cross sections used in determining large and small detector AE's.

TOFFEE converts raw TOF spectra into plots of $\frac{d^2\sigma}{d\Omega dU}$ $\left[\frac{mb}{sr\text{-}MeV}\right]$ vs. U [MeV], where U is the excitation energy of the residual nucleus. The code also generates error bars on each $\frac{d^2\sigma}{d\Omega dU}$ plotted. The code has the capability of averaging $\frac{d^2\sigma}{d\Omega dU}$ over two channels, and computing the appropriate error. The code was developed at Livermore by E-division. TOFFEE plots were made for all the spectra. Peaks in the TOFFEE plots corresponding to transitions to particular nuclear states were integrated to yield differential cross sections.

For listings of the above programs contact:

Mr. Bertram A. Pohl
University of California
Lawrence Livermore National Laboratory
P.O. Box 808
Livermore, California 94550
U.S.A.